Title

2D Films and 3D-Printed Electrodes For Supercapacitors

Author

Yao, Bin

Publication Date

2020

UNIVERSITY OF CALIFORNIA
SANTA CRUZ

2D FILMS AND 3D-PRINTED ELECTRODES FOR SUPERCAPACITORS

A dissertation submitted in partial satisfaction
of the requirements for the degree of

DOCTOR OF PHILOSOPHY

in

CHEMISTRY

by

Bin Yao

September 2020

The Dissertation of Bin Yao is approved:

Professor Yat Li, chair

Professor Jin Zhong Zhang

Professor Ilan Benjamin

Quentin Williams
Interim Vice Provost and Dean of Graduate Studies

Table of Contents

List of Figures

Chapter 1

Chapter 2

Chapter 3

Chapter 4

Chapter 5

Chapter 6

Chapter 7

Abstract

2D Films and 3D Printed Electrodes for Supercapacitors

by

Bin Yao

Sustainable energy is advocated over the past few decades when the traditional fossil fuels are running out and the environmental pollution is getting worse. In response to the call for greener energy supply, various energy conversion methods have been established, such as solar energy, wind energy, hydro energy, geothermal energy and so on. The intermittent and regional nature of these clean energy further drive the development of high-performance energy storage devices. Batteries and electrostatic capacitors are two most investigated power sources. Batteries own good energy densities while their power performance is mediocre. Electrostatic capacitors are advantageous in their high power densities, while their energy densities are much inferior. Supercapacitors represent a new and promising energy storage technique that can bridge the gap between these two power sources. They have higher power densities than batteries and higher energy densities than traditional electrostatic capacitors. The key to achieve sound electrochemical performance of supercapacitor lies in the advanced electrodes, which are required to rapidly store/deliver a good amount of charges and retain their structural integrity after long-time operation.

This dissertation covers the research of my past five years at UC Santa Cruz in design and synthesis of high-performance supercapacitor electrodes. Some

nanomaterials have been studied in this dissertation, including metal oxide, metal nitride, and carbonaceous materials. Different electrode structures have been fabricated, such as paper-based electrodes and 3D-printed electrodes. Both the intrinsic electrochemical properties of electrode materials and practical considerations of device design will be analyzed.

The contents in this dissertation are mainly composed of two parts. The first parts are the investigation on the two-dimensional (2D) film-based electrodes for supercapacitors. The second parts are the exploration of three-dimensional (3D) printed electrodes for supercapacitors. To be more specific, Chapter 1 introduces the background of the sustainable energy storage, mechanism of supercapacitors, and the recent advancement of 2D film and 3D-printed supercapacitor electrodes. Chapter 2 reports the fabrication and the electrochemical performance of a flexible and transparent MoO_3 nanopaper, a new form of freestanding electrodes for supercapacitors. Chapter 3 demonstrates a freestanding and flexible TiN nanopaper that shows ultrahigh power performance and ultralong electrochemical stability. Chapter 4 to chapter 7 are mainly focused on the development of 3D printed electrodes. Chapter 4 presents a 3D printed carbon aerogel with very high specific surface area via a thixotropic R-F based ink. Chapter 5 describes a new five-scale pore carbon network achieved via additive manufacturing. By adding a new dimension of 3D printed pores, the new carbon network displays superior charge storage capability even under ultralow temperature of -70 ^{o}C. Chapter 6 successfully addresses a long-term challenge for supercapacitors, that is the electrochemical performance significantly gets deteriorated with the increase of active loading. In this chapter, a 3D printed macroporous graphene aerogels has been fabricated to support the record-high loading of MnO_2, which is two to three orders higher than the current reports. More importantly, this 3D printed graphene/MnO_2 can simultaneously achieve excellent capacitance normalized to area, gravimetry and volume, which is the trade-off for most electrodes. This work also successfully validates the feasibility of printing practical pseudocapacitive electrodes, which might revolutionize the pseudocapacitor fabrication. Chapter 7 exhibits a new surface-functionalized 3D printed graphene aerogel electrode that achieves not only a benchmark areal capacitance at high current densities but also an ultrahigh intrinsic capacitance even at high mass loadings. This work also clearly demonstrates the role of 3D printed structure in boosting the kinetics and intrinsic capacitance of pseudocapacitive graphene aerogels. Chapter 8 is a summary of the current problems and an outlook of further directions in the supercapacitor research. Fundamental scientific questions and practical issues associated with the 2D films and 3D printed electrodes for supercapacitors will also be discussed.

Dedication

DEDICATED

TO

MY PARENTS, WEIJUN YAO & XIUQIN ZHENG

MY WIFE, JING ZHANG

MY DAUGHTER, JULIE YAO & MY SON, TYLER YAO

Acknowledgments

Time flies! I am almost finishing my Ph.D. study and research at Santa Cruz. The past five years in Prof. Yat Li's group at the Department of Chemistry and Biochemistry, University of California, Santa Cruz not only give me a Doctoral degree of Philosophy, it also leaves me numerous unforgettable moments of the study, the research, and the life at this world-famous, beautiful campus. At this particular moment, I want to thank those people who have helped me in the past few years.

I would like first to thank my research advisor, Professor Yat Li. Without his offer five years ago, I won't be able to be here. He has reshaped the way I do research. His motivation-driven style towards every research topic, time management, and priority setting in each project will benefit my whole life in academia. I also learned from him how a nice person could be. He is such a humble, respectful, thoughtful, and inspiring person. He always gave me more than I can give him back. I still remember the first day I arrived at SFO. There was a delay in my entry, and he waited a long time to pick me up. He treated me the first meal I had in the US, a Mexican-favor cafe in the Mission street. He gave me a lot of suggestions on future career plans, on how to deal with colleagues, and on how to respect each other. I was touched when I was down, and he came to back me up. I am also very fortunate to work with and learn from Yat's wife, Dr. Fang Qian. She is such a smart and diligent researcher and is well-prepared for her work every time. She could always pop out new ideas for a project. She is also a fast learner. She can quickly become an expert in a new area. Without her inspiring instruction and help, I will not be able to devote myself to the 3D printing field.

I would also like to thank my research committee members, Professor Jin Zhong Zhang, Professor Yat Li, Professor Ilan Benjamin, and Prof. Frank Bud Bridges. Their strict and high standards in evaluating my second-year seminar, oral exams, and yearly reviews always push me to polish myself and make every detail in my research better. I could never forget Jin's encouraging words when I reached him for advice on my career. His encouragement gave me the power to follow my heart and chose my career path. His optimistic personality also inspires me in both my life and work.

I would like to thank the talented peers I have worked with at the University of California, Santa Cruz. I appreciate all their help to me during the past five years. I could not have the current achievements without their input. I thank the doctors who graduated from the Li lab: Dr. Gongming Wang, Dr. Yichuan Ling, Dr. Hanyu Wang, Dr. Yi Yang, Dr. Tianyu Liu, Dr. Tianyi Kou; graduate students who are working in the Li lab: Wang Xiao, Daniel Bulmanh, Mingpeng Chen, Megan Freyman, Shanwen Wang, Dun Lin; scholars who joined or are visiting in the Li lab: Prof. Xihong Lu, Prof. Teng Zhai, Prof. Feng Zhang, Prof. Yang Yang, Dr. Mingyang Li, Prof. Yu Song, Dr. Huarong Peng, Prof. Zihang Huang, Prof. Changjin Tang, Dr. Xiaoli Fan, Prof. Wei Xu, Dr. Cheng Cheng, Dr. Lei Zhang, Junzhe Kang and André Luiz Martins de Freitas; Undergraduates who worked with me: Andrea Cruz, Germain Madina Jr., Martina Morelli, Azebe Ayalew, Gerardo Delgado, Thanh Huynh, Brianna Aguilar-Solis, Dana Byrne, and Soren Faulkner; Summer intern high school students who worked with me: Jennifer John, Daisy Kamp, Samira Sriram, Shangfeihong Cao, Dean Tran, Annie Ma, Natali Solis Gomez, Meera Suresh, and Eileen Ho; Peers from Prof. Jin Zhong Zhang's lab: Staci Adams, Sarah Lindley, Dr. Binbin Luo, Sara bonabi, Evan Vickers, A'Lester Allen, and Prof. Hongmei Wang; Peers from Shaowei Chen's lab: Dr. Peiguang Hu, Dr. Limei Chen, Dr. Mauricio Rojas-Andrade, Dr. Samantha Sweeney, Dr. Jia Lu, Dr. Yi Peng, Bingzhang Lu, Rene Mercado, Gustavo Chata, and Qiming Liu; Peers from Prof. Alexander Ayzner's lab: Michael Roders, Will Hollingsworth, Carmen Segura, Pamela Schleissner and Gregory Pitch; Peers from Prof. Pradip Mascharak's lab: Dr. Jorge Jimenez, and Dr. Miguel Pinto; Peers from Prof. Yuan Ping's lab: Tyler Smart; Peers from Prof. Frank Bud Bridges's lab: Cameron MacKeen.

I cannot complete my research works without professional external collaborators. I appreciate Prof. Xihong Lu, Prof. Yexiang Tong, Dr. Mingyang Li, and Haozhe Zhang at Sun Yat-Sen University, Dr. Lei Zhang at the Wuhan University of Technology, Prof. Jun Zhou, Prof. Liang Huang, Xiang Gao at Wuhan National Laboratory for Optoelectronics and Huazhong University of Science and Technology for their enthusiastic help in materials characterization; Scientists at Lawrence Livermore National Lab: Dr. Marcus Worsley, Dr. Cheng Zhu, Dr. Swetha Chandrasekaran, Dr. Fang Qian, Dr. Eric Duoss, Dr. Christopher Spadaccini, Dr. Miguel A. Salazar de Troya, Dr. Victor Becker, with whom we worked together on the exciting projects on 3D printed supercapacitors.

Last but not least, I need to thank my family. I would thank my parents for their understanding of my decision five years ago when I decided to pursue my Ph.D. in the USA. I know it was not a relaxed feeling for them when most of my friends at my age had chosen a more stable life. I did not have a chance to go back to visit them within these five years. But I missed them so much every moment. I would like to especially thank my wife, Dr. Jing Zhang, for her understanding and following me these years. I know she could have a lot of better choices in her career after she received her Ph.D. degree years ago. But she chose to accompany me in this new place. She sacrificed a lot for me, and I will never forget all the things she has done for me. I would also like to thank my two kids, Julie Yao and Tyler Yao. Your birth to this beautiful world has brought me numerous joy and happiness. The hard but sweet experience for being their parents gives me a more in-depth understanding of my parents, who raised me and have worried me for so many years. Thank you all for being in my life. I love you all so much!

The text of this dissertation includes reprints of the following previously published or subsequently published materials:

1. **Yao, B.**, Huang, L., Zhang, J., Gao, X., Wu, J., Cheng, Y., Xiao, X., Wang, B., Li, Y., Zhou, J. Flexible Transparent Molybdenum Trioxide Nanopaper for Energy Storage, *Adv. Mater.*, 2016, ***28***, 6353-6358.

2. **Yao, B.**, Li, M., Zhang, J., Zhang, L., Song, Y., Xiao, W., Cruz, A., Tong, Y., Li, Y. TiN Paper for Ultrafast-Charging Supercapacitors, *Nano-Micro Lett.*, 2020, ***12***, 3.
3. **Yao, B.**, Zhang, J., Kou, T., Song, Y., Liu, T., Li, Y. Paper-Based Electrodes for Flexible Energy Storage Devices, *Adv. Sci.*, 2017, ***4***, 1700107.
4. Chandrasekaran, S., **Yao, B. (co-first author)**, Liu, T., Xiao, W., Song, Y., Qian, F., Zhu, C., Duoss, E. B., Spadaccini, C. M., Li, Y., Worsley, M. A. Direct ink writing of organic and carbon aerogels, *Mater. Horiz.*, 2018, ***5***, 1166-1175.
5. **Yao, B.**, Peng H., Zhang H., Kang J., Zhu C., Delgado G., Byrne D., Faulkner S., Freyman M., Lu J., Lu X., Worsley M., Li Y., 3D-Printed Multiscale Pore Carbon Aerogels Enable Efficient Ion and Electron Transport at Ultralow Temperatures, in preparation (2020)
6. **Yao, B.**, Chandrasekaran, S., Zhang, J., Xiao, W., Qian, F., Zhu, C., Duoss, E. B., Spadaccini, C. M., Worsley, M. A., Li, Y. Efficient 3D Printed Pseudocapacitive Electrodes with Ultrahigh MnO_2 Loading, *Joule*, 2019, ***3***, 459-470.
7. **Yao, B.**, Chandrasekaran, S., Zhang, H., Ma, A., Kang, J., Zhang, L., Lu, X., Qian, F., Zhu, C., Duoss, E. B., Spadaccini, C. M., Worsley, M. A., Li, Y. 3D-Printed Structure Boosts the Kinetics and Intrinsic Capacitance of Pseudocapacitive Graphene Aerogels, *Adv. Mater.*, 2020, ***32***, 1906652.

Chapter 1

Introduction of Supercapacitors

Abstract

Climate change and the depletion of fossil fuels drive society to move towards sustainable resources. As a result, we are observing a spike in renewable energy production from sun and wind, as well as the rapid development of electric vehicles or hybrid electric vehicles with lower CO_2 emissions. The sun does not shine during the night, the wind does not blow on demand, but we all expect to drive our cars with at least a few hours of autonomy. Therefore, energy storage systems are becoming to play a more critical role in our lives. Supercapacitors and batteries are the two most investigated electrical energy storage systems. However, we need to improve their performance substantially to meet the ever-increasing requirement of further systems, ranging from portable electronics to hybrid electric vehicles and large industrial equipment. We need to develop new materials and advance our understanding of the electrochemical processes at the nanoscale. In this chapter, the background for energy storage, fundamental concepts of supercapacitors, standard electrochemical characterization techniques, and recent advances in supercapacitor research based on 2D films and 3D printed electrodes will be discussed.

1.1 Basic Principles

The invention of supercapacitors, also called electrochemical capacitors, bridge the gap in between the conventional solid-state and electrolytic electrostatic capacitors and batteries.[1-2] As shown in Figure 1.1, the supercapacitors could store hundreds or thousands of times more charge (tens to hundreds of farads per gram) than the conventional capacitors, because of the carbon materials with much larger surface area (1000-2000 m^2/g) are available for charge storage. However, they have a lower energy density than batteries, which limits the operational discharge time to less than a minute, whereas many applications need more. Supercapacitors were invented in 1957 by Becker, who used a high surface area carbon coated on a metal current collector in a sulphuric acid solution. However, only incremental performance improvement was achieved until the 1990s. The past few years saw the impressive increase in the performance due to the discovery of new electrode materials and improved understanding of ion behavior in small pores, as well as the design of hybrid systems coupling faradic and capacitive electrodes.

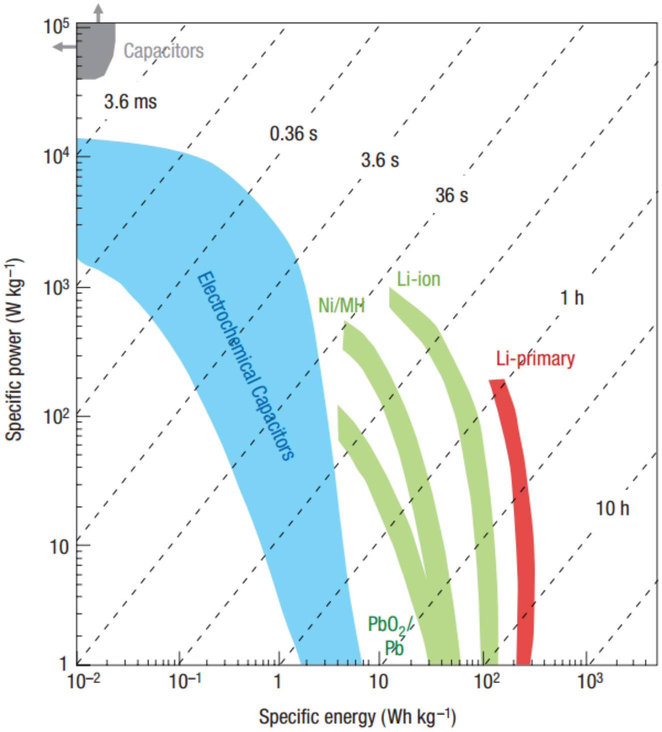

Figure 1.1 Specific power vs. specific energy, also called a Ragone plot, for various electrical energy storage devices. If a supercapacitor is employed in an electric vehicle, the specific power means how fast the car can go, and the specific energy means how long the car can go on a single charge. Time displayed in the figures are the time constants of the devices, obtained by dividing the specific energy by the specific power.[2]

Supercapacitors share a similar configuration of batteries, which are typically consisted of four parts, electrodes, electrolyte, separator, and current collectors. Electrodes can be further divided into positive electrodes (cathode) and negative electrodes (anode). For asymmetric supercapacitors, the positive electrode and negative electrode can be the same materials. For an asymmetric supercapacitor, they have different compositions. According to the types of the electrolyte, electrolytes can be classified into liquid-based electrolytes, gel (quasi-solid state) electrolytes, and solid-state electrolytes. The liquid-based electrolyte can be further categorized into aqueous electrolytes and organic electrolytes. Since the focus of this dissertation is the high-performance novel electrodes, the other three parts will not be further discussed.

1.2 Mechanisms

In general, the supercapacitors can be classified into electric double-layer capacitors (EDLC) and pseudocapacitors according to their charge storage mechanisms.

In EDLC, energy is stored by separation of charges in a Helmholtz double layer at the interface between the electrode surface and electrolyte. Suppose the conductive electrode material is negatively charged. The negatively charged electrons near the electrode surface will attract cations in the electrolyte due to the electrostatic attraction. These anchored cations align with each other and form a compact layer called the inner Helmholtz layer (IHL). The counter-ions establish the second layer, e.g., anions, in this case, built above the IHL and named outer Helmholtz layer (OHL). The OHL is typically packed loosely and less ordered than the IHL. That is because the electrostatic attraction force between the counter ions in IHL and OHL is weakened by the dielectric nature of the solvent and the solvation shells surrounding the counter ions. The IHL and OHL together are termed as an electrical double layer. The thickness of the electric double layer is dependent on the size of electrolyte ions, the concentration of electrolytes, and the charge density on the electrode surface. It is typically less than 10 nm. Accordingly, the double-layer capacitance is generally between 5 and 20 $\mu F/cm^2$.[3] Increasing the accessible surface area and improving the conductivity of the electrode materials can result in higher electrical double layer capacitances. Carbon materials store charges mainly via the formation of electrical double layers.

Different from the EDLC, pseudocapacitors store energy from pseudocapacitive reactions. There are three widely accepted pseudocapacitive reactions, (1) under-potential deposition; (2) Near-surface redox reaction; and (3) Fast ion insertion and extrusion without phase change.

The under-potential deposition is to deposit a species at a potential that is lower than its theoretical potential. For example, the deposition of lead film on gold substrates. But this method is rarely been studied for supercapacitors due to its limited capacitance because of the tiny active materials loading (only single atom thick layer), slow kinetics, and poor reversibility.

The near-surface redox reaction is the most common type of pseudocapacitive reaction among the three. The charge is stored via the valence change on the thin layer of active materials. For example, during the charging process of ruthenium dioxide (RuO_2), a negative bias is applied, and electrons are injected into the RuO_2, accompanying with the valence change of Ru^{4+} to Ru^{3+}. To balance the overall charge of the entire electrode, protons in the electrolyte will diffuse into ruthenium dioxide. The energy is stored in the lower valance state of pseudocapacitive materials in this near-surface region of the electrodes.

Another type of pseudocapacitive reaction is the fast ion insertion/desertion of electrolyte ions in active materials. This process is similar to the intercalation/deintercalation process for Li-ion battery. The difference is there is no phase change for the pseudocapacitive reaction, while the phase will change for battery materials. Representative materials that belong to this category are layered metal oxides, such as orthorhombic niobium pentoxide (T-Nb_2O_5),[4] hexagonal tungsten trioxide (h-WO_3)[5] and orthorhombic molybdenum trioxide (α-MoO_3)[6-7].

1.3 Performance Evaluation

The electrochemical performance of single electrode material or supercapacitor device can be evaluated via several different electrochemical techniques, such as cyclic voltammetry, chronopotentiometry, and electrochemical impedance spectroscopy. Several metrics can be calculated and used to make comparisons with other materials and devices, including gravimetric/areal/volumetric capacitance, energy density, and power density, etc.

1.3.1 Electrochemical Techniques

Cyclic voltammetry (CV) is a type of electrochemical technique that measures the current that develops in an electrochemical cell under conditions where the working potential is ramped linearly versus time to the set potential and then ramped in the opposite direction to return the initial potential. The current at the working electrode is plotted versus the applied potential/voltage to give a cyclic voltammogram.

Chronopotentiometry (CP) is a galvanostatic method in which the current is at the working electrode is held at a constant value for a given time. The potential/voltage and current are recorded as a function of time.

Electrochemical impedance spectroscopy (EIS) is an electrochemical technique to measure the impedance of a system in the response of the AC potentials frequency.

1.3.2 Metrics

The areal capacitance (C_A), gravimetric capacitance (C_G), and volumetric capacitance (C_V) of single electrodes were calculated based on the galvanostatic charging and discharging curves, respectively.

$$C_A = \frac{I \times t}{\Delta U \times A}$$

$$C_G = \frac{I \times t}{\Delta U \times m}$$

$$C_V = \frac{I \times t}{\Delta U \times V}$$

Where C_A, C_G and C_V are the areal, gravimetric and volumetric capacitance (F cm^{-2}, F g^{-1} or F cm^{-3}), ΔU is the potential window (V), I is the discharge current (A), t is the discharge time (s), m is the mass loading of the materials on the electrodes (g), A is the geometric electrode working area (cm^2), and V is the volume of the electrodes (cm^3). For the asymmetric supercapacitor devices, m is the total mass of two electrodes (g), A is the geometric electrode working area (cm^2) and V is the volume of the two electrodes (cm^3).

The areal energy density (E, mWh cm^{-2}) and power density (P, mW cm^{-2}) of the asymmetric device are calculated using the following equations:

$$E_A = \frac{1000}{2 \times 3600} C_A U^2$$

$$P_A = \frac{3600 \times E_A}{t}$$

Where C_A is the areal capacitance (F cm^{-2}), U is the working voltage (V), and t is the discharging time (s) measured in the galvanostatic charging and discharging experiments.

The gravimetric energy density (E, Wh kg^{-1}) and power density (P, W kg^{-1}) of the asymmetric device are calculated using the following equations:

$$E_G = \frac{1000}{2 \times 3600} C_G U^2$$

$$P_G = \frac{3600 \times E_G}{t}$$

Where C_G is the gravimetric capacitance (F g^{-1}), U is the working voltage (V) and t is the discharging time (s) measured in the galvanostatic charging and discharging experiments.

The volumetric energy density (E, mWh cm^{-3}) and power density (P, mW cm^{-3}) of the asymmetric device are calculated using the following equations:

$$E_V = \frac{1000}{2 \times 3600} C_V U^2$$

$$P_V = \frac{3600 \times E_V}{t}$$

Where C_V is the volumetric capacitance (F cm^{-3}), U is the working voltage (V) and t is the discharging time (s) measured in the galvanostatic charging and discharging experiments.

1.3.3 Kinetics Analysis

There are three charge storage mechanisms: the non-faradaic contribution from the formation of the electric double layer, the faradaic contribution (pseudocapacitance) from charge-transfer processes of surface atoms, and the ion insertion process.[8-10] The first two charge storage processes are fast-kinetic processes, which are not limited by ion diffusion. The ion insertion process is a diffusion-controlled process.[11]

Cyclic voltammetry can provide a great insight into the difference in charge storage kinetics. By analyzing the current dependence on the sweep rate, v, the nature of the kinetic processes of the electrode materials can be obtained. Both equations of $i = kv^b$ and $i = k_1 v + k_2 v^{0.5}$ can be used to determine the kinetic behavior.

For the equation of $i = kv^b$, both k and b are adjustable parameters, with b-value determined from the slope of log i vs. log v. There are two well-defined conditions: $b=0.5$ and $b=1$. For the $b=0.5$, the current is proportional to the square root of the scan rate, v, according to the following equation:

$$i = nFAC^{*}D^{1/2}v^{1/2}(\alpha nF/RT)^{1/2}\pi^{1/2}\chi(bt)$$

where C^* is the surface concentration of the electrode material, α is the transfer coefficient, D is the chemical diffusion coefficient, n is the number of electrons involved in the electrode reaction, A is the surface area of the electrode material, F is the Faraday constant, R is the molar gas constant, T is the temperature, and the $\chi(bt)$ function is the normalized current for a totally irreversible system as indicated by the cyclic voltammetry response. The current response in Equation 10 is diffusion controlled, which is indicative of a faradaic intercalation process.

b=1 represents a capacitive response because the capacitive current is proportional to the sweep rate, according to the following equation:

$$i = vC_dA$$

where C_d is the capacitance.

Under different potentials, the b value can vary between 0.5 to 1, depending on the specific potential required for the faradaic reactions. The values of b determined by equation $i = kv^b$ can tell whether an electrochemical process is dominated by a capacitive process or diffusion-controlled process, but it is unable to quantify the contribution from each process.

The equation ($i = k_1 v + k_2 v^{0.5}$) can further distinguish the fraction of current contributed from the surface capacitive effects and diffusion-controlled insertion processes by determining the values of k_1 and k_2. $k_1 v$ and $k_2 v^{1/2}$ correspond to the current contributions from the fast-kinetic processes (surface capacitive process) and the show-kinetic processes (diffusion-controlled intercalation process), respectively.

A method reported by Prof. Bruce Dunn's group to quantify the capacitance contribution from fast-kinetic processes and slow-kinetic processes. First, the current density at a fixed potential and scan rate, i, was extracted from the CV curves. The current density, i, is a function of scan rate, v, and can be expressed as the sum of two items v:

$$i = k_1 v + k_2 v^{0.5}$$

where k_1 and k_2 are constants. $k_1 v$ and $k_2 v^{0.5}$ represent the current contribution of fast kinetic (or capacitive-controlled) process and slow kinetic (or diffusion-controlled) process, respectively. Dividing $v^{0.5}$ into both sides of the above equation gives:

$$iv^{-0.5} = k_1 v^{0.5} + k_2$$

By plotting $iv^{-0.5}$ as a function of $v^{0.5}$, k_1 (slope) and k_2 (y-axis intercept) can be determined. The calculation was repeated for each potential to determine the contribution from fast kinetic and slow kinetic processes.

The ion diffusion resistance (σ) was determined from a plot of the real part of impedance (Z’) in the EIS spectrum as a function of the square root of frequency ($\omega^{-0.5}$) in the intermediate frequency range. The slopes of the linear fitting line of this plot are the values of the ion diffusion resistance, which is also called Warburg coefficient.

1.4 Recent Research Advances

The rapid development of supercapacitors has been taken place over the past decade due to the emerging of many new materials and novel device configurations. The following parts will discuss the recent advances in the supercapacitors based on 2D film electrodes and 3D printed electrodes.

1.4.2 2D Film Electrodes

Two-dimensional (2D) thin-film electrode represents the most widely used form of supercapacitor electrodes. By coating thin-film materials under the help of polymetric binders and conducting agents on current collectors, such as metal substrates, the electrodes can be used as supercapacitor electrodes.[12] However, due to the rigid nature of most electrodes fabricated in this way, most of them could satisfy the requirements for flexible and wearable electrodes. In addition, the employment of heavy metal substrate, as well as the conducting agents, introduce additional weight to the entire electrodes and devices and lower their energy and power densities. Furthermore, the non-conductive nature of polymer binders in the electrode increases the resistance of electrodes and decreases the power performance of the supercapacitors. To address these challenges for the conventional 2D film electrodes, freestanding electrodes with good flexibility, lightweight, high conductivity, and excellent capacitances are proposed and attracted worldwide research interests.

2D film electrodes can be mainly divided into two categories. The first category is the electrodes with active materials loaded on flexible substrates, such as papers or plastics.[13-14]

The second category is the freestanding films with pure active materials or the mixture of less-conductive materials and conducting materials.[15-17] The pure freestanding 2D films can be graphene,[18] carbon nanotubes,[19] carbon fibers,[20] et al. However, these carbon materials typically suffer from the low capacitances because they store charges mainly via forming electrical double layers, which could only provide limited capacitances. Some other materials, such as 1T-MoS_2,[21] MXenes,[22], which also have high conductivity, were investigated as pure 2D film electrodes as well. But their stability is still not satisfying. To increase the capacitance in 2D film electrodes, hybrid films are designed and fabricated. The hybrid films mix the electrode materials with high capacitance, such as metal oxides, metal sulfides, or metal nitrides with highly conductive carbon, such as graphene and CNTs.[23-25] The high capacitive modules in the 2D hybrid films act as the charge storage center, while the interconnected graphene or CNTs networks help to effectively transfer the charges. Yet for most of these 2D film electrodes, their capacitances and power performance are still inferior to the counterparts in the conventional electrodes with additional current collectors and conducting agents. Improving the capacitance and fast-charging properties of the 2D films are still challenging for this area.

1.4.3 3D Printed Electrodes

3D printed electrodes are a class of new type of electrodes for energy storage.[26-27] Compared to the conventional 2D film electrodes with tens of micrometers, 3D printed electrodes substantially increase the thickness of electrodes as well as the mass loading of active materials. They could store charge several orders higher than the 2D thin-film electrodes, while retaining sound electrochemical performance, which is not possible for conventional electrodes.

Carbon materials are the first research model for 3D printed electrodes of supercapacitors due to their high conductivity, tuned morphology, and high surface areas.[28] 3D printed graphene aerogels have shown impressive rate performance that is equivalent to their counterparts that are hundreds or thousands thinner.[29] The open channels in the 3D printed electrode offer the free path for electrolyte ions to aggregate on the surface of active materials rapidly. This is especially important for supercapacitors, which require fast charging and discharging. However, the electrochemical performance of the conventional 2D film electrodes will typically deteriorate with the increase of mass loadings.[30-31] The thick compact film electrode does not allow the electrolyte ions to effectively transport to the interior part of the electrode, which results in lower utilization of the active materials and thus resulting in lower capacitances.

To further improve the capability of charge storage in the 3D printed electrodes, coating or mixing the metal oxides with the carbon materials, especially graphene, becomes another right choice. Metal oxide in these hybrid structures could store more charges than the pure 3D graphene due to the additional surface redox reactions.[32] Some recent work also employed MXenes as building materials and creased 3D printed pure MXene structures.[33] The high conductivity and high capacitance of the MXenes ensure the high performance of printed electrodes even under high mass loading of the active materials. But due to the large porosity of the 3D printed electrodes, the volumetric capacitance, and energy densities are not comparable with those of compact, thin film.[11] How to improve the volumetric performance while maintaining their high gravimetric and areal performance will be the pursuit of future work.

References

1. P. Simon, Y. Gogotsi, *Nat. Mater.* **2020**.
2. P. Simon, Y. Gogotsi, *Nat. Mater.* **2008**, *7*, 845-854.
3. D. Sheberla, J. C. Bachman, J. S. Elias, C.-J. Sun, Y. Shao-Horn, M. Dincă, *Nat. Mater.* **2016**, *16*, 220.
4. V. Augustyn, J. Come, M. Lowe, J. Kim, P. Taberna, S. Tolbert, H. Abruna, P. Simon, B. Dunn, *Nat. Mater.* **2013**, *12*, 518-522.
5. M. Zhu, W. Meng, Y. Huang, Y. Huang, C. Zhi, *ACS Appl. Mater. Interfaces* **2014**, *6*, 18901-18910.
6. T. Brezesinski, J. Wang, S. H. Tolbert, B. Dunn, *Nat. Mater.* **2010**, *9*, 146-151.
7. H. S. Kim, J. B. Cook, H. Lin, J. S. Ko, S. H. Tolbert, V. Ozolins, B. Dunn, *Nat. Mater.* **2017**, *16*, 454-460.

8. H. Lindström, S. Södergren, A. Solbrand, H. Rensmo, J. Hjelm, A. Hagfeldt, S.-E. Lindquist, *J. Phys. Chem. B* **1997**, *101*, 7717-7722.

9. J. Wang, J. Polleux, J. Lim, B. Dunn, *J. Phys. Chem. C* **2007**, *111*, 14925-14931.

10. T. Liu, Z. Zhou, Y. Guo, D. Guo, G. Liu, *Nat. Commun.* **2019**, *10*, 675.

11. B. Yao, S. Chandrasekaran, H. Zhang, A. Ma, J. Kang, L. Zhang, X. Lu, F. Qian, C. Zhu, E. B. Duoss, C. M. Spadaccini, M. A. Worsley, Y. Li, *Adv. Mater.* **2020**, *32*, 1906652.

12. J. Li, K. Liu, X. Gao, B. Yao, K. Huo, Y. Cheng, X. Cheng, D. Chen, B. Wang, D. Ding, M. Liu, L. Huang, *ACS Appl. Mater. Interfaces* **2015**, *7*, 24622-24628.

13. B. Yao, J. Zhang, T. Kou, Y. Song, T. Liu, Y. Li, *Adv. Sci.* **2017**, *4*, 1700107.

14. L. Yuan, B. Yao, B. Hu, K. Huo, W. Chen, J. Zhou, *Energy Environ. Sci.* **2013**, *6*, 470-476.

15. B. Yao, L. Huang, J. Zhang, X. Gao, J. Wu, Y. Cheng, X. Xiao, B. Wang, Y. Li, J. Zhou, *Adv. Mater.* **2016**, *28*, 6353-6358.

16. L. Huang, B. Yao, J. Sun, X. Gao, J. Wu, J. Wan, T. Li, Z. Hu, J. Zhou, *J. Mater. Chem. A* **2017**, *5*, 2897-2903.

17. B. Yao, M. Li, J. Zhang, L. Zhang, Y. Song, W. Xiao, A. Cruz, Y. Tong, Y. Li, *Nano-Micro Lett.* **2020**, *12*, 3.

18. M. El-Kady, V. Strong, S. Dubin, R. Kaner, *Science* **2012**, *335*, 1326-1330.

19. Z. Q. Niu, W. Y. Zhou, J. Chen, G. X. Feng, H. Li, W. J. Ma, J. Z. Li, H. B. Dong, Y. Ren, D. A. Zhao, S. S. Xie, *Energy Environ. Sci.* **2011**, *4*, 1440-1446.

20. Y. Cheng, L. Huang, X. Xiao, B. Yao, L. Yuan, T. Li, Z. Hu, B. Wang, J. Wan, J. Zhou, *Nano Energy* **2015**, *15*, 66-74.

21. M. Acerce, D. Voiry, M. Chhowalla, *Nat. Nanotechnol.* **2015**, *10*, 313-318.

22. M. Ghidiu, M. Lukatskaya, M. Zhao, Y. Gogotsi, M. Barsoum, *Nature* **2014**, *516*, 78-81.

23. J. Wu, X. Gao, H. Yu, T. Ding, Y. Yan, B. Yao, X. Yao, D. Chen, M. Liu, L. Huang, *Adv Funct Mater* **2016**, *26*, 6114-6120.

24. S. Wang, J. Zhu, Y. Shao, W. Li, Y. Wu, L. Zhang, X. Hao, *Chem. Eur. J.* **2017**, *23*, 3438-3446.

25. X. Xiao, X. Peng, H. Jin, T. Li, C. Zhang, B. Gao, B. Hu, K. Huo, J. Zhou, *Adv. Mater.* **2013**, *25*, 5091-5097.

26. A. Ambrosi, M. Pumera, *Chem. Soc. Rev.* **2016**, *45*, 2740-2755.

27. M. P. Browne, E. Redondo, M. Pumera, *Chem. Rev.* **2020**.

28. T. Y. Liu, F. Zhang, Y. Song, Y. Li, *J. Mater. Chem. A* **2017**, *5*, 17705-17733.

29. C. Zhu, T. Liu, F. Qian, T. Han, E. Duoss, J. Kuntz, C. Spadaccini, M. Worsley, Y. Li, *Nano Lett.* **2016**, *16*, 3448-3456.

30. Y. He, W. Chen, X. Li, Z. Zhang, J. Fu, C. Zhao, E. Xie, *ACS Nano* **2013**, *7*, 174-182.

31. L. Hu, W. Chen, X. Xie, N. Liu, Y. Yang, H. Wu, Y. Yao, M. Pasta, H. Alshareef, Y. Cui, *ACS Nano* **2011**, *5*, 8904-8913.

32. B. Yao, S. Chandrasekaran, J. Zhang, W. Xiao, F. Qian, C. Zhu, E. B. Duoss, C. M. Spadaccini, M. A. Worsley, Y. Li, *Joule* **2019**, *3*, 459-470.

33. W. Yang, J. Yang, J. J. Byun, F. P. Moissinac, J. Xu, S. J. Haigh, M. Domingos, M. A. Bissett, R. A. W. Dryfe, S. Barg, *Adv. Mater.* **2019**, *31*, e1902725.

Chapter 2

Molybdenum Trioxide Nanopaper for Supercapacitors

Abstract

Free-standing paper-like film with excellent transparency and flexibility holds great potential to serve as a transparent electrode for wearable electronics and energy storage. Transition metal oxide have shown their huge potential for energy storage due to their high capacitance and stability. Nevertheless, the fabrication of ultrathin transparent paper electrode via the assembly of 1D transition metal oxide nanostructure has never been reported. Orthorhombic molybdenum trioxide (α-MoO_3), transition metal oxide with layered structures, has been recognized as a promising electrode for energy storage. In this work, the fabrication of flexible and transparent MoO_3 nanopapers via assembly of ultralong molybdenum trioxide nanobelts (MoO_3 NBs) is demonstrated. The well-dispersed, ultralong MoO_3 NBs with an average length of 200 μm have been synthesized via a hydrothermal method. A flexible transparent molybdenum trioxide nanopaper via the assembly of these ultralong nanobelts displays an excellent average transmittance of 90% in the visible region. Significantly, the freestanding nanopaper electrode delivers an outstanding specific capacitance of 1198 F g^{-1} at 2 mV s^{-1}, which is just slightly below the theoretical value of molybdenum trioxide (1256 F g^{-1}). The excellent specific capacitance can be ascribed to the efficient ion diffusion in the 3D structure and the very thin nanobelts, as well as the reduced distance of electron transport from transparent nanopaper electrode to current collector.

2.1 Introduction

Free-standing paper-like film with excellent transparency and flexibility hold great potentials to serve as transparent electrode for applications such as thin-film transistor,[1-2] solar cell,[3] organic light emitting diodes,[4] smart window,[5] generator,[6] lithium ion battery,[7] and supercapacitors.[8] Transition metal oxide nanostructures, due to their low-cost and rich chemical nature, have been widely investigated as active materials for energy storage application. However, the added non-conductive binders like polytetrafluoroethylene (PTFE) or polyvinylidene fluoride (PVDF) during electrode preparation increase the electrode resistance.[9-11] Various conductive materials such as graphene and carbon nanotubes have been employed to fabricate composite film with transition metal oxides to reduce their resistance.[12-13] However, the compactness as well as light absorption of graphene and carbon nanotubes in these hybrid films impedes them to be transparent. Flexible free-standing transition metal oxide electrodes without conductive agents and binders have been developed in recent years.[14-15] Nevertheless, the fabrication of ultrathin transparent paper electrode *via* the assembly of 1-D transition metal oxide nanostructure has never been reported.

Orthorhombic molybdenum trioxide (α-MoO_3), transition metal oxide with layered structures, has been recognized as a promising electrode for energy storage.[11] A number of MoO_3 nanostructures including nanoparticle,[16] nanoplate,[17] nanorod,[18] nanowire,[19] nanotube[20] and nanobelt,[21] have been reported. Among them, 1-D MoO_3 nanobelts have received much attention due to its unique structural anisotropy. However, most of the MoO_3 nanobelts reported in previous works are relatively short with length of several micron or easy to aggregate into bundles, which are difficult to be assembled for forming free-standing ultrathin nanopaper.[9, 11, 13, 15, 22-24] In this work, we have successfully synthesized ultralong molybdenum trioxide nanobelts with average length of 200 μm and well-dispersive nature *via* a hydrothermal method. A flexible transparent molybdenum trioxide nanopaper *via* the assembly of these ultralong nanobelts displays an excellent average transmittance of 90% in the visible region. Significantly, the free-standing nanopaper electrode delivers an outstanding specific capacitance of 1198 F/g at 2 mV/s, which is just slightly below the theoretical value of molybdenum trioxide (1256 F/g).[25] The excellent specific capacitance can be ascribed to the efficient ion diffusion in the 3D structure and very thin nanobelts as well as the reduced distance of electron transport from transparent nanopaper electrode to current collector. The nanopaper based supercapacitor device also shows an excellent long-term stability performance over 20000 cycles with a retention rate of 96.5 %.

2.2 Experimental Section

Synthesis of ultralong molybdenum trioxide nanobelts: Ultralong molybdenum trioxide was synthesized via a modified hydrothermal method. Typically, 2.000 g molybdenum power (Aladdin, 99.5%) was added into 10 mL deionized water to form a uniform mixture. Then 20.0 mL 30.0 % (wt.%) H_2O_2 was slowly added until the solution became light-yellow. The solution was continued to stir for 30 min to react thoroughly. After that, the solution was transferred to a Teflon-lined stainless steel autoclave and heated to 220 °C for 3 h to 168 h. The precipitate was filtered and rinsed by deionized water and ethanol for several times.

Preparation of transparent molybdenum trioxide nanopapers: Vacuum filtration method was employed to fabricate molybdenum trioxide nanopapers. First, 0.82 mg molybdenum trioxide nanobelts were dispersed in 50.0 ml deionized water to form a homogeneous suspension. Then, the as-prepared suspension was filtered though a membrane (220 nm pore size). After filtration, a nanopaper formed on the membrane was dried in air for 5 min and then was peeled off from the filter membrane to get a free-standing transparent nanopaper. For comparison, nanopapers with different mass loading of molybdenum trioxide nanobelts (from 1.64 to 26.24 mg) were assembled via the same procedure.

Preparation of flexible solid-state supercapacitor: The PVA/LiCl gel electrolyte was prepared as follow: 6.000 g of LiCl and 6.000 g of PVA were added to 60.0 ml deionized water, and then the mixture was heated to 85 °C under vigorous stirring until the solution became clear. The transparent molybdenum trioxide nanopaper was pressed on the gold-coated polyethylene terephthalate (PET) conductive substrate, and then a PVA/LiCl transparent film was sandwiched in between to work as both electrolyte and separator. After that, the device was left in 60 °C for 12 h to remove excess water in the electrolyte.

Characterization: The X-ray diffraction patterns were collected on a powder X-ray diffractometer (Philips X' Pert Pro) with Cu Kα radiation (λ = 1.54184 Å).The morphology of ultralong molybdenum trioxide nanobelts were investigated using field emission scanning electron microscope (FESEM, FEI Nova 450 Nano) and transmission electron microscope (TEM, Tecnai G20). Fourier transform infrared spectroscopy (FTIR) analysis of the materials was performed on a VERTEX 70 (Bruker) with the wave number range of 400-4000 cm^{-1}. Raman spectroscopy was conducted using a RenishawInvia Raman microscope spectrometer. The optical transmittance spectra were recorded using a SHIMADZU UV-2550 spectrophotometer. Thermogravimetric and differential scanning calorimetric (TG-DSC) data was recorded on a Netzsch STA 449 F3 thermoanalyzer with air as the carrier gas at a heating rate of 5 °C/min. The electrochemical measurements were carried out using electrochemical workstation (EC-lab VMP-300 and CHI 660). For the typical three electrode test, a piece of 0.2 cm^2 MoO_3 nanopaper film was used as work electrode, Ag/AgCl (CHI, USA), YP-50 (Kuraray Chemical, USA) and Celgard membrane (Celgard, USA) were used as reference electrode, counter electrode and the separator, respectively. The weight of the MoO_3 nanopaper electrode are 0.015, 0.030, 0.061, 0.122, 0.244 and 0.488 mg, respectively. Two-electrode symmetric device was constructed based on two pieces of 0.2 cm^2 MoO_3 nanopaper films with the same area and mass as electrode. All the electrochemical tests were conducted in Swagelok cells (Swagelok, USA).

Calculations: For three electrode system and two electrode supercapacitor devices, the specific capacitance is calculated from the CV area by equations below:

$$Cs = \frac{\int IdV}{2v\Delta Vm}$$

For two electrode supercapacitor devices, the energy density and power density are calculated by equations below:

$$E = \frac{1}{2}Cs(\Delta V)^2$$

$$P = \frac{3600E}{\Delta t}$$

where *Cs* is the specific capacitance (F/g), *I* is the current (A), v is the scan rate (V/s), *m* is the mass loading (g), *V* is the working potential, Δt is the discharging time, *E* is the energy density and *P* is the power density.

2.3 Results and Discussions

Ultralong molybdenum trioxide nanobelts (MoO_3 NB) were synthesized *via* a modified hydrothermal method.[11] Compared with previous reports, higher temperature (220 °C) was employed. Due to the anisotropy of MoO_3 nanobelts, the growth rate in different directions is different. From the thermodynamic viewpoint, the growth along [001] orientation is more favorable, since more Mo-O bond will form and more energy will release accordingly.[26] Therefore, the length of MoO_3 NB synthesized at 220 °C is much longer than its 180 °C counterparts. During the hydrothermal reaction, the orange peroxomolybdic acid solution changed into white suspension of MoO_3 NB. It is noteworthy that MoO_3 NB can be well dispersed in ethanol for one year without any aggregation.

As shown in Figure 2.1a and b, MoO_3 nanobelts have very uniform structure. The length of nanobelts can be tuned *via* controlled variation of hydrothermal reaction time, while the samples prepared at different hydrothermal time have similar width (200-400 nm) and thickness (50-70 nm) (Figure 2.2). The length and the length-to-width (L/D) ratio of MoO_3 NB increase nearly linearly with reaction time (Figure 2.1c). The average length of MoO_3 NB changed from 3 μm to 200 μm and their corresponding L/D ratios increased from 14 to almost 1000, when the reaction time increase from 3 to 168 hours. The greatly increased length and well-dispersive character of ultralong MoO_3 nanobelts enable them to fabricate both the flexible transparent film[10-11, 13, 15, 21-22, 27-29] and single nanobelt device[10-11, 13, 22].

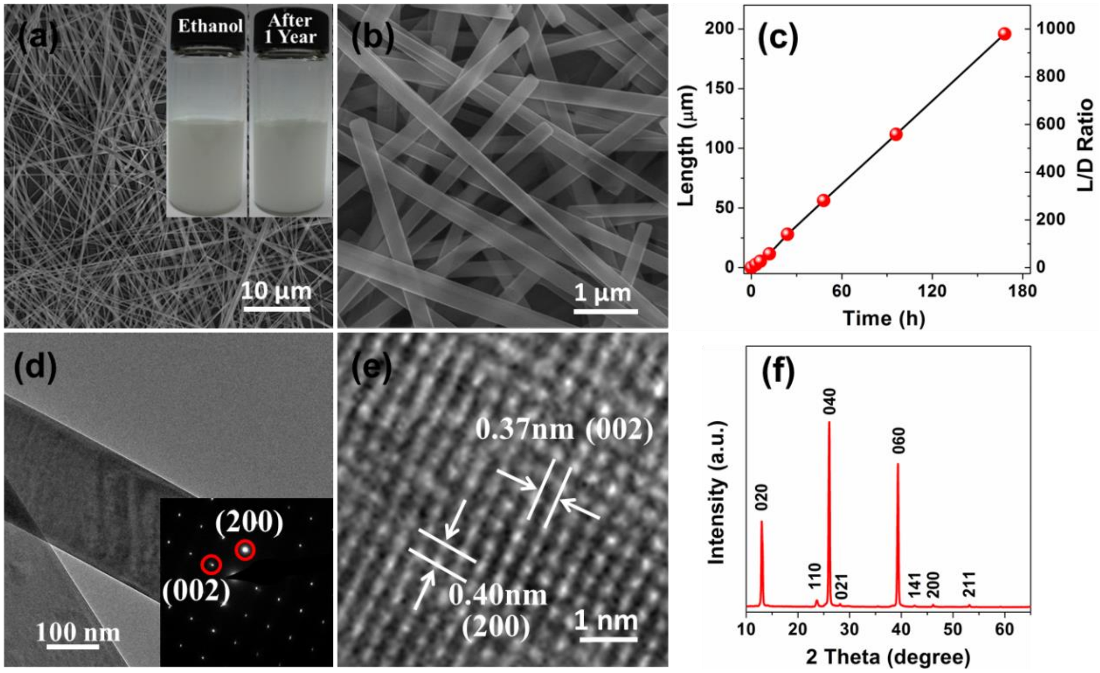

Figure 2.1 (a, b) SEM images of ultralong MoO_3 nanobelts (MoO_3 NB) after 168 hours reaction. The insert in figure 2.1a shows the optical image of MoO_3 NB dispersed in ethanol after reaction and one-year. (c) Length and ratio of length versus to width of MoO_3 NBs under different reaction time. (d) TEM of MoO_3 NB. The insert shows SAED pattern of an individual MoO_3 NB. (e) HR-TEM of an individual MoO_3 NB. (f) XRD pattern of UL-MoO_3 NB after 168 hours reaction.

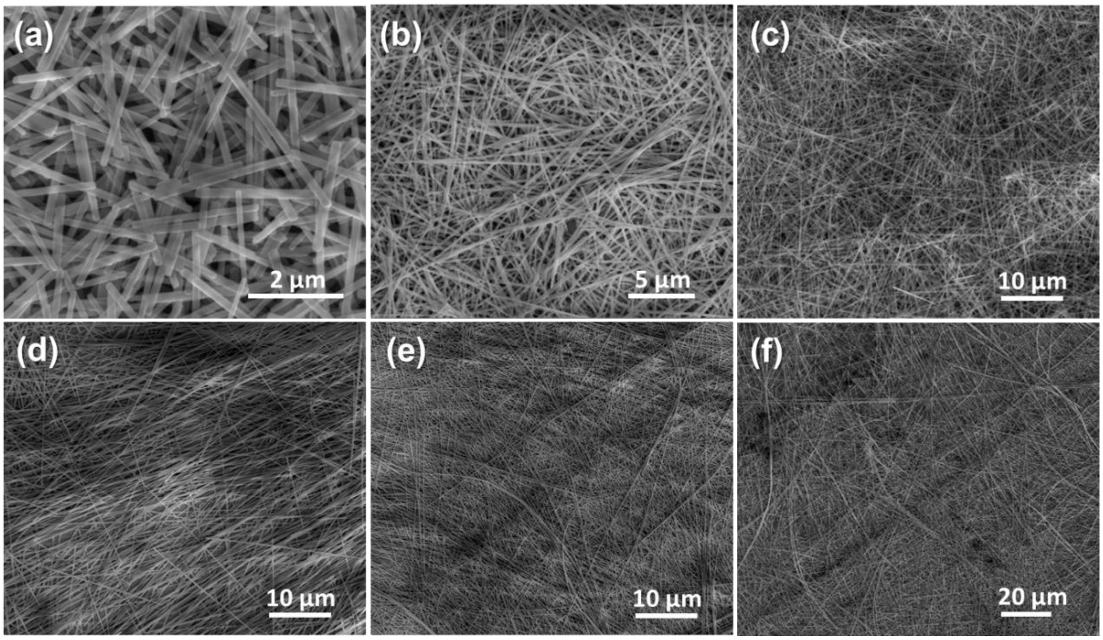

Figure 2.2 SEM images of MoO_3 nanobelts under hydrothermal reaction time of 3 h (a), 6 h (b), 12 h (c), 24 h (d), 48 h (e) and 96 h (f), respectively.

X-ray diffraction (XRD) studies confirmed that the nanobelts are orthorhombic MoO_3 (JCPDS No. 05-0508) (Figure 2.1f, Figure 2.3).[11] The high intensity of (020), (040) and (060) suggests that the nanobelts have a highly ordered orientation in nanopaper.[15] High-resolution transmission electron microscopy images and selected area electron diffraction pattern (Figure 2.1d and 2.1e) further revealed that the nanobelts are single crystal with interplanar spacing of 0.37 nm and 0.40 nm along perpendicular directions, which are consistent to the (002) and (200) *d*-space of MoO_3.[13] Furthermore, Raman and FT-IR spectra collected from NBs show characteristic peaks of MoO_3. TG-DSC analysis suggested that these MoO_3 NBs are thermochemically stable up to 788 °C.

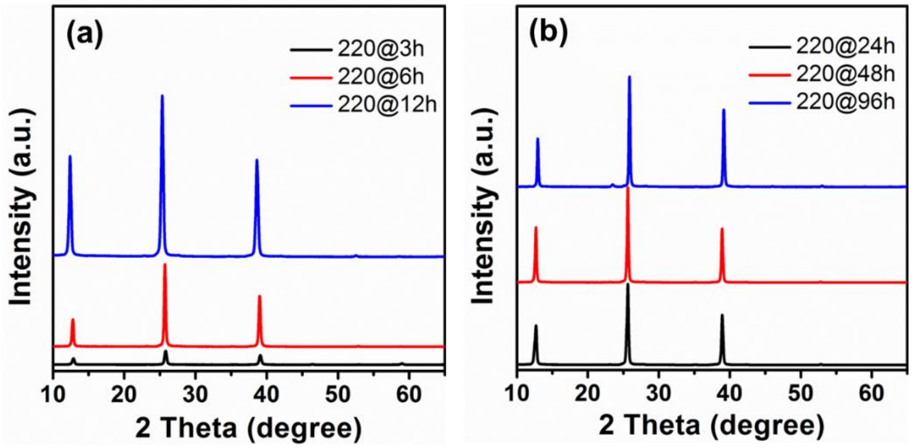

Figure 2.3 XRD patterns of MoO_3 nanobelts under hydrothermal reaction time of 3 h, 6 h and 12 h (a) and 24 h, 48 h and 96 h (b), respectively.

Free-standing transparent nanopaper was fabricated by vacuum filtration of homogeneous MoO_3 NB suspension, followed by peeling off process (Figure 2.4). The transparent MoO_3 NB nanopaper is a three-dimensional network with large pores between nanobelts (Figure 2.5a), which facilitates the ion diffusion in the 3D electrode. Side-view SEM image of the nanopaper shows that the thickness of the nanopaper is about several hundred nanometers, which is only two to three layers of MoO_3 NBs (Figure 2.5b). The thickness can be controlled by tuning the concentration of suspension for vacuum filtration. The ultrathin nanopaper shows excellent transparency in visible region (Figure 2.5d). As shown in Figure 2.5c, the transmittance increases with the decreasing thickness (or mass loading) of nanopaper. For nanopaper with mass loading of 0.076 mg/cm^2, it achieves an excellent average transmittance of ~ 90% in the visible region.

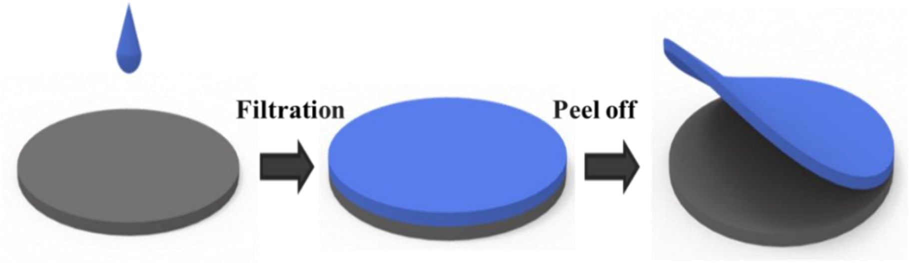

Figure 2.4 Schematic diagram illustrating the process using vacuum filtration method to fabricate MoO_3 nanopaper

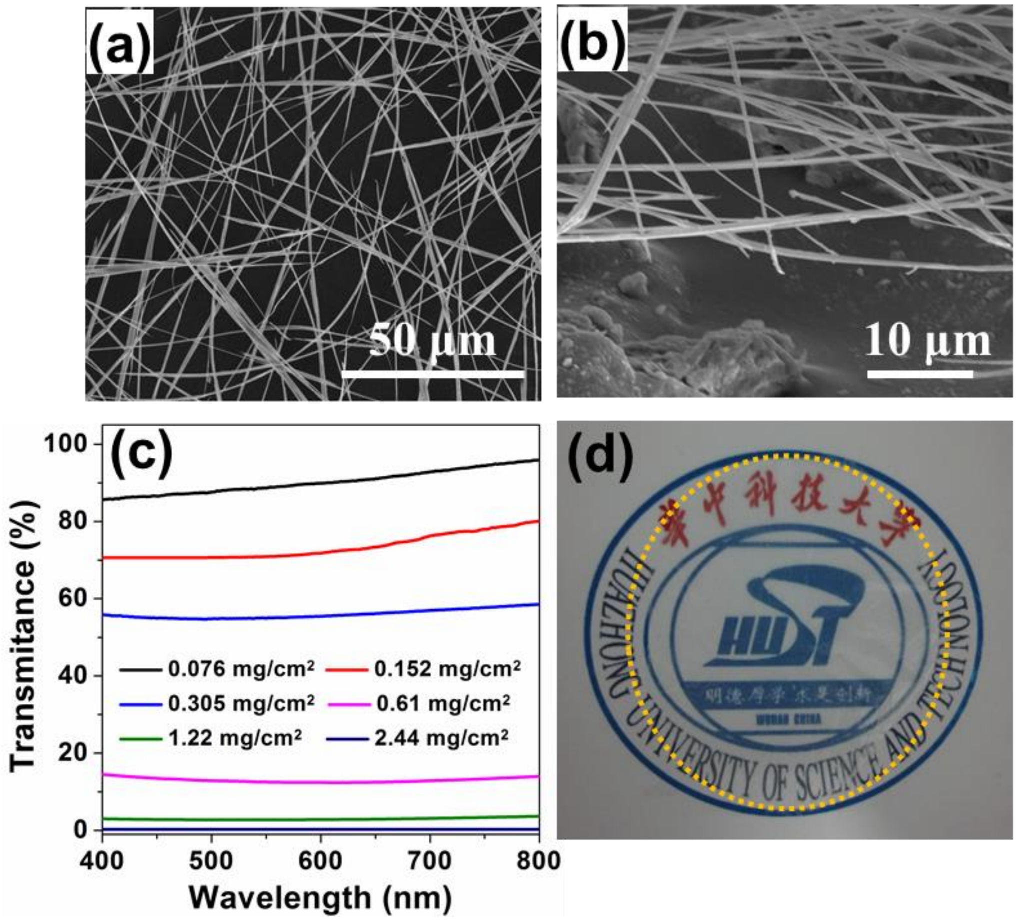

Figure 2.5 (a) SEM image of ultrathin transparent MoO_3 NB nanopaper. (b) Side view of transparent MoO_3 nanopaper. (c) Transmittance spectra of MoO_3 NB nanopapers with different mass loading. (d) Optical image shows excellent transparent character of transparent MoO_3 nanopaper.

Importantly, the nanopapers are mechanically flexible and robust that allows for folding and writing as normal paper. The flexibility and fold ability were tested for both the ultrathin transparent nanopaper (0.076 mg/cm^2) and the opaque thick nanopaper (2.440 mg/cm^2). As shown in Figure 2.6, the transparent nanopaper can be folded for four times and then unfolded. The transmittance of transparent nanopaper decreases with the increase of the folding layers, as expected. No crack was found in the upfolded nanopaper and its transparency was also not affected by the times of folding and unfolding, revealing its excellent mechanically flexibility. The same result was also observed for the opaque nanopaper (Figure 2.7). Besides, these nanopapers can be directly used as a substrate for deposition of other materials. For example, we can write on the nanopaper using an ink brush soaked with carbon nanotube ink (Figure 2.8).

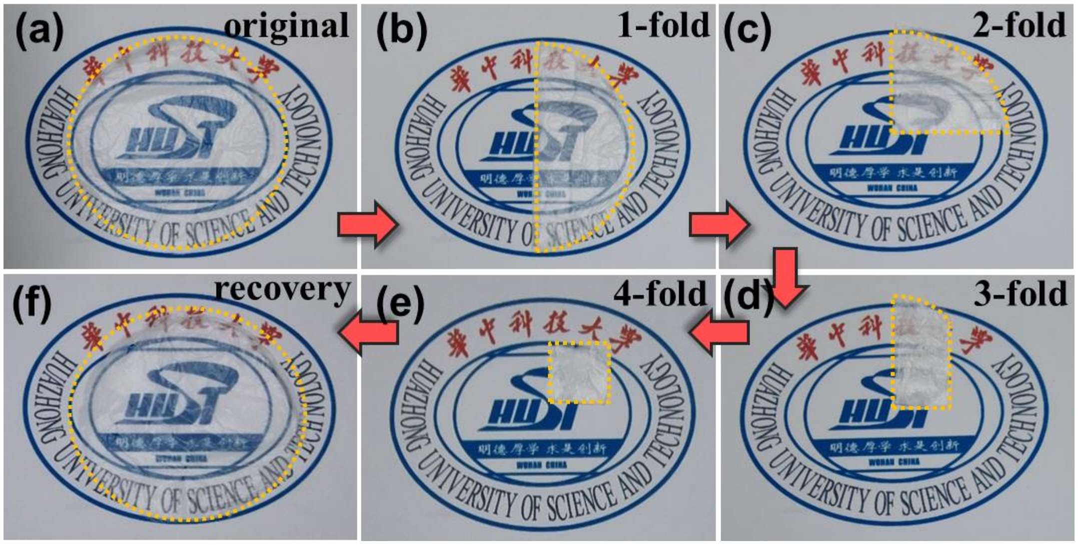

Figure 2.6 Optical images of transparent MoO_3 nanopaper under different times of folding and full recovery.

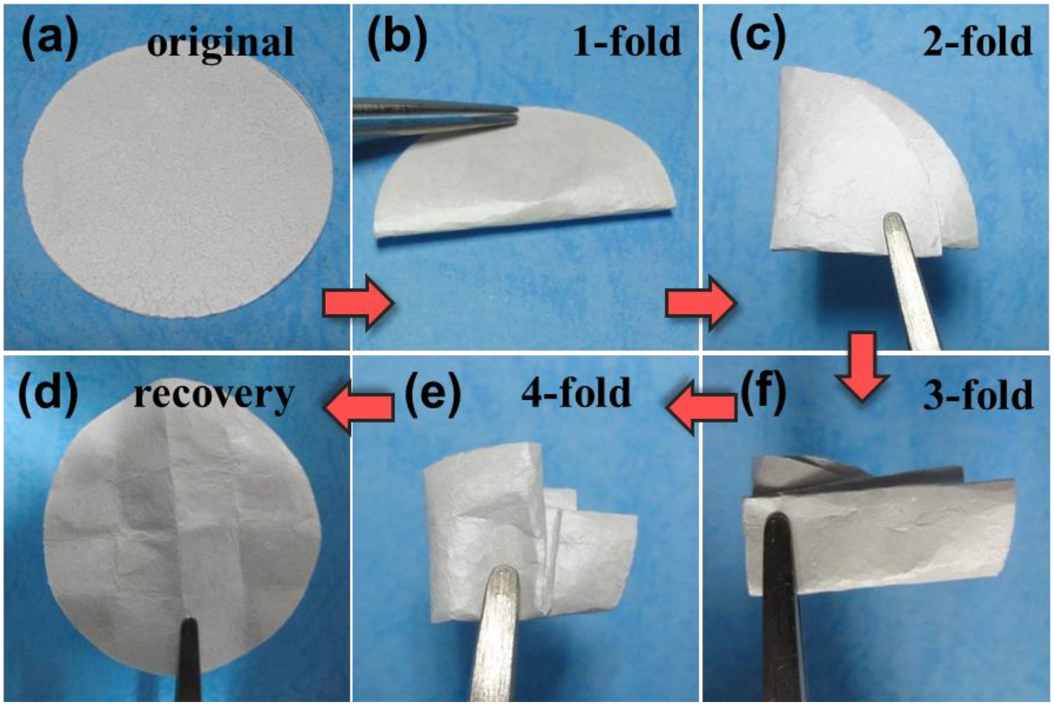

Figure 2.7 Optical images of opaque thick MoO_3 nanopaper under different times of folding and full recovery.

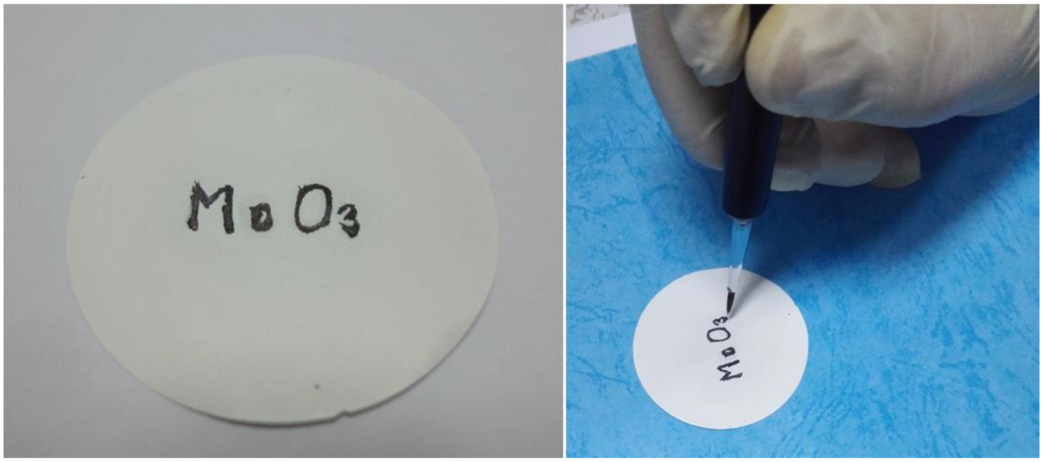

Figure 2.8 Optical image of "MoO_3" written on MoO_3 nanopaper using an ink brush with CNT ink, illustrating a good character to be substrate of this kind of nanopaper.

These unique structural properties enable the nanopapers to be a promising electrode material for supercapacitors.[14, 30-31] In comparison to the traditional method of using conductive agent and binder to prepare composite electrodes, binder-free and conductive agent-free 3-D porous transition metal oxide nanostructures have been proved to be promising in achieving high performance.[13-15] However, the specific capacitances of these nanostructured electrodes are still substantially lower than the theoretical value of corresponding metal oxide. The inadequate utilization of inner active materials and long electron transport in the thick film electrode are ascribed to this low specific capacitance. The ultrathin and flexible feature of MoO_3 NB nanopaper could address these limitations by building up a conductive scaffold, which allows fast ionic diffusion and electron transfer through active materials to current collector.

The electrochemical performance of ultrathin transparent MoO_3 NB nanopaper electrode was evaluated by cyclic voltammetry (CV) and galvanostatic charging and discharging (GCD) in a three-electrode configuration in 5.0 M LiCl electrolyte (Figure 2.9a and 2.9b). As shown in the Figure 2.9a, CV area of ultrathin MoO_3 NB nanopaper electrode is much larger than the thick MoO_3 NB nanopaper electrode under the scan rate of 100 mV/s. Significantly, the specific capacitance of ultrathin MoO_3 NB nanopaper electrode achieved 1198 F/g at the scan rate of 2 mV/s, approaching the theoretical specific capacitance (1256 F/g) of MoO_3 in a working potential window of 0.8 V (Figure 2.9c).[25] This is the highest value reported for MoO_3 based pseudocapacitor electrodes. The excellent specific capacitance can be ascribed to the efficient ion diffusion in thin nanobelts (ion diffusion length less than

35 nm) and the 3D structure as well as the reduced distance of electron transport from ultrathin nanopaper electrode to current collector.[32] Moreover, ultrathin MoO$_3$ NB nanopaper electrode shows outstanding cycling stability with a capacitance retention rate of 99.1 % over 20000 cycles, which is the best cycling performance for MoO$_3$-based energy storage system (Figure 2.9d).[10-13, 25, 32-39]

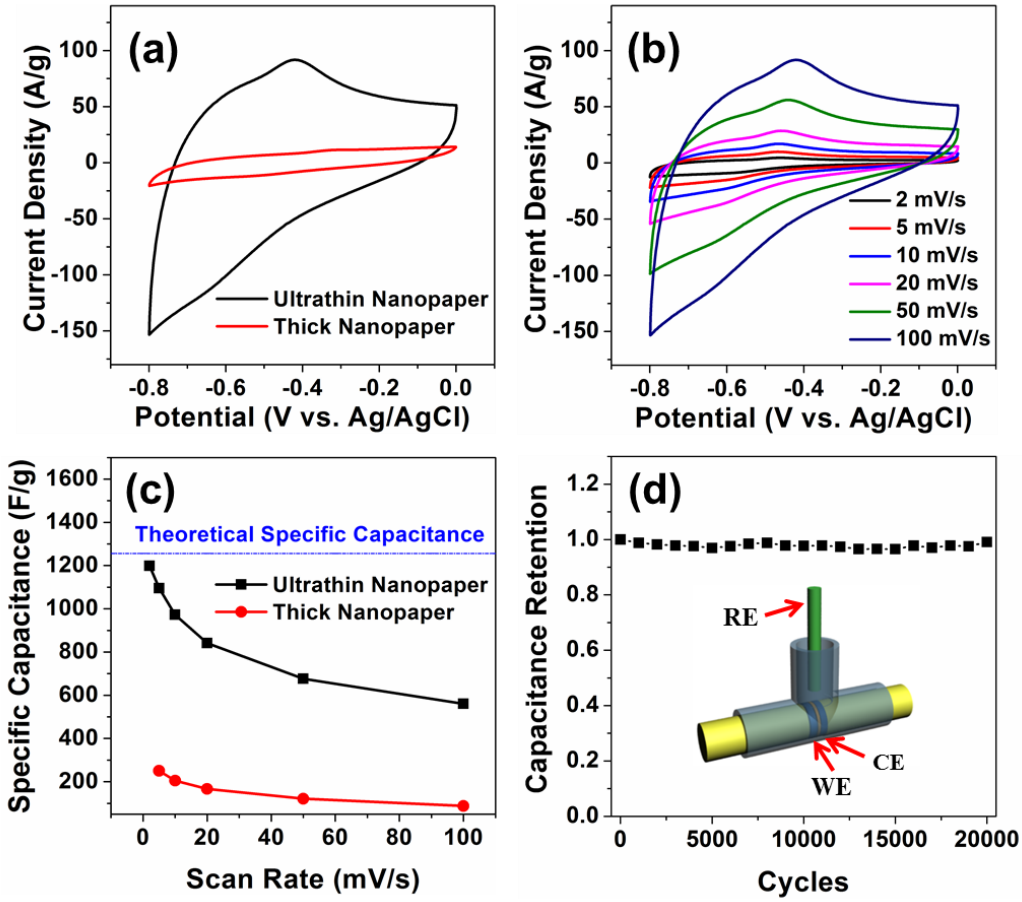

Figure 2.9 (a) CV curves of ultrathin (0.076 mg/cm^2) and thick (2.440 mg/cm^2) MoO$_3$ nanopaper electrode in a typical three-electrode configuration at 100 mV/s. (b) CV curves of ultrathin MoO$_3$ nanopaper at different scan rate. (c) Specific capacitance of ultrathin and thick MoO$_3$ nanopaper measured as a function of scan rate. (d) Cycle performance of ultrathin MoO$_3$ nanopaper electrode measured at 100mV/s for 20000 cycles. Insert is the schematic diagram of the test unit.

A symmetric device assembled with two MoO_3 nanopaper electrodes was evaluated in 5.0 M LiCl as electrolyte and PVA/LiCl gel electrolyte (Figure 2.10). CV curves of the device retains a quasi-rectangle shape when the scan rate increased from 5 mV/s to 1000 mV/s and GCD curves keep a triangular shape from 10 A/g to 100 A/g, demonstrating its good supercapacitor performance (Figure 2.10a). The specific capacitance of the entire device was calculated to be 257.6 F/g at scan rate of 5 mV/s, and it slowly decreases to 94.6 F/g when the scan rate increased to 200 mV/s (Figure 2.10b). The device also exhibits excellent cycling performance (Figure 2.10c). It retains 96.5 % of its initial capacitance after 20000 cycles, which is much better than the previous reported values.[10-13, 25, 32-39] The energy density of the symmetric device was calculated to be 22.89 Wh/kg at an average power density of 686.84 W/kg, which is about three times higher than carbon nanofiber supercapacitors, twenty times higher than H-TiO_2/MnO_2, K_yMoO_{3-x} and H_xMoO_y supercapacitors, and two hundred times higher than activated carbon cloth, TiN and H-ZnO/MnO_2 supercapacitors.[10, 27, 40-44] The average power density shows 10.1 kW/kg at an energy density of 8.4 Wh/kg, which is also higher than the values previously reported (Figure 2.10d).[10, 27] The high energy density and power density demonstrates its promising application for supercapacitors.

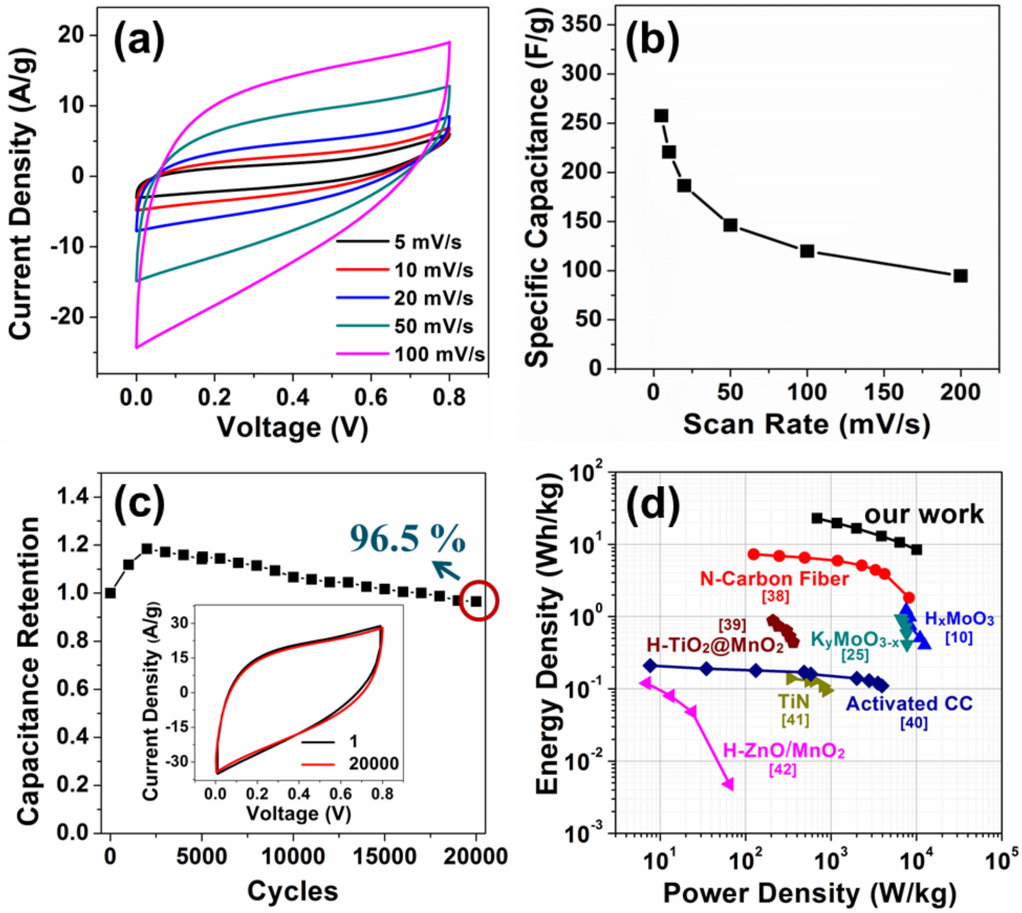

Figure 2.10 (a) CV curves of symmetric supercapacitor of ultrathin MoO_3 nanopaper electrodes from 5 to 100 mV/s (b) Specific capacitances and columbic efficiency of symmetric supercapacitor under different scan rate (c) Cycle performance of supercapacitor at 200 mV/s for 20000 cycles. Insert shows the CV curve almost unchanged after 20000 cycles. (d) Ragone plots of symmetric supercapacitor of ultrathin MoO_3 nanopaper electrodes. Reported values are also added for comparison.

2.4 Conclusions

In summary, we have successfully synthesized well-dispersive ultralong MoO_3 nanobelts *via* a modified hydrothermal reaction. The length of nanobelts can reach 200 μm. A versatile and effective method was used to fabricate transparent MoO_3 NB nanopapers. The transparent nanopapers show an excellent transmittance of 95.6 % and display an extraordinary flexibility and robustness over times of folding and unfolding. This ultrathin nanopaper electrode delivers an excellent specific capacitance of 1198 F/g at 2 mV/s and long-term cycle stability over 20000 cycles due to the efficient ion diffusion and reduced distance of electron transport. The MoO_3 NB nanopaper with outstanding flexibility, high transparency and excellent electrochemical performance holds great potential for the application of flexible electronics. Moreover, we believe that the same strategy can also be used to fabricate other metal oxide nanopaper electrodes for energy storage and other applications.

References

1. K. Nomura, H. Ohta, A. Takagi, T. Kamiya, M. Hirano, H. Hosono, *Nature* **2004**, *432*, 488-492.
2. H. Zhu, Z. Fang, C. Preston, Y. Li, L. Hu, *Energy Environ. Sci.* **2014**, *7*, 269-287.
3. L. Hu, G. Zheng, J. Yao, N. Liu, B. Weil, M. Eskilsson, E. Karabulut, Z. Ruan, S. Fan, J. T. Bloking, M. D. McGehee, L. Wagberg, Y. Cui, *Energy Environ. Sci.* **2013**, *6*, 513-518.
4. T. Sekitani, H. Nakajima, H. Maeda, T. Fukushima, T. Aida, K. Hata, T. Someya, *Nat. Mater.* **2009**, *8*, 494-499.
5. P. Yang, P. Sun, Z. Chai, L. Huang, X. Cai, S. Tan, J. Song, W. Mai, *Angew. Chem. Int. Ed.* **2014**, *53*, 11935-11939.

6. J. Zhong, H. Zhu, Q. Zhong, J. Dai, W. Li, S. H. Jang, Y. Yao, D. Henderson, Q. Hu, L. Hu, J. Zhou, *ACS Nano* **2015**, *9*, 7399-7406.
7. Y. Yang, S. Jeong, L. Hu, H. Wu, S. W. Lee, Y. Cui, *Proc. Natl. Acad. Sci. U.S.A.* **2011**, *108*, 13013-13018.
8. N. Li, G. Yang, Y. Sun, H. Song, H. Cui, G. Yang, C. Wang, *Nano Lett.* **2015**, *15*, 3195-3203.
9. Y. Dong, X. Xu, S. Li, C. Han, K. Zhao, L. Zhang, C. Niu, Z. Huang, L. Mai, *Nano Energy* **2015**, *15*, 145-152.
10. L. Huang, X. Gao, Q. Dong, Z. Hu, X. Xiao, T. Li, Y. Cheng, B. Yao, J. Wan, D. Ding, Z. Ling, J. Qiu, J. Zhou, *J. Mater. Chem. A* **2015**, *3*, 17217-17223.
11. L. Q. Mai, B. Hu, W. Chen, Y. Y. Qi, C. S. Lao, R. S. Yang, Y. Dai, Z. L. Wang, *Adv. Mater.* **2007**, *19*, 3712-3716.
12. K. Zhou, W. Zhou, X. Liu, Y. Sang, S. Ji, W. Li, J. Lu, L. Li, W. Niu, H. Liu, S. Chen, *Nano Energy* **2015**, *12*, 510-520.
13. X. Xiao, Z. Peng, C. Chen, C. Zhang, M. Beidaghi, Z. Yang, N. Wu, Y. Huang, L. Miao, Y. Gogotsi, J. Zhou, *Nano Energy* **2014**, *9*, 355-363.
14. Y. L. Ding, Y. Wen, C. Wu, P. A. van Aken, J. Maier, Y. Yu, *Nano Lett.* **2015**, *15*, 1388-1394.
15. Y. Sun, J. Wang, B. Zhao, R. Cai, R. Ran, Z. Shao, *J. Mater. Chem. A* **2013**, *1*, 4736-4746.

16. S.-H. Lee, Y.-H. Kim, R. Deshpande, P. A. Parilla, E. Whitney, D. T. Gillaspie, K. M. Jones, A. H. Mahan, S. Zhang, A. C. Dillon, *Adv. Mater.* **2008**, *20*, 3627-3632.

17. W. Tang, L. Liu, S. Tian, L. Li, Y. Yue, Y. Wu, K. Zhu, *Chem. Commun.* **2011**, *47*, 10058-10060.

18. L. Zheng, Y. Xu, D. Jin, Y. Xie, *J. Mater. Chem.* **2010**, *20*, 7135-7143.

19. P. Meduri, E. Clark, J. H. Kim, E. Dayalan, G. U. Sumanasekera, M. K. Sunkara, *Nano Lett.* **2012**, *12*, 1784-1788.

20. S. Hu, X. Wang, *J. Am. Chem. Soc.* **2008**, *130*, 8126-8127.

21. Z. Wang, S. Madhavi, X. W. Lou, *J. Phys. Chem. C* **2012**, *116*, 12508-12513.

22. B. Hu, L. Mai, W. Chen, F. Yang, *ACS Nano* **2009**, *3*, 478-482.

23. B. Mendoza-Sánchez, T. Brousse, C. Ramirez-Castro, V. Nicolosi, P. S. Grant, *Electrochim. Acta* **2013**, *91*, 253-260.

24. L. Zhou, L. Yang, P. Yuan, J. Zou, Y. Wu, C. Yu, *J. Phys. Chem. C* **2010**, *114*, 21868-21872.

25. T. Brezesinski, J. Wang, S. H. Tolbert, B. Dunn, *Nat. Mater.* **2010**, *9*, 146-151.

26. X.-L. Li, J.-F. Liu, Y.-D. Li, *Appl Phys Lett* **2002**, *81*, 4832-4834.

27. X. Xiao, C. Zhang, S. Lin, L. Huang, Z. Hu, Y. Cheng, T. Li, W. Qiao, D. Long, Y. Huang, L. Mai, Y. Gogotsi, J. Zhou, *Energy Storage Mater.* **2015**, *1*, 1-8.

28. X. W. Lou, H. C. Zeng, *Chem. Mater.* **2002**, *14*, 4781-4789.

29. W. Tang, L. Liu, Y. Zhu, H. Sun, Y. Wu, K. Zhu, *Energy Environ. Sci.* **2012**, *5*, 6909-6913.

30. B. Yao, L. Yuan, X. Xiao, J. Zhang, Y. Qi, J. Zhou, J. Zhou, B. Hu, W. Chen, *Nano Energy* **2013**, *2*, 1071-1078.

31. L. Yuan, B. Yao, B. Hu, K. Huo, W. Chen, J. Zhou, *Energy Environ. Sci.* **2013**, *6*, 470-476.

32. L. Mai, X. Tian, X. Xu, L. Chang, L. Xu, *Chem. Rev.* **2014**, *114*, 11828-11862.

33. J. Chang, M. Jin, F. Yao, T. H. Kim, V. T. Le, H. Yue, F. Gunes, B. Li, A. Ghosh, S. Xie, Y. H. Lee, *Adv Funct Mater* **2013**, *23*, 5074-5083.

34. X. Cao, B. Zheng, W. Shi, J. Yang, Z. Fan, Z. Luo, X. Rui, B. Chen, Q. Yan, H. Zhang, *Adv. Mater.* **2015**, *27*, 4695-4701.

35. G. R. Li, Z. L. Wang, F. L. Zheng, Y. N. Ou, Y. X. Tong, *J. Mater. Chem.* **2011**, *21*, 4217-4221.

36. Y. Liu, B. Zhang, Y. Yang, Z. Chang, Z. Wen, Y. Wu, *J. Mater. Chem. A* **2013**, *1*, 13582-13587.

37. F. Jiang, W. Li, R. Zou, Q. Liu, K. Xu, L. An, J. Hu, *Nano Energy* **2014**, *7*, 72-79.

38. V. Kumar, X. Wang, P. S. Lee, *Nanoscale* **2015**, *7*, 11777-11786.

39. J. Rajeswari, P. S. Kishore, B. Viswanathan, T. K. Varadarajan, *Electrochem. Commun.* **2009**, *11*, 572-575.

40. Y. Cheng, L. Huang, X. Xiao, B. Yao, L. Yuan, T. Li, Z. Hu, B. Wang, J. Wan, J. Zhou, *Nano Energy* **2015**, *15*, 66-74.

41. X. Lu, M. Yu, G. Wang, T. Zhai, S. Xie, Y. Ling, Y. Tong, Y. Li, *Adv. Mater.* **2012**, *25*, 267-272.

42. G. Wang, H. Wang, X. Lu, Y. Ling, M. Yu, T. Zhai, Y. Tong, Y. Li, *Adv. Mater.* **2014**, *26*, 2676-2682.

43. X. Lu, G. Wang, T. Zhai, M. Yu, S. Xie, Y. Ling, C. Liang, Y. Tong, Y. Li, *Nano Lett.* **2012**, *12*, 5376-5381.

44. P. Yang, X. Xiao, Y. Li, Y. Ding, P. Qiang, X. Tan, W. Mai, Z. Lin, W. Wu, T. Li, H. Jin, P. Liu, J. Zhou, C. P. Wong, Z. L. Wang, *ACS Nano* **2013**, *7*, 2617-2626.

Chapter 3

TiN Nanopapers for Ultrafast-Charging Supercapacitors

Abstract

Ultrafast charging energy storage devices are attractive for powering personal electronics and electric vehicles. Most ultrafast charging devices are made of carbonaceous materials such as chemically converted graphene and carbon nanotubes. Yet, their relatively low electrical conductivity may restrict their performance at ultrahigh charging rate. Here, we report the fabrication of a porous TiN paper as an alternative electrode material for ultrafast charging devices. The TiN paper shows an excellent conductivity of 3.67×10^4 S m^{-1}, which is considerably higher than most carbon-based electrodes. The paper-like structure also contains a combination of large pores between interconnected nanobelts and mesopores within the nanobelts. This unique electrode enables fast charging by simultaneously providing efficient ion diffusion and electron transport. The supercapacitors (SCs) made of TiN paper enable charging/discharging at an ultrahigh scan rate of 100 V s^{-1} in a wide voltage window of 1.5 V in Na_2SO_4 neutral electrolyte. It has an outstanding response time with a characteristic time constant of 4.0 ms. Significantly, the TiN paper-based SCs also show zero capacitance loss after 200,000 cycles, which is much better than the stability performance reported for other metal nitride SCs. Furthermore, the device shows great promise in scalability. The filtration method enables good control of the thickness and mass loading of TiN electrodes and devices. When the mass loading of

TiN increases from 0.38 to 3.00 mg cm^{-2}, the device's areal capacitance increases linearly while the gravimetric and volumetric capacitance remain almost unchanged.

3.1 Introduction

The emerging advances in portable and wearable electronics urge the rapid development of fast charging and discharging energy storage devices.[1-6] Supercapacitors (SCs), renowned for their high charging rate and long lifespan, have received great attention in the past decades.[7-8] Currently, most SCs are operated at a charging speed of 2 mV s^{-1} to 100 mV s^{-1}, which corresponding to the charging time from tens of seconds to tens of minutes.[9-10] Further increasing the charging speed usually results in an inferior performance and deteriorated material structure.[11] Ultrafast-charging SCs with charging rate >10 V s^{-1} would significantly shorten the charging time and meet the requirements for high-rate energy storage devices.[12-14] Ultrafast-charging SCs are mainly fabricated by carbonaceous materials, such as activated carbon, graphene and CNTs.[15-18] Yet, the relatively low electrical conductivity of activated carbon (~1-100 S m^{-1}), chemically converted graphene (~500-2000 S m^{-1}) and carbon nanotubes (~1×10^4 S m^{-1}) restricts their performances at ultrahigh charging rates.[19-20] Therefore, exploration of new materials with superior conductivity for ultrafast-charging SCs is highly desirable.

Transition metal nitrides have received increasing attention for energy storage devices due to their excellent electrical conductivity and high capacities/capacitances.[21-22] Among them, titanium nitride (TiN) stands out as one of the most promising material for SCs because of its outstanding conductivity (4.0×10^5~5.6×10^6 S m^{-1}) and mechanical stability.[22-23] However, in most cases, TiN nanostructures were supported on a substrate, which limits the gravimetric capacitances of TiN electrodes when it is normalized with the mass of entire electrode. Besides, most TiN-based electrodes suffered from severe capacitance loss in aqueous electrolytes, especially in the acidic and alkaline medium.[24-25] Hasegawa *et al.* showed that the neutral electrolyte can help to alleviate the cycling stability of transition metal nitrides.[25] Here we report the fabrication of a freestanding, flexible and porous TiN paper electrode for ultrafast charging SCs. Electrical measurements showed that a single TiN nanobelt and a piece of TiN paper achieved excellent conductivities of 4.5×10^5 S m^{-1} and 3.7×10^4 S m^{-1}, respectively. The unique combination of high conductivity and pore structure of the TiN paper warrants rapid electron transport and ion diffusion that are required for ultrafast charging. The SCs fabricated with TiN paper electrodes enable an ultrahigh charging/discharging rate of 100 V s^{-1} in a wide voltage window of 1.5 V in neutral Na_2SO_4 aqueous electrolyte. The SC device also shows remarkable stability with zero loss of capacitance after testing for 200,000 cycles, which is uncommon for metal nitride materials.

3.2 Experimental Section

Synthesis of ultralong TiO_2 nanobelts

0.100 g P25 powder was mixed with 20.0 mL 10.0 mol/L NaOH aqueous solution. The mixture was transferred to a Teflon-lined autoclave and heated at

200 °C for 48 h. The autoclave was cooled down at room temperature. The solid product, sodium titanate ($Na_2Ti_3O_7$) nanobelts, in the solution was collected by vacuum filtration and washed with deionized water. The sodium titanate was then re-dispersed into 0.10 mol/L HCl aqueous solution and let it stay for 24 h to form hydrogen titanate ($H_2Ti_3O_7$) nanobelts through ion exchange reaction. Finally, TiO_2 nanobelts were obtained by annealing the $H_2Ti_3O_7$ nanobelts at 500 °C in air for 1 h.

Preparation of TiO_2 and TiN paper

TiO_2 and TiN paper were prepared by vacuum filtration of the ultralong $H_2Ti_3O_7$ nanobelts followed by annealing process. First, the $H_2Ti_3O_7$ nanobelts were re-dispersed into 100 mL deionized water and stirred for 0.5 h to make a uniform suspension. Then the $H_2Ti_3O_7$ nanobelt suspension solution was poured into the vacuum filtration system and get a $H_2Ti_3O_7$ paper. The $H_2Ti_3O_7$ paper with the filter paper was put in an electric oven at 70 °C for 20 min until they get dry. The $H_2Ti_3O_7$ paper can be easily peeled off from the filter paper afterward. The papers with different mass loadings can be readily tuned by changing the mass of $H_2Ti_3O_7$ nanobelts in the suspension solution for the filtration.

TiO_2 paper were obtained by annealing the $H_2Ti_3O_7$ paper at 500 °C in air for 1 h. TiN papers were obtained by annealing the TiO_2 paper in ammonia environment at 800 °C for 1 h. The conventional TiN pellet electrodes as a control sample were fabricated by mixing the TiN nanobelts, carbon black and PTFE in a ratio of 8:1:1 followed by rolling the mixture into thin films.

Materials Characterization

The X-ray diffraction patterns were collected on a powder X-ray diffractometer (Rigaku Americas Miniflex Plus) with 2θ angle from 30 to 70° under a step size of 0.01° at a rate of 1°/min. The morphology of nanobelts was investigated by a field emission SEM (FEI Quanta 3D FEG dual beam) and TEM (JEM, 2010-HR). XPS (ESCALAB 250) was used to analyze the chemical composition of samples. Textural properties were examined by Brunauer-Emmett-Teller and Barrett-Joyner-Halenda methods using an ASAP 2020 surface area analyzer (Micromeritics Instrument) via nitrogen porosimetry. The areal mass of the electrodes was measured based on 4 cm^2 TiN papers on an analytical balance (Citizen CX265) with a resolution of 0.01 mg. The thickness of the electrodes was measured using a micrometer caliper (NSCING) with a resolution of 0.001 mm. The single TiO_2 and TiN nanobelt devices were fabricated via a focused ion beam (FIB, Quanta 3D FEG) with Pt as the contact electrode. The electrical measurement was carried out using an Agilent 2400 instrument.

The electrochemical measurements were conducted using electrochemical workstation (CHI 660D and EC-Lab SP-300). For three-electrode measurements, a piece of 0.2 cm^2 TiN paper was used as working electrode. Ag/AgCl (CHI, USA) and YP-50 activated carbon (Kuraray Chemical, Japan) was used as the reference electrode and counter electrode, respectively. The measurements were carried out in different aqueous electrolytes, including 0.5 M Na_2SO_4 (pH = 7.67), 3 M LiCl (pH=6.76), 1 M H_2SO_4 (pH = 0.03) and 1 M KOH (pH = 13.65) solutions. A piece of Celgard film was used as a separator (Celgard, USA). Two-electrode symmetric devices were assembled with two pieces of 0.2 cm^2 TiN paper or pellet with the same area and mass loading. Three samples with similar mass loadings were tested for each condition to make sure the electrode's capacitive performance is reproducible. Unless otherwise mentioned, the mass loading of the TiN papers in the SSC is 1.50 mg cm^{-2}.

Calculation

Gravimetric capacitance is calculated from CV curves using the following equation.

$$C_g = \frac{\int I\,dV}{v\Delta V m}$$

where I is the current (A), V is the working potential, v is the scan rate (V s^{-1}), ΔV is the working voltage, m is the mass loading (g). $\int I\,dV$ corresponds to the area of the discharging parts. For the working potential in the positive region, it corresponds the area in the reductive part. For the working potential in the negative region, it corresponds to the area in the oxidation part.

Areal capacitance is calculated from CV curves using the following equation.

$$C_A = \frac{\int I\,dV}{v\Delta V A}$$

where I is the current (A), V is the working potential, v is the scan rate (V s^{-1}), ΔV is the working voltage, A is the working area (cm^2). $\int I\,dV$ corresponds to the area of the discharging parts.

The characteristic time constant ($\tau_{characteristic}$) is calculated by the following equation:

$$\tau_{characteristic} = \frac{1}{2\pi f_{characteristic}}$$

where the $f_{characteristic}$ is the frequency (Hz) at a phase degree of -45° from the EIS measurement.

Imaginary capacitances (C”) were calculated by the following equation:

$$C^{"} = \frac{Z'}{2\pi f|Z|^2}$$

where Z' (Ω) is the real part of Z, Z is the electrochemical impedance (Ω), f is the frequency (Hz) from the EIS measurement.

3.3 Results and Discussions

Ultralong TiO_2 nanobelts were prepared by a hydrothermal method. TiO_2 nanobelts have average length around tens of micrometers, width of 50-200 nm and thickness of 20-50 nm (Figure 3.1). These nanobelts with large aspect ratio can be easily assembled into flexible, paper-like electrodes using filtration method (Figure 3.2).[26] X-ray diffraction (XRD) pattern confirmed that the nanobelts are monoclinic TiO_2 (TiO_2-B, JCPDS No. 74-1940).

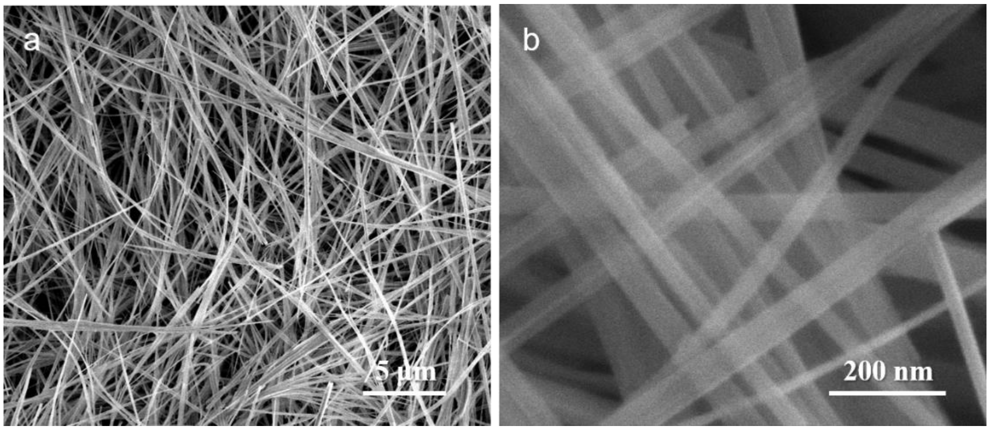

Figure 3.1 SEM images of TiO_2 paper.

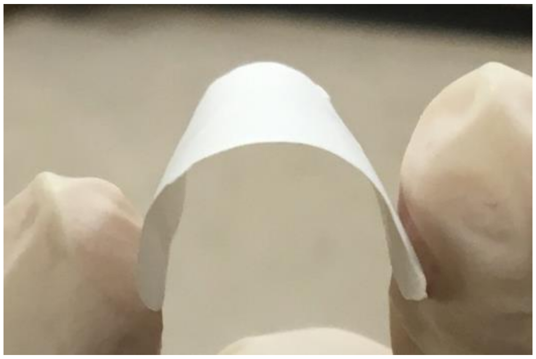

Figure 3.2. Optical image of a piece of flexible TiO_2 paper.

TiN paper was obtained by treating the TiO_2 paper in ammonia atmosphere at 800 °C (Figure 3.3a). Notably, TiN paper inherits the excellent flexibility of TiO_2 paper (Figure 3.3b inset). While the basic framework of the 3D nanobelts assembly did not change upon ammonia treatment, each nanobelt became porous structure (Figure 3.3b and 3.3c). N_2 adsorption-desorption isotherms showed that the specific surface area increased from 31.2 m^2/g (TiO_2 paper) to 43.5 m^2/g (TiN paper) after ammonia treatment (Figure 3.4a). The hysteresis located at $0.4 < P/P_0 < 1.0$ indicates the presence of mesopores.[27] The pore size distribution profile also confirmed the presence of higher amount of mesopores for TiN paper (Figure 3.4b). The porous structure was further confirmed with the transmission electron microscopy (TEM) image (Figure 3.3d). It has been reported that TiO_2 can be etched by ammonia at high temperatures.[21-22] The topotactic reaction of TiO_2 nanobelts and NH_3 led to the rearrangement of the oxide structure and produced a mesoporous structure in the framework of the TiN nanobelts.[28-29] The high-resolution TEM image revealed the

TiN nanobelt has a lattice fringe of 0.245 nm, which is consistent with the *d*-spacing of (111) crystal plane of cubic TiN (Figure 3.3e). The cross-sectional SEM image clearly showed that the TiN paper is formed *via* uniform assembly of nanobelts (Figure 3.3f). The filtration method allows good control of the TiN paper thickness. The large pores between the nanobelts and mesoporous structure of the nanobelts provide sufficient space for ion diffusion, which is critical for the fast charging.

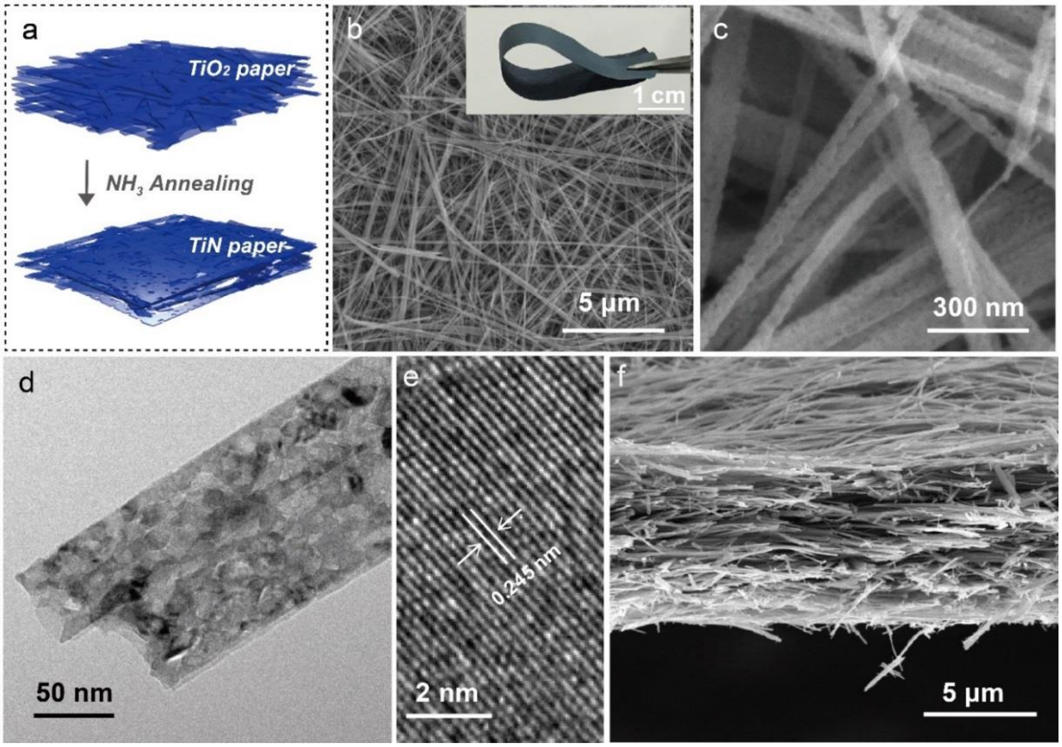

Figure 3.3 (a) Schematic illustration of the fabrication process of TiN paper from TiO_2 paper. (b, c) Scanning electron microscopy (SEM) images of TiN nanobelts. Inset in Figure 1b shows the digital image of a piece of flexible TiN paper. (d, e) TEM and high-resolution TEM images of porous TiN nanobelts. (f) Cross-sectional SEM image of TiN paper.

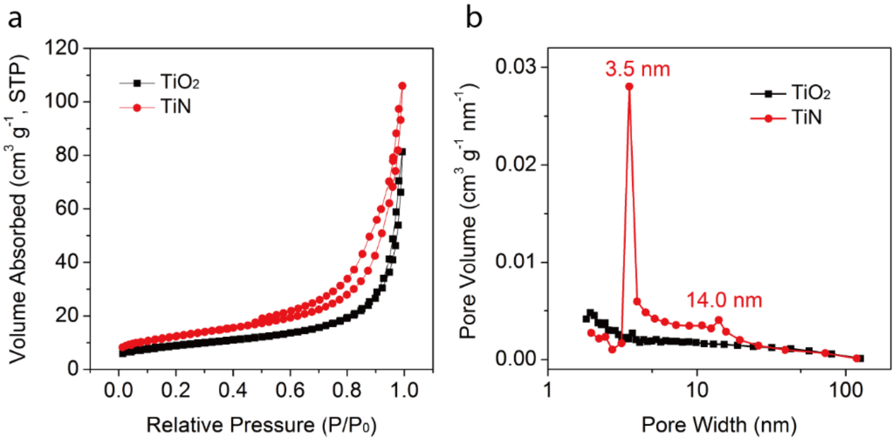

Figure 3.4 (a) N_2 adsorption/desorption isotherms of TiO_2 nanobelts and TiN nanobelts. (b) Pore size distribution of TiO_2 nanobelts and TiN nanobelts.

Additional X-ray diffraction and spectroscopy techniques were used to probe the chemical composition of the TiN paper. Despite XRD pattern showed that the sample is cubic phase TiN (JCPDS No. 38-1420) (Figure 3.5a), X-ray photoelectron spectroscopy (XPS) survey spectrum revealed the existence of Ti, N, and O on the surface of TiN nanobelts. The O signal is believed to be due to TiO_2 and/or TiO_xN_y, which might come from the incomplete conversion from their oxide predecessor and surface oxidation after exposure in air.[25, 30] The possible reaction between TiO_2 and NH_3 are: First, the ammonia is decomposed into nitrogen and hydrogen ($2NH_3 + heat \rightarrow N_2 + 3H_2$). The reaction proceeds with the reduction of TiO_2 to TiO by hydrogen ($TiO_2 + H_2 \rightarrow TiO + H_2O$). Then, TiO reacts with ammonia and generate TiN ($TiO + NH_3 \rightarrow TiN + H_2O$).[31] The TiO_2 also reacts with nitrogen and generate TiO_xN_y ($TiO_2 + N_2 \rightarrow TiO_xN_y + O_2$).[32]

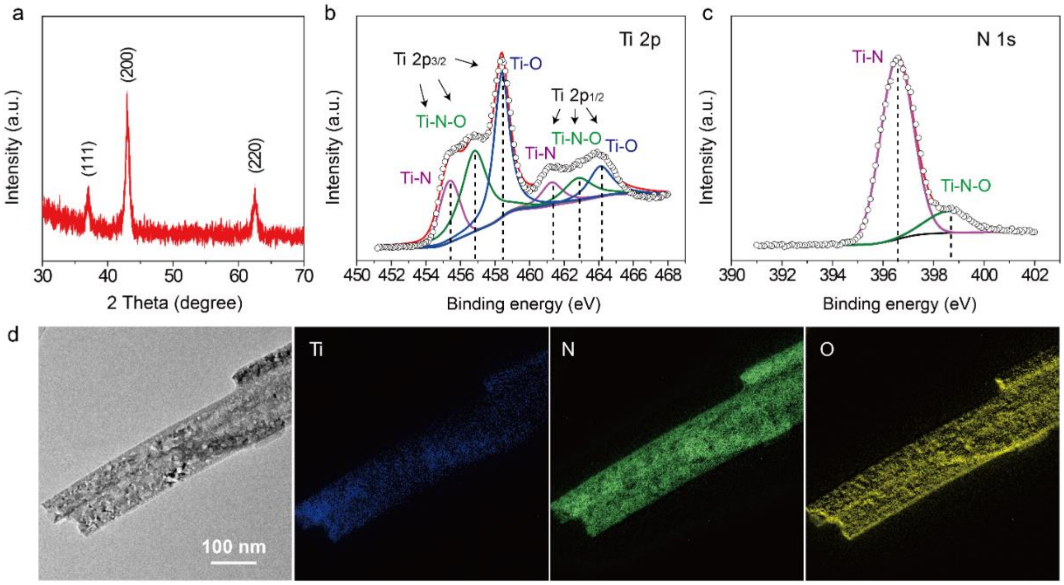

Figure 3.5 (a) XRD pattern and (b, c) Ti 2p and N 1s XPS spectra of TiN paper. (d) TEM image and the corresponding Ti, N and O elemental mapping images of TiN nanobelts.

The core-level Ti 2p XPS spectrum exhibits multiple peaks in the binding energy range between 453 and 466 eV. They can be deconvoluted into three sets of synthetic peaks, corresponding to Ti-N ($2p_{3/2}$=455.4 eV, $2p_{1/2}$=461.3 eV), Ti-N-O ($2p_{3/2}$=456.85 eV, $2p_{1/2}$=462.9 eV) and Ti-O ($2p_{3/2}$=458.4 eV, $2p_{1/2}$=464.15 eV) (Figure 3.5b).[33] The N 1s spectrum also consists of two different peaks, Ti-N (396.6 eV) and Ti-N-O (398.6 eV), which are consistent with the peaks observed in the Ti 2p spectrum (Figure 3.5c).[34] Furthermore, TEM elemental mapping results confirmed the uniform distribution of Ti, N, and O in TiN nanobelts (Figure 3.5d).

To probe the electrical conductivity of TiO_2 and TiN, focused ion beam (FIB) lithography was used to fabricate single-nanobelt devices (Figure 3.6a inset). The current-voltage (*I*-*V*) curves of the TiO_2 and TiN nanobelt devices are shown in

Figure 3.6a. TiN exhibits a significantly larger current response with voltage than TiO_2. Their specific conductivities were calculated according to the following equations:

$$R = \rho \frac{l}{A} \qquad (1)$$

$$\sigma = \frac{1}{\rho} \qquad (2)$$

where *R* is the resistance, ρ is the resistivity, *l* is the length of the nanobelt, *A* is the cross-sectional area of the nanobelt, and σ is the conductivity of the nanobelt. The conductivity of a single TiN nanobelt (4.5×10^5 S m^{-1}) is almost 3 orders of magnitude higher than that of TiO_2 nanobelt (4.9×10^2 S m^{-1}). The TiN paper also retains excellent conductivity of 3.7×10^4 S m^{-1}. These values are much higher than the previous reported carbon-based materials, such as activated carbon (10-100 S m^{-1})[35], chemical converted graphene (5.0×10^2 S m^{-1}),[20] holy graphene (~10^3 S m^{-1})[36], laser-scribed graphene (1738 S m^{-1}) and even higher than the commercial CNT (~10^4 S m^{-1})[37].

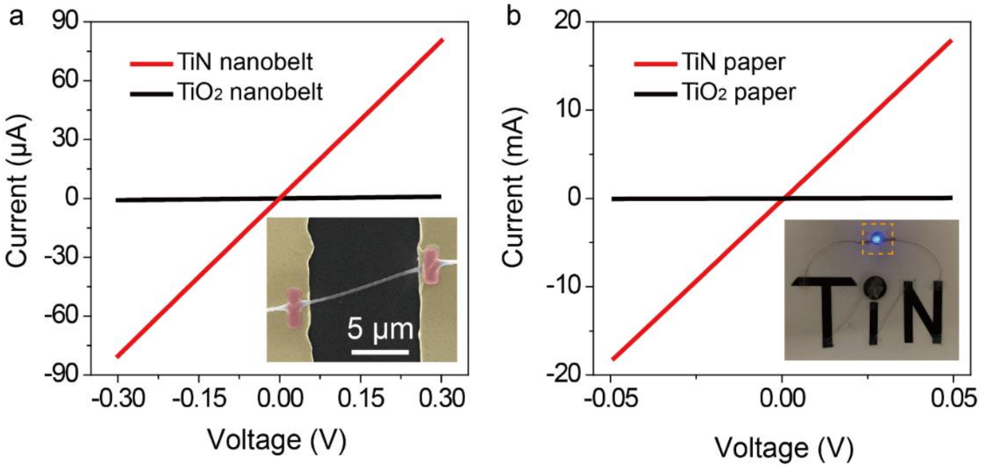

Figure 3.6 (a) I-V curves of individual ultralong TiO_2 and TiN nanobelts. Inset shows the SEM image of a single nanobelt test unit. (b) I-V curves of TiO_2 and TiN papers. Inset shows the digital image of TiN papers as a part of the electrical connections to light a blue LED by a commercial 3V battery.

Furthermore, the TiN paper has a low sheet resistance of only 2.7 Ω sq^{-1}, which is smaller than those of graphene film (280.0 Ω sq^{-1}),[38] chemical converted graphene film (124.0 Ω sq^{-1}),[39] CNT paper (10.0 Ω sq^{-1}),[40] Au paper (7.0 Ω sq^{-1}),[41] MoO_{3-x} paper (5.1 Ω sq^{-1}),[37] Polypyrrole paper (4.5 Ω sq^{-1}),[9] and comparable to that for poly(3,4-ethlenedioxythirphene):polystyrene sulfonate (PEDOT:PSS) paper (2.6 Ω sq^{-1})[42] (Figure 3.6b). Given the excellent conductivity, the TiN paper can actually be used as a connecting lead to power a 2.5 V light-emitting-diode (LED) with a commercial 3 V button battery (Figure 3.6b inset).

The unique combination of high conductive and pore structure makes TiN paper an excellent electrode candidate for ultra-fast charging supercapacitors. The working potential of TiN papers was first evaluated using a three-electrode system in electrolytes with different pH values. TiN paper electrodes exhibit the largest working potential window (1.5 V) in 0.5 M Na_2SO_4 (pH=7.57) neutral electrolyte, while only 0.8 V in 1.0 M KOH (pH=13.65), 1.0 V in 1.0 M H_2SO_4 (pH=0.03) and 0.9 V in 3.0 M LiCl (pH=6.76) (Figure 3.7). Significantly, this is the first report for TiN-based materials to be operated in such a wide working voltage of 1.5 V.[22, 33, 43-46] The large working voltage can be ascribed to the employment of the sulfate-based neutral electrolyte, which have been demonstrated to be effective in expanding the working voltage of SC materials in aqueous electrolyte because the high solvation energy of sulfate and alkali metal ions (160-220 kJ mol^{-1}) cause relatively large overpotentials for hydrogen evolution and oxygen evolution reactions.[47-50]

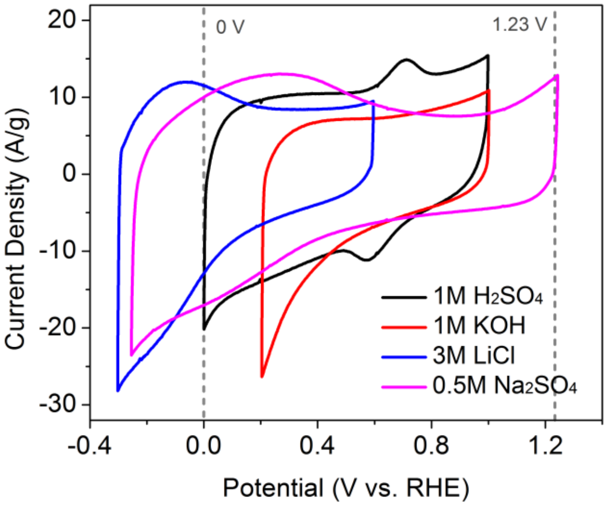

Figure 3.7 CV curves of TiN paper electrodes obtained in electrolytes (1.0 M H_2SO_4, 1.0 M KOH, 3.0 M LiCl and 0.5 M Na_2SO_4) with different pH values.

Excellent specific capacitances have been obtained for electrodes with small mass loading (0.1-1 mg cm^{-2}) of metal nitrides deposited on conducting substrates (~10-200 mg cm^{-2}).[21-22, 24, 33, 51] These capacitances were typically calculated based only on the mass of active material. However, the value of specific capacitance would be more practically meaningful if it is normalized to the mass of the entire electrode. In this regard, binder-free and conducting additive-free TiN papers is advantageous over its counterparts that require current collector. The TiN paper electrode showed a high capacitance of 164.5 F g^{-1} in 0.5 M Na_2SO_4 at a scan rate of 5 mV s^{-1} and retained 64.7 % of its capacitance when the scan rate is raised to 100 mV s^{-1}, which is significantly higher than capacitance of other metal nitride electrodes normalized to the mass of entire electrode, such as TiN nanosheets/graphene nanosheets (5.3 F g^{-1} at

10 mV s^{-1}),[21] Nb_4N_5/Ni foil (0.86 F g^{-1} at 0.67 A g^{-1}),[52] TiN nanowire/carbon cloth (10.2 F g^{-1} at 10 mV s^{-1}),[22] VN nanowire/carbon cloth (16.7 F g^{-1} at 10 mV s^{-1}),[53] and TiN/MnO_2 nanowire/carbon cloth (25.9 F g^{-1} at 2 mA cm^{-2})[54].

TiN pellet electrodes as control samples were prepared by mixing TiN nanobelts, carbon black and PTFE binders, followed by pressing the mixture into thin pellets (Figure 3.8). Symmetric supercapacitors (SSCs) were prepared via the assembly of two TiN paper or pellet electrodes with the same mass loadings. As shown in Figure 3.8b, the paper-based SSCs indeed have considerably longer charging and discharging time than the pellet SSCs. Importantly, the paper SSC exhibits excellent capacitive behavior even at ultrafast charging rates at 200 A g^{-1}, while the charging rate of the pellet SSC is limited by its large internal resistances. As shown in the Figure 3.9, the specific capacitance of the TiN paper-based SSC was 12.67 F/g at a scan rate of 100 mV/s and retained a capacitance of 8.99 F/g at a high scan rate of 1 V/s and 3.35 F/g at an ultrahigh scan rate of 100 V/s. However, the specific capacitance of the TiN pellet-based SSC was only 2.91 F/g at a scan rate of 100 mV/s and retained a capacitance of 1.24 F/g at a high scan rate of 1 V/s and 0.11 F/g at an ultrahigh scan rate of 100 V/s. The reduced capacitance and rate capability of the pellet electrode are mainly because of two reasons. First, the addition of non-conductive and non-electrochemical active polymer binder (PTFE) increases the overall electrode resistance and decreases the specific capacitance. Second, part of the active capacitive material TiN nanobelts are covered by carbon black and PTFE. This makes the ion diffusion to TiN nanobelts more difficult, especially at high charging rates, compared to the porous paper electrode.

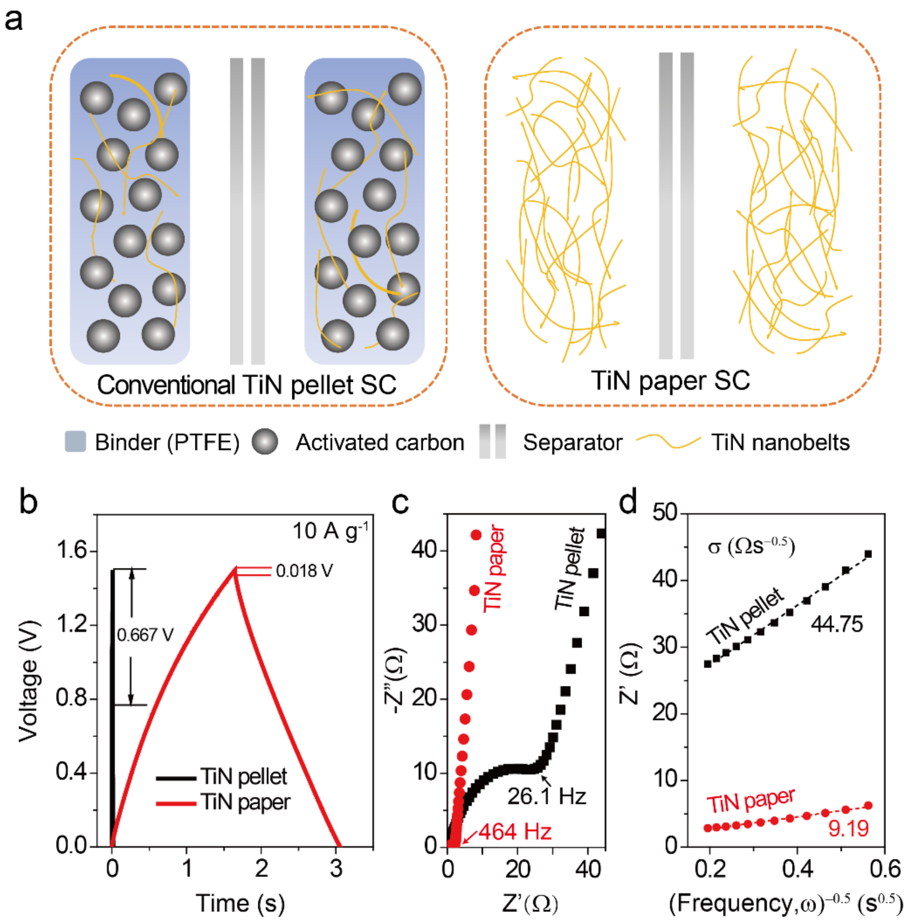

Figure 3.8 (a) Schematic illustration of the device configuration of TiN pellet and paper based SSCs. (b) Galvanostatic charging and discharging curves of the SSCs at a current density of 10 A g^{-1}. The iR drop of TiN paper SSC and pellet SSC are 0.018 V and 0.667 V, respectively. (c) Electrochemical impedance spectra of TiN pellet SSC and TiN paper SSC. The knee frequency of the TiN paper SSCs and TiN pellet SSCs are 464.0 Hz and 26.1 Hz, respectively. (d) Z' versus the reciprocal of the square root of frequency ($\omega^{-0.5}$) in the intermediate frequency range. The dashed lines are the linear fitting lines for calculating the ion diffusion resistance, σ.

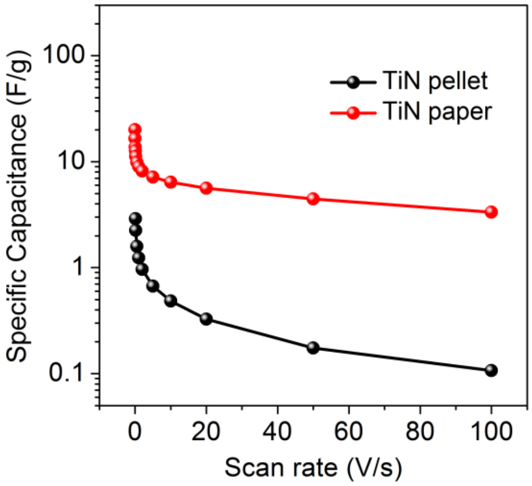

Figure 3.9 Plots of specific capacitance of TiN pellet SSC and TiN paper SSC as a function of scan rate.

Electrochemical impedance spectroscopy (EIS) measurements were performed to understand the electron transport, ion diffusion resistivity and frequency characteristics of TiN SSCs. The equivalent series resistance (ESR) obtained from the intercept of the plot on the real axis is only 0.92 Ω, indicating the excellent electrical conductivity and low resistance of TiN paper SSCs. Besides, the paper SSC showed much smaller charge transfer resistance (1.66 Ω) than the pellet SSC (35.98 Ω) (Figure 3.8c). The high knee frequency of paper SSC (464.0 Hz) is also an order of magnitude higher than the knee frequency of the pellet SSC (26.1 Hz) (Figure 3.8c). The characteristic time constant of the paper SSC was calculated to be 4 ms (Figure 3.10). This value is substantially smaller than the values reported for many carbon based SSCs, including CNT fibers (1930 ms),[55] metal-organic frameworks derived porous carbon (1270 ms),[56] carbide-derived carbon (379 ms),[57] laser-scribed graphene (33 ms),[58] and onion-like carbon (26 ms)[59].

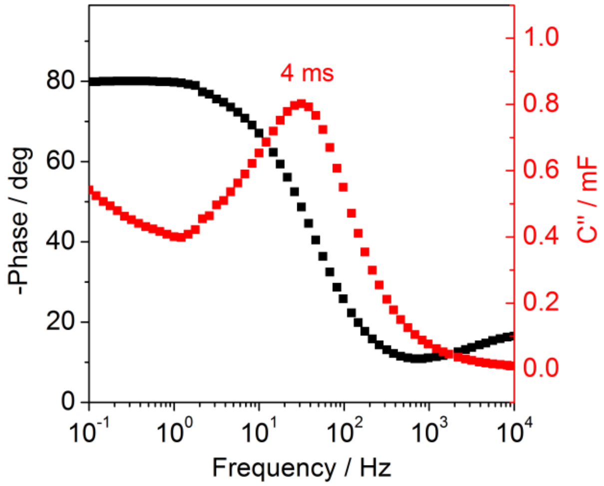

Figure 3.10 Bode phase plot and imaginary capacitance (C″) of TiN paper electrode obtained at different frequencies.

In addition to the efficient electron transport, paper SSCs exhibited much faster ion diffusion kinetics than the conventional pellet SSCs. The ion diffusion resistances (σ) can be extracted from the slopes of the linear fitting of the real part of impedance (Z') versus the reciprocal of the square root of frequency ($\omega^{-0.5}$) in the intermediate frequency range.[60] The paper SSC displayed an σ of 9.19 $\Omega\ s^{-0.5}$, which is much smaller than the pellet SSCs (44.75 $\Omega\ s^{-0.5}$), highlighting the advantage of having the unique porous electrode structure (Figure 3.8d).

The CV curves of the paper SSC retain the rectangular shape even at ultrafast charging rates of 100 V s^{-1} (Figure 3.11a-e). The linear increase of the discharge currents to 20 V s^{-1} reflects the efficient charge transfer and ion diffusion in the paper SSCs (Figure 3.11f), in contrast to the pellet SSCs. The paper SCC delivers an energy density of 1.05 Wh/kg under an extraordinarily high power density of 251.2 kW/kg, with a charging/discharging time of only 15 ms. These values are much better than most of previously reported electrochemical capacitors. Furthermore, the TiN paper SSCs showed remarkable energy density of 3.26 mWh/cm^3 under a power density of 78.3 mW/cm^3. An energy density of 0.54 mWh/cm^3 was still retained under an extremely high power density of 1.31×10^5 mW/cm^3, which is again much higher than most metal nitride-based SSCs.[21-22, 51, 53, 61-62]

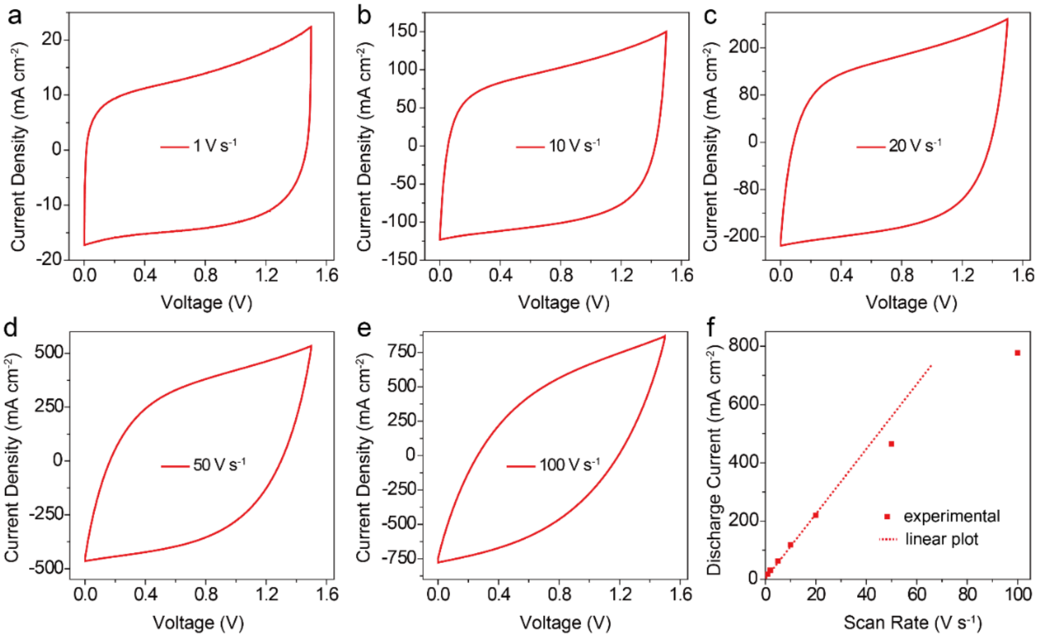

Figure 3.11 (a-e) CV curves of TiN paper SSC collected at different scan rates in 0.5 M Na_2SO_4 aqueous electrolyte. (f) A plot of discharge current of TiN paper SSC against scan rate.

Transition metal nitride electrodes have been suffering from the instability problem during cycling.[22, 24] TiN paper SSCs were tested for long-term stability in three different electrolytes, 0.5 M Na_2SO_4, 1.0 M H_2SO_4 and 1.0 M KOH solutions. TiN paper SSC show zero decay in capacitance after cycling in 0.5 M Na_2SO_4 electrolyte for 200,000 cycles at 1 V s^{-1}, while only 47.5 % and 42.4% of capacitance were retained in 1.0 M H_2SO_4 and 1.0 M KOH electrolyte, respectively (Figure 3.12a-d). SEM images revealed that the porous structure of TiN nanobelts remained unchanged after cycling in 0.5 M Na_2SO_4 electrolyte. In contrast, the nanobelt morphology of TiN changed significantly after testing in 1.0 M H_2SO_4 and 1.0 M KOH solutions (Figure 3.12e-g). XPS spectra were collected to investigate the chemical nature of TiN electrode surface before and after cycling stability test. The N 1s spectrum of TiN paper tested in 0.5 M Na_2SO_4 solution show no obvious change, while the N 1s peaks disappeared after cycling in 1.0 M H_2SO_4 or 1.0 M KOH electrolytes (Figure 3.13). Ti 2p XPS spectra further showed that the signal of Ti-N and Ti-N-O decreased considerably after testing in H_2SO_4 or KOH solution, leaving only Ti-O signals, while the Ti-N and Ti-N-O signals were not affected for TiN paper tested in in 0.5 M Na_2SO_4. These results suggested that TiN papers were oxidized in H_2SO_4 and KOH solution, which are consistent with the previous reports.[25, 63-64] The titanium ion in TiN was easily oxidized to soluble titanate ion ($HTiO_3^-$) and/or $TiO_2 \cdot H_2O$ in alkaline solution.[63] The titanium ion in TiN got oxidized steadily to the states of trivalence ($Ti(OH)^{2+}$) and tetravalence ($Ti(OH)_2^{2+}$) after working at positive voltages in acidic solutions.[64] These results demonstrate the importance of selecting the sulfate-based neutral electrolyte for TiN electrodes and possibly other nitride electrodes. The outstanding cycling stability of TiN with zero decay in capacitance after 200,000 cycles in 0.5 M Na_2SO_4 is much better than the previous reports on metal nitride electrodes, such as TiN nanowires on carbon cloth (82 % after 15,000 cycles),[22] Mo_2N nanobelts/graphene (85.7 % after 4000 cycles)[65], Nb_4N_5 nanobelts

(80 % after 1000 cycles),[51] VN/CNT composite (82 % after 10,000 cycles),[61] and Fe_2N/graphene (92.9 % after 20,000 cycles)[21].

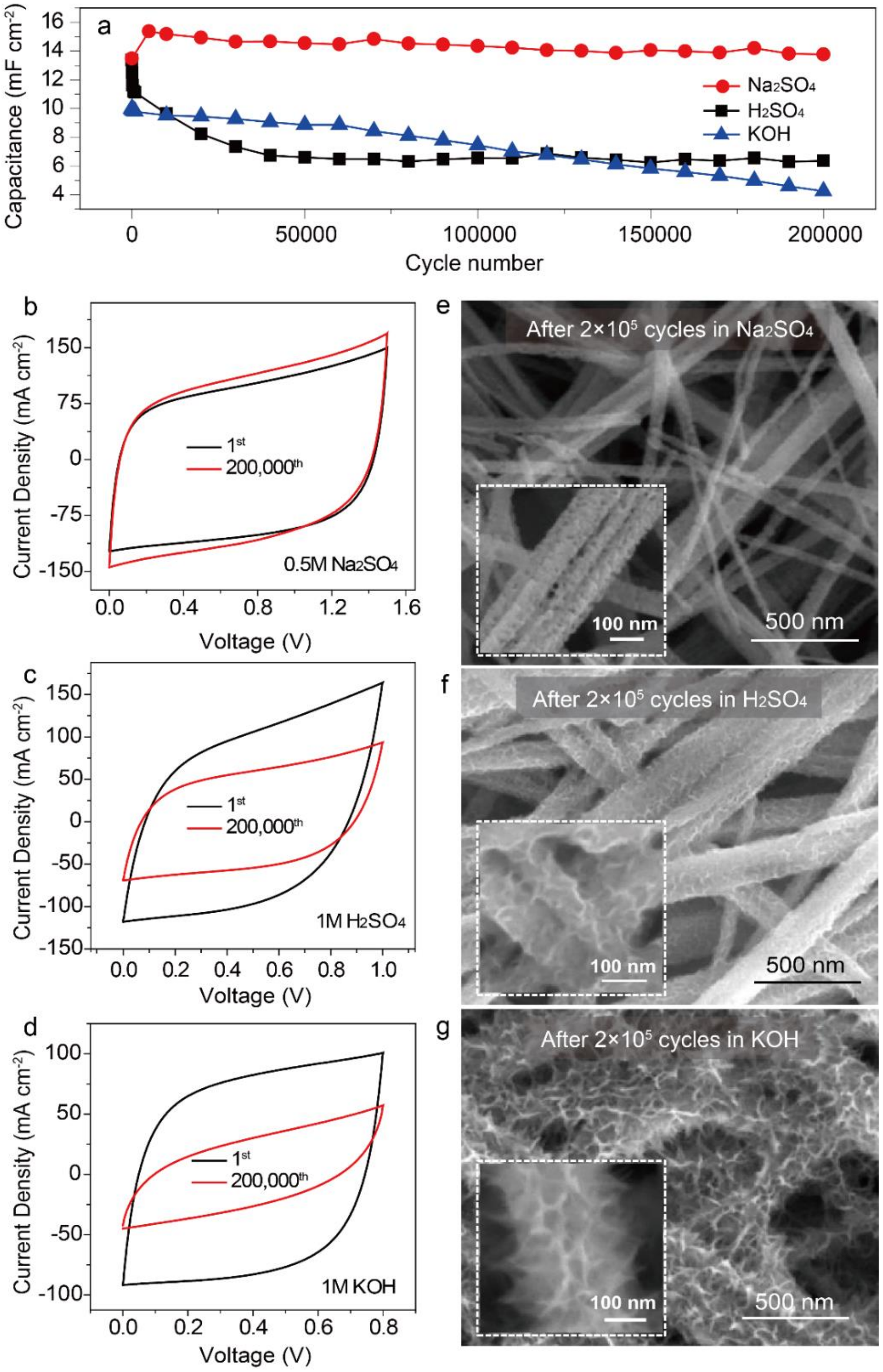

Figure 3.12 (a) Capacitance retention of TiN paper SSC obtained at 1 V s^{-1} in 0.5 M Na_2SO_4, 1.0 M H_2SO_4 and 1.0 M KOH electrolytes are plotted as a function of cycling number. (b, c, d) CV curves of TiN paper SSC collected at the 1st and after the 200000th cycle in 0.5 M Na_2SO_4, 1.0 M H_2SO_4 and 1.0 M KOH electrolytes at 10 V s^{-1}, respectively. (e, f, g) SEM images of the TiN paper electrodes after testing for 200,000 cycles in 0.5 M Na_2SO_4, 1.0 M H_2SO_4 and 1.0 M KOH electrolytes at 1 V s^{-1}, respectively.

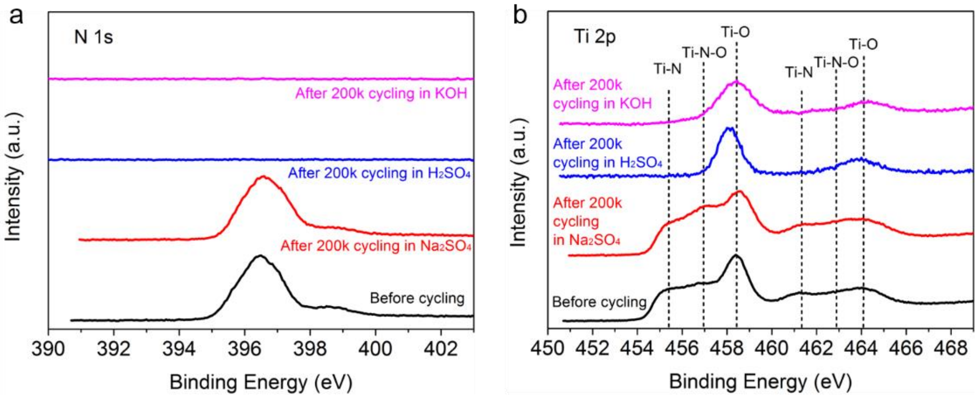

Figure 3.13 Core level N 1s and Ti 2p XPS spectra collected for TiN paper electrodes after testing in different electrolytes (0.5 M Na_2SO_4, 1.0 M H_2SO_4 and 1.0 M KOH) for 200,000 cycles.

The filtration method offers not only an easy way to make paper-like electrode, but also the capability of controlling the electrode thickness and mass loading. We investigated the capacitive performance of TiN paper SSC with different mass loadings. As shown in **Figure 3.14a**, TiN paper SSC retains a rectangular CV curves at a high scan rate of 1 V s^{-1} under different mass loadings. When the mass loading increased from 0.38 to 3.00 mg cm^{-2}, the areal capacitance increases almost linearly, manifesting the gravimetric and volumetric capacitance are not significantly affected with the increased mass loading (**Figure 3.14b**). The thickness/mass loadinginsensitive capacitive behavior makes the TiN paper electrode promising for practical energy storage devices.

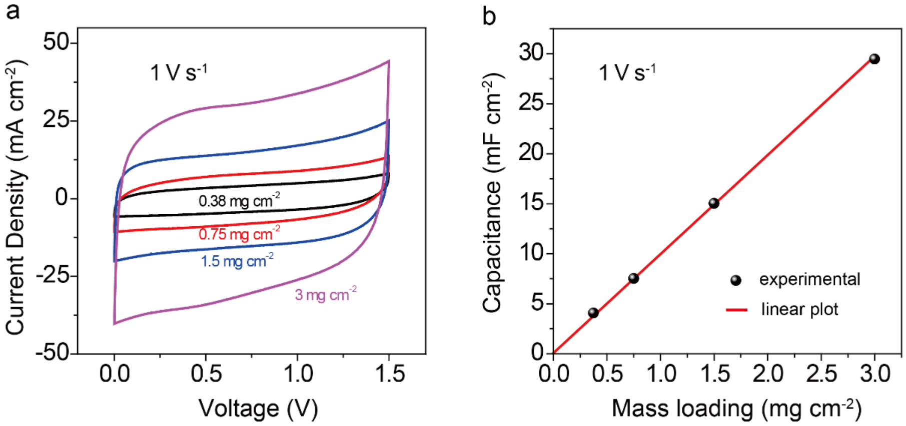

Figure 3.14 (a) CV curves of TiN paper SSC with different mass loadings collected at a scan rate of 1 V s^{-1}. (b) Areal capacitance of TiN paper SSC is plotted as a function of TiN mass loading. The linear plot in the figure is used as a guildline to show the linear increasing trend of areal capacitance as a function of mass loading.

3.4 Conclusions

In summary, we have fabricated a free-standing highly conductive and porous TiN paper electrode that can be operated at an ultrahigh scan rate of 100 V s^{-1} in a wide voltage window of 1.5 V in a Na_2SO_4 electrolyte and shows no capacitance decay in 200,000 charge/discharge cycles. Importantly, the TiN paper SSC exhibits an outstanding response time with a characteristic time constant of 4 ms. This can be attributed to the high conductivity of TiN nanobelts and the efficient ion diffusion in the unique electrode architecture constructed with a network of mesoporous TiN nanobelts. We believe the paper-like electrode fabrication method can be applied to other metal nitride materials and provide an alternative way to make electrodes for ultrafast charging supercapacitors.

References

1. H. S. Kim, J. B. Cook, H. Lin, J. S. Ko, S. H. Tolbert, V. Ozolins, B. Dunn, *Nat. Mater.* **2017**, *16*, 454-460.
2. N. A. Kyeremateng, T. Brousse, D. Pech, *Nat. Nanotechnol.* **2017**, *12*, 7-15.
3. D. Feng, T. Lei, M. Lukatskaya, J. Park, Z. Huang, M. Lee, L. Shaw, S. Chen, A. Yakovenko, A. Kulkarni, J. Xiao, K. Fredrickson, J. Tok, X. Zou, Y. Cui, Z. Bao, *Nat. Energy* **2018**, *3*, 30-36.
4. B. Yao, S. Chandrasekaran, J. Zhang, W. Xiao, F. Qian, C. Zhu, E. B. Duoss, C. M. Spadaccini, M. A. Worsley, Y. Li, *Joule* **2019**, *3*, 459-470.
5. H. Sun, L. Mei, J. Liang, Z. Zhao, C. Lee, H. Fei, M. Ding, J. Lau, M. Li, C. Wang, X. Xu, G. Hao, B. Papandrea, I. Shakir, B. Dunn, Y. Huang, X. Duan, *Science* **2017**, *356*, 599-604.
6. V. Augustyn, J. Come, M. Lowe, J. Kim, P. Taberna, S. Tolbert, H. Abruna, P. Simon, B. Dunn, *Nat. Mater.* **2013**, *12*, 518-522.
7. B. Yao, J. Zhang, T. Kou, Y. Song, T. Liu, Y. Li, *Adv. Sci.* **2017**, *4*, 1700107.
8. M. H. Yu, X. L. Feng, *Joule* **2019**, *3*, 338-360.
9. L. Yuan, B. Yao, B. Hu, K. Huo, W. Chen, J. Zhou, *Energy Environ. Sci.* **2013**, *6*, 470-476.
10. V. Augustyn, P. Simon, B. Dunn, *Energy Environ. Sci.* **2014**, *7*, 1597-1614.

11. Y. Song, T. Liu, B. Yao, M. Li, T. Kou, Z. Huang, D. Feng, F. Wang, Y. Tong, X. Liu, Y. Li, *ACS Energy Lett.* **2017**, *2*, 1752-1759.

12. M. Zhang, Q. Zhou, J. Chen, X. Yu, L. Huang, Y. Li, C. Li, G. Shi, *Energy Environ. Sci.* **2016**, *9*, 2005-2010.

13. N. Kurra, M. K. Hota, H. N. Alshareef, *Nano Energy* **2015**, *13*, 500-508.

14. J. A. Lee, M. K. Shin, S. H. Kim, H. U. Cho, G. M. Spinks, G. G. Wallace, M. D. Lima, X. Lepro, M. E. Kozlov, R. H. Baughman, S. J. Kim, *Nat. Commun.* **2013**, *4*, 1970.

15. D. T. Pham, T. H. Lee, D. H. Luong, F. Yao, A. Ghosh, V. T. Le, T. H. Kim, B. Li, J. Chang, Y. H. Lee, *ACS Nano* **2015**, *9*, 2018-2027.

16. G. H. Lee, J. W. Lee, J. I. Choi, S. J. Kim, Y. H. Kim, J. K. Kang, *Adv Funct Mater* **2016**, *26*, 5139-5148.

17. Z. S. Wu, Z. Liu, K. Parvez, X. Feng, K. Mullen, *Adv. Mater.* **2015**, *27*, 3669-3675.

18. J. Lin, C. Zhang, Z. Yan, Y. Zhu, Z. Peng, R. H. Hauge, D. Natelson, J. M. Tour, *Nano Lett.* **2013**, *13*, 72-78.

19. R. H. Baughman, A. A. Zakhidov, W. A. de Heer, *Science* **2002**, *297*, 787-792.

20. Y. Zhu, S. Murali, M. D. Stoller, K. J. Ganesh, W. Cai, P. J. Ferreira, A. Pirkle, R. M. Wallace, K. A. Cychosz, M. Thommes, D. Su, E. A. Stach, R. S. Ruoff, *Science* **2011**, *332*, 1537-1541.

21. C. Zhu, P. Yang, D. Chao, X. Wang, X. Zhang, S. Chen, B. K. Tay, H. Huang, H. Zhang, W. Mai, H. J. Fan, *Adv. Mater.* **2015**, *27*, 4566-4571.

22. X. Lu, G. Wang, T. Zhai, M. Yu, S. Xie, Y. Ling, C. Liang, Y. Tong, Y. Li, *Nano Lett.* **2012**, *12*, 5376-5381.

23. M.-S. Balogun, W. Qiu, W. Wang, P. Fang, X. Lu, Y. Tong, *J. Mater. Chem. A* **2015**, *3*, 1364-1387.

24. X. Lu, T. Liu, T. Zhai, G. Wang, M. Yu, S. Xie, Y. Ling, C. Liang, Y. Tong, Y. Li, *Adv. Energy Mater.* **2014**, *4*, 1300994.

25. G. Hasegawa, A. Kitada, S. Kawasaki, K. Kanamori, K. Nakanishi, Y. Kobayashi, H. Kageyama, T. Abe, *J. Electrochem. Soc.* **2015**, *162*, A77-A85.

26. B. Yao, L. Huang, J. Zhang, X. Gao, J. Wu, Y. Cheng, X. Xiao, B. Wang, Y. Li, J. Zhou, *Adv. Mater.* **2016**, *28*, 6353-6358.

27. F. Zhang, T. Liu, M. Li, M. Yu, Y. Luo, Y. Tong, Y. Li, *Nano Lett.* **2017**, *17*, 3097-3104.

28. M. Zukalova, J. Prochazka, Z. Bastl, J. Duchoslav, L. Rubacek, D. Havlicek, L. Kavan, *Chem. Mater.* **2010**, *22*, 4045-4055.

29. H.-C. Park, K.-H. Lee, Y.-W. Lee, S.-J. Kim, D.-M. Kim, M.-C. Kim, K.-W. Park, *J. Power Sources* **2014**, *269*, 534-541.

30. L. Yan, G. Chen, S. Tan, M. Zhou, G. Zou, S. Deng, S. Smirnov, H. Luo, *ACS Appl. Mater. Interfaces* **2015**, *7*, 24212-24217.

31. Z. Zhang, J. B. M. Goodall, D. J. Morgan, S. Brown, R. J. H. Clark, J. C. Knowles, N. J. Mordan, J. R. G. Evans, A. F. Carley, M. Bowker, J. A. Darr, *J. Eur. Ceram. Soc.* **2009**, *29*, 2343-2353.

32. M. Harb, P. Sautet, P. Raybaud, *J. Phys. Chem. C* **2011**, *115*, 19394-19404.

33. P. Yang, D. Chao, C. Zhu, X. Xia, Y. Zhang, X. Wang, P. Sun, B. K. Tay, Z. X. Shen, W. Mai, H. J. Fan, *Adv. Sci.* **2016**, *3*, 1500299.

34. S. Oktay, Z. Kahraman, M. Urgen, K. Kazmanli, *Appl. Surf. Sci.* **2015**, *328*, 255-261.

35. R. Chandrasekaran, Y. Soneda, J. Yamashita, M. Kodama, H. Hatori, *J. Solid State Electrochem.* **2008**, *12*, 1349-1355.

36. Y. Xu, Z. Lin, X. Zhong, X. Huang, N. O. Weiss, Y. Huang, X. Duan, *Nat. Commun.* **2014**, *5*, 4554.

37. L. Huang, B. Yao, J. Sun, X. Gao, J. Wu, J. Wan, T. Li, Z. Hu, J. Zhou, *J. Mater. Chem. A* **2017**, *5*, 2897-2903.

38. K. S. Kim, Y. Zhao, H. Jang, S. Y. Lee, J. M. Kim, K. S. Kim, J.-H. Ahn, P. Kim, J.-Y. Choi, B. H. Hong, *Nature* **2009**, *457*, 706.

39. U. N. Maiti, J. Lim, K. E. Lee, W. J. Lee, S. O. Kim, *Adv. Mater.* **2014**, *26*, 615-619.

40. L. Hu, J. W. Choi, Y. Yang, S. Jeong, F. La Mantia, L. F. Cui, Y. Cui, *Proc. Natl. Acad. Sci. U.S.A.* **2009**, *106*, 21490-21494.

41. L. Yuan, X. Xiao, T. Ding, J. Zhong, X. Zhang, Y. Shen, B. Hu, Y. Huang, J. Zhou, Z. L. Wang, *Angew. Chem. Int. Ed.* **2012**, *51*, 4934-4938.

42. Z. Li, G. Ma, R. Ge, F. Qin, X. Dong, W. Meng, T. Liu, J. Tong, F. Jiang, Y. Zhou, K. Li, X. Min, K. Huo, Y. Zhou, *Angew. Chem. Int. Ed.* **2016**, *55*, 979-982.

43. T. Zheng, M. H. Tahmasebi, B. Li, Y. Li, S. Ran, T. S. Glen, K.-H. Lam, I.-S. Choi, S. T. Boles, *ChemElectroChem* **2018**, *5*, 2199-2207.

44. F. Grote, H. Zhao, Y. Lei, *J. Mater. Chem. A* **2015**, *3*, 3465-3470.

45. P. Sun, R. Lin, Z. Wang, M. Qiu, Z. Chai, B. Zhang, H. Meng, S. Tan, C. Zhao, W. Mai, *Nano Energy* **2017**, *31*, 432-440.

46. E. Kao, C. Yang, R. Warren, A. Kozinda, L. Lin, *Sensor. Actuat. a-Phys.* **2016**, *240*, 160-166.

47. L. Demarconnay, E. Raymundo-Piñero, F. Béguin, *Electrochem. Commun.* **2010**, *12*, 1275-1278.

48. Q. Gao, L. Demarconnay, E. Raymundo-Pinero, F. Beguin, *Energy Environ. Sci.* **2012**, *5*, 9611-9617.

49. T. Lin, I. Chen, F. Liu, C. Yang, H. Bi, F. Xu, F. Huang, *Science* **2015**, *350*, 1508-1513.

50. K. Fic, G. Lota, M. Meller, E. Frackowiak, *Energy Environ. Sci.* **2012**, *5*, 5842-5850.

51. H. Cui, G. Zhu, X. Liu, F. Liu, Y. Xie, C. Yang, T. Lin, H. Gu, F. Huang, *Adv. Sci.* **2015**, *2*, 1500126.

52. B. Gao, X. Xiao, J. Su, X. Zhang, X. Peng, J. Fu, P. K. Chu, *Appl. Surf. Sci.* **2016**, *383*, 57-63.

53. X. Lu, M. Yu, T. Zhai, G. Wang, S. Xie, T. Liu, C. Liang, Y. Tong, Y. Li, *Nano Lett.* **2013**, *13*, 2628-2633.

54. Y. Liu, R. Xiao, Y. Qiu, Y. Fang, P. Zhang, *Electrochimica Acta* **2016**, *213*, 393-399.

55. P. Xu, T. Gu, Z. Cao, B. Wei, J. Yu, F. Li, J.-H. Byun, W. Lu, Q. Li, T.-W. Chou, *Adv. Energy Mater.* **2014**, *4*, 1300759-1300764.

56. W. Bao, A. K. Mondal, J. Xu, C. Wang, D. Su, G. Wang, *J. Power Sources* **2016**, *325*, 286-291.

57. V. Presser, L. Zhang, J. J. Niu, J. McDonough, C. Perez, H. Fong, Y. Gogotsi, *Adv. Energy Mater.* **2011**, *1*, 423-430.

58. M. El-Kady, V. Strong, S. Dubin, R. Kaner, *Science* **2012**, *335*, 1326-1330.

59. D. Pech, M. Brunet, H. Durou, P. Huang, V. Mochalin, Y. Gogotsi, P. L. Taberna, P. Simon, *Nat. Nanotechnol.* **2010**, *5*, 651-654.

60. T. Liu, Z. Zhou, Y. Guo, D. Guo, G. Liu, *Nat. Commun.* **2019**, *10*, 675.

61. X. Xiao, X. Peng, H. Jin, T. Li, C. Zhang, B. Gao, B. Hu, K. Huo, J. Zhou, *Adv. Mater.* **2013**, *25*, 5091-5097.

62. Y. Xie, Y. Wang, H. Du, *Mater. Sci. Eng. B* **2013**, *178*, 1443-1451.

63. C. F. Windisch, J. W. Virden, S. H. Elder, J. Liu, M. H. Engelhard, *J. Electrochem. Soc.* **1998**, *145*, 1211-1218.

64. S. D. Chyou, H. C. Shih, T. T. Chen, *Corros. Sci.* **1993**, *35*, 337-347.

65. G. Q. Ma, Z. Wang, B. Gao, T. P. Ding, Q. Z. Zhong, X. Peng, J. Su, B. Hu, L. Y. Yuan, P. K. Chu, J. Zhou, K. F. Huo, *J. Mater. Chem. A* **2015**, *3*, 14617-14624.

Chapter 4

3D-printed Resorcinol-Formaldehyde-derived Porous Carbon Aerogels for Supercapacitors

Abstract

The use of additive manufacturing to 3D print aerogels has the potential to impact several important technologies such as energy storage, catalysis, and desalination. While there has been a great deal of focus on graphene aerogels, reports of 3D printed conventional carbon aerogels (CAs) are sparse. Activated CAs are particularly compelling because in addition to having a lower cost than a comparable graphene aerogel, they can achieve much higher surface areas (>3000 m^2/g). Herein we report a 3D printable ink based on traditional resorcinol-formaldehyde sol-gel chemistry that can produce a final activated carbon aerogel with surface areas approaching 2000 m^2/g and good electrical conductivities (~200 S/m). Direct ink writing (DIW) is used to then fabricate electrodes, which demonstrate excellent electrochemical properties with a high specific capacitance of 215.0 F/g at 1 A/g and 83% capacitive retention at higher current densities (10 A/g). The DIW electrode significantly outperformed its bulk counterpart and provides an example of how one can use 3D printed aerogel electrodes to overcome mass transport limitations and boost energy storage performance.

4.1 Introduction

Carbon aerogels (CAs) are unique porous solids with network structures consisting of interconnected carbon particles and, as a result, these materials exhibit many interesting properties, such as high surface-to-volume ratios, continuous porosities and high electrical conductivity.[1] These porous aerogels are currently used in a variety of applications which include catalysis, energy storage, and sorbents.[2-5] Baumann et al., reported synthesis of ultra-high surface area carbon aerogel monoliths (obtained from resorcinol and formaldehyde) through thermal activation[6]. By controlling the mass loss during thermal activation with CO_2, the formation of micropores (pores with diameters less than 2 nm) yielded carbon aerogels with surface areas as high as 3000 m^2/g.[7] These activated carbon aerogels (ACAs) possessed a unique bimodal porosity where the presence of micropores etched into the walls of micron-sized channels could facilitate ion diffusion and produce large capacitances. Therefore, these ACAs are attractive candidates for electrical energy storage devices (supercapacitors, batteries, etc.) and are currently being developed as electrode materials for desalination via capacitive de-ionization.[8-9]

The use of additive manufacturing to print 3D porous carbons has been primarily demonstrated via micro-extrusion of graphene-based inks or carbonization of 3D-printed polymer resins.[10-20] For energy storage applications, Zhu et al., used direct ink writing (DIW) to 3D print a graphene aerogel electrodes that exhibited enhanced mechanical properties, good electrical conductivities, and surface areas up to 740 m^2/g.[17] Capacitive retention of the 3D printed microlattices was an exceptional 90% from current densities of 0.5 A/g to 10 A/g for thick (*ca.* 1 mm) electrodes. This extraordinary performance was attributed to the macropore architecture made possible by 3D printing the electrode. Given the modest surface areas (less than 1000 m^2/g) and corresponding capacitance (ca. 70 F/g) of this example, one would expect that a 3D printed ACA with surface areas in excess of 1000 m^2/g should provide a significant boost to electrode performance. Gao et. al., also fabricated graphene oxide aerogels through direct ink writing, and reported their performance for supercapacitor applications.[21] However, to date, there are no reports of 3D printable ACAs. In this study, we report the development of 3D printable acid-catalyzed resorcinol-formaldehyde (RF) organic aerogel. The organic aerogel ink is printed via DIW by extruding the ink through nozzles as small as 100 μm in diameter. The organic aerogels are then converted to electrically conductive 3D printed CAs (DIW-CA) via pyrolysis in nitrogen making them suitable as electrodes. The electrodes (DIW–CA) are then activated using CO_2 to increase the surface area to almost 2000 m^2/g. These high surface area DIW-ACA electrodes exhibit capacitances over 200 F/g, much higher than that of the DIW-CA and previously reported 3D printed electrodes. Furthermore, by changing the ligament diameter of the 3D printed electrodes, a significant improvement in the capacitive retention is observed, revealing the superiority of high resolution 3D printing techniques. This work demonstrates the value of leveraging conventional organic sol-gel methods in 3D printing technologies to overcome some of the traditional limitations of aerogels. Specifically, engineering macroporosity into large surface area DIW-ACA electrodes allows one to simultaneously realize high capacitance and good capacitive retention.

4.2 Experimental Section

Fabrication of the 3D printed electrodes

Resorcinol (R) and formaldehyde solution (F) (37.0 wt%) purchased from Sigma Aldrich were used to prepare the organic aerogels. Predetermined amounts of formaldehyde solution (1.700 g), DI water (1.500 g) was mixed with 6.0 wt% of hydroxypropyl methyl cellulose (purchased from DOW chemicals). The mixture is sonicated in a temperature-controlled bath for 24 h. To this mixture, 1.230 g of R and 44.0 μL of glacial acetic acid. To further tailor the ink to be thixotropic, 9wt% of Carbosil-EH5 fumed silica, was added and mixed in the Thinky mixture at 2000 rpm for 5 minutes. The as-prepared ink is loaded into a 3.0 ml syringe barrel (EFD) and centrifuged for a minute at 4500 rpm to remove air bubbles, after which the ink is extruded through a micro nozzle (400 µm diameter) to pattern 3D structures on a glass substrate. For direct ink writing, the syringe was attached by a luer-lock to a smooth-flow tapered nozzle whose inner diameter(d) is 400 µm. The ink was then extruded by means of an air powered fluid dispenser (Ultimus V, EFD) which provides an appropriate pressure (in the range of 12-15 psi) for writing and the writing speed was kept at 3 mm/sec for all the 3D printed structures. Simple cubic lattices with multiple orthogonal layers of parallel cylindrical rods were printed alternately. The diameter of the cylindrical rods equals the diameter of nozzle (d) and the center-to-center rod spacing (L) was varied depending on the type of electrode. The height of the electrodes was varied from 1 mm to 3 mm and the layers were stacked on the structure such that each layer has a z spacing of 60% the diameter of the nozzle diameter. To avoid cracking or drying due to evaporation of water, soon after printing, the 3D printed structures are immersed in a jar containing solvent (iso-octane) and cured in an oven at 80°C for 72 h to form organic aerogels.

Carbonization and activation of aerogels

This process involves carbonizing the super-critically dried RF gels to form carbon aerogels (CAs). The aerogels were subjected to a heat treatment process where the samples were heated in a tube furnace under nitrogen atmosphere at 1050 °C for 3 h with a heating and cooling rate of 2 °C/min. The carbonized 3D printed graphene based CAs were then etched with hydrofluoric acid to remove fumed silica. The etched parts were again subjected to a three-day solvent (acetone) exchange followed by super critical drying. Activation was done thermally, according to a previous study[6]. This process involves the use of the Boudouard reaction, CO_2 reacting to carbon at 950 °C to evolve CO, to controllably etch small pores in the CA.[28-31] In this case, the CA was thermally activated until a 60% mass loss of the sample was obtained. The DIW-ACA electrodes weighed *ca.* 3.00 mg.

Characterization

Nitrogen Porosimetry. Textural properties were determined by Brunauer-Emmett-Teller (BET) and Barrett-Joyner-Halenda (BJH) methods using an ASAP 2020 Surface Area Analyzer (Micromeritics Instrument Corporation) via nitrogen porosimetry.[32-33] Samples of approximately 0.1 g were heated to 423 K under vacuum (10^{-3} Pa) for at least 24 hours to remove all adsorbed species. Scanning electron micrographs in Fig. 2 was obtained with a JEOL7401-F SEM at a 5kV accelerating voltage.

The electrochemical measurements were carried out using electrochemical workstation (CHI 660D and EC-Lab SP-300) in a three-electrode electrolytic cell under 3.0 M KOH aqueous solution. The working electrodes were prepared by pressing carbon aerogels in between two pieces of nickel foams. A piece of carbon foil and Hg/HgO electrode were working as counter electrode and reference electrode, respectively.

Calculation

Gravimetric capacitance (C_g) of single electrodes are calculated based on the galvanostatic charging and discharging curves using the following equation.[34]

$$C_g = \frac{I\times t}{\Delta U\times m} \quad \text{(Equation 1)}$$

Where C_g is the gravimetric capacitance (F g^{-1}), ΔU is the potential window (V), I is the discharge current (A), t is the discharge time (s), and m is the mass loading of the materials on the electrodes (g).

Volumetric capacitance (C_v) of single electrodes are calculated based on the galvanostatic charging and discharging curves using the following equation.

$$C_v = \frac{I\times t}{\Delta U\times V} \quad \text{(Equation 2)}$$

Where C_v is the volumetric capacitance (F cm^{-3}), ΔU is the potential window (V), I is the discharge current (A), t is the discharge time (s), and V is the volume of the electrodes (cm^3).

4.3 Results and Discussions

The key challenge to 3D printing conventional organic aerogels is the formulation of a printable ink. The conventional RF aerogel monoliths are synthesized by mixing resorcinol (1.230 g, 0.112 mol) and 37% formaldehyde solution (1.700 g, 0.224 mol) in water (1.5 ml), followed by the addition of glacial acetic acid (0.440 g, 0.007 mol), which was further cured at 80 °C for 72 h. To form a homogenous thixotropic ink the RF polymer is mixed with hydroxy propyl methyl cellulose and fumed silica particles. Since the formulation contains mostly water, cellulose serves as a viscosifier to meet the rheology requirements of reliable flow through the nozzle (of diameter as small as 100 μm) under shear. Even though the mixture forms a stiff gel, upon addition of resorcinol and acetic acid to the formaldehyde-cellulose mixture, the RF-cellulose mixture loses its stiffness in the gel. This is due to the endothermic reaction that occurs between resorcinol and formaldehyde via sol-gel chemistry. Fig. 4.1a shows the viscosity of the as-prepared RF ink containing cellulose and silica as a function of shear rate, revealing a shear thinning behavior which is necessary for a printable ink. It is evident from the graphs that addition of fumed silica particles (purchased from Carbosil EH5), improves viscosity and imparts additional stiffness to enhance the printability of the ink. RF inks without silica filler exhibit a plateau of its storage modulus G′ at 300 Pa. Meanwhile, the addition of 9.0 wt% silica particles to RF-cellulose ink increases the modulus by 2 orders of magnitude. Although there is not a significant difference in the viscosity of the RF inks with and without cellulose, the storage modulus of the RF ink without silica drops drastically at very low shear stress of 10 Pa. Fig. 4.1b also shows that the inclusion of cellulose alone results in an ink with a stiffness (<10^3 GPa) much lower than that previously reported for GO ink[12].

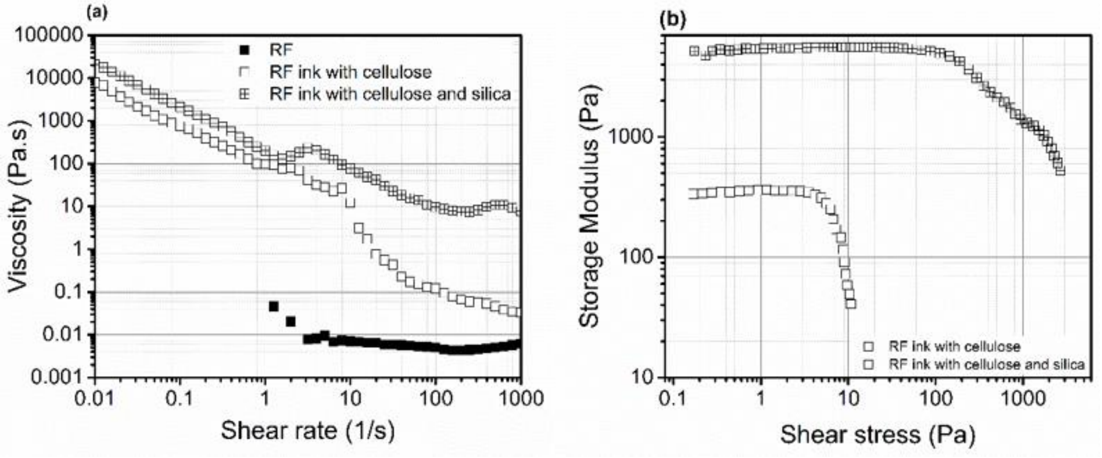

Figure 4.1 Log-log plots of (a) viscosity as a function of shear rate and (b) storage modulus as a function of shear stress of RF inks.

Fig. 4.2a shows the storage modulus of the RF ink measured as a function of time. Since the RF sol-gel process is dynamic with time, it is necessary to monitor the change in the stiffness of the ink over time. As expected, the addition of silica particles increases the stiffness and shear yield stress of the inks but does not appear to interfere with the sol-gel chemistry of the RF inks. So in addition to imparting shear-thinning behavior, silica increased storage modulus to 10^5 GPa which is on par with the previously developed GO inks[12].

(a) Shear modulus of the ink

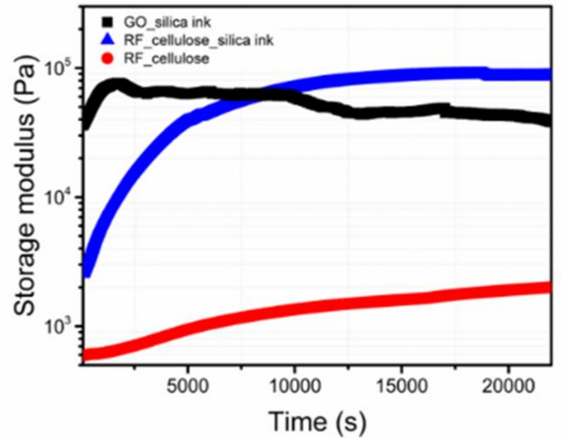

(b) DIW-CA

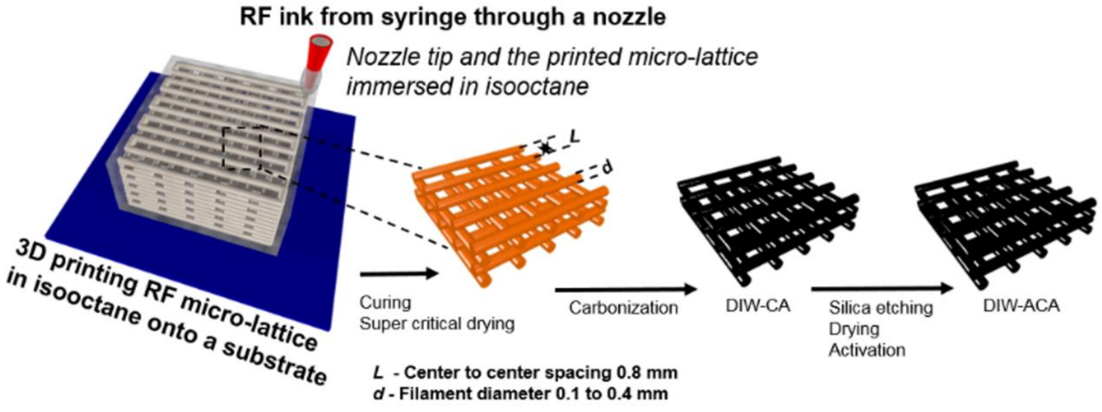

(c) Traditional Carbon Aerogel synthesis

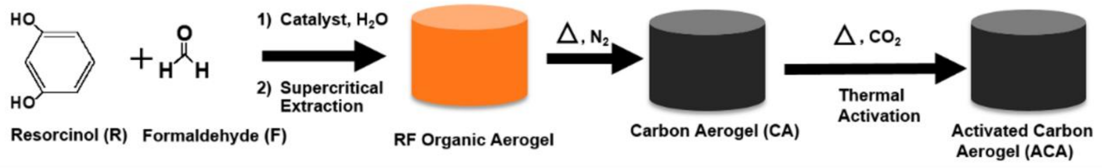

Figure 4.2 (a) Rheology data of the ink where shear modulus is measured as a function of time, (b) schematic diagram of the DIW printed carbon aerogels and (c) traditional CA synthesis schematic.

After the ink rheology is properly tuned, it is then loaded into a syringe barrel (3.0 ml or 20.0 ml in volume). The ink is then centrifuged at 4500 rpm for 2 minutes to remove trapped gas, after which the ink is extruded through a micro nozzle (100-400 µm in diameter at the tip opening) to pattern 3D structures. A schematic of the 3D printing and traditional methods for making the DIW-ACA and ACA, respectively, is shown in Fig. 4.2b-c. For the DIW-ACA, cubic lattices with multiple orthogonal layers of parallel cylindrical rods are printed alternately. The diameter of the cylindrical rods equals the inner diameter of the nozzle and the center-to-center rod spacing is kept constant at 0.8 mm. The z-spacing during the print is set to 60 % of the nozzle diameter and the number of layers stacked on the structure is varied to achieve the desired thickness of the final electrode. To create organic aerogels, the printed structures must remain wet during printing and gelation so that the gels can be dried via supercritical drying to avoid collapse of pores due to capillary forces. Therefore, during printing the part was immersed in an organic solvent (2,2,4-trimethyl-pentane) that is immiscible with the aqueous RF ink.

After printing, the RF parts on the glass substrate are carefully placed in a container with the solvent (2,2,4-trimethyl-pentane) and sealed tightly before being placed in the oven for gelation at 80 °C for 72 h. Once gelled, the aqueous solvent is removed by soaking the 3D printed parts in an acetone bath for 3 days with exchange of acetone every 24 h. The samples are then super critically dried using liquid CO_2. To form CAs, the dried 3D printed RF aerogels are subjected to a carbonization step where the samples are heated in a tube furnace under nitrogen atmosphere at 1050 °C for 3 h. These carbonized aerogels are denoted as DIW-CA. After carbonization, the silica particles incorporated in DIW-CAs are etched with hydrofluoric acid similar to the previous work[17]. To activate these aerogels, the samples are heated to 950 °C under CO_2 atmosphere. By tuning the time of exposure of the samples to CO_2, a controlled etching of carbon framework is carried out. This results in the formation of new micropores which in turn increases the surface area. In the present study, the time of exposure was adjusted until a mass loss of nearly 60±2 % was achieved after the activation and the obtained samples are referred to as DIW-ACA.

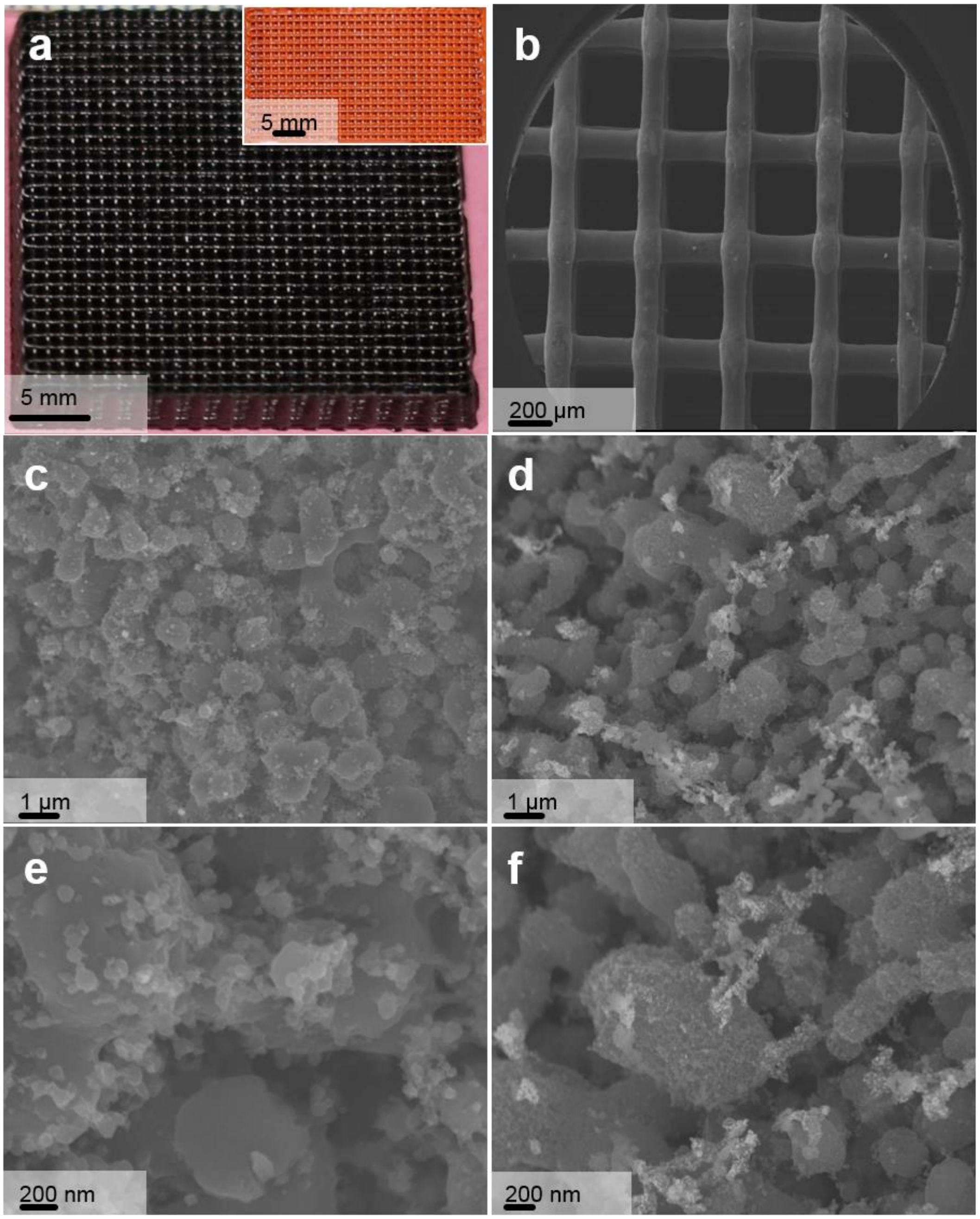

Figure 4.3 (a) Digital photograph and (b) SEM image of DIW-CA. Magnified SEM images of (c, e) DIW-CA and (d, f) DIW-ACA. Inset in (a) shows 3D-printed organic aerogel before carbonization.

Fig. 4.3a shows an optical image of a DIW-CA where the inset - an optical image shows the 3D printed RF aerogel before carbonization. The printed DIW-CA lattice maintains its structural integrity through a series of post-processing steps (e.g., solvent exchange, gelation, carbonization, activation). The scanning electron micrograph of the DIW-CA cubic lattice (Fig. 4.3b) contains parallel cylindrical filaments with multiple orthogonal layers piled on top of each other. Unlike, the GO inks reported earlier[12, 17], during printing, the RF inks are relatively soft and hence the filaments became ellipsoidal at cross-over points in the lattice. These 3D simple cubic lattices are designed with an in-plane center-to-center rod spacing (*L*) of 0.80 mm and a rod diameter (*d*) of 0.25 mm, resulting in a spacing-to-diameter ratio (*L/d*) of *ca.* 3. The printed sample in Fig. 3a was printed with a print speed of 3 mm/sec, a pressure of 16 psi was applied to extrude the ink from the syringe barrel. For every incremental layer, the nozzle moves up by 0.15 mm or 0.24 mm depending on the nozzle diameter in the z-direction. Note, that the samples undergo a volumetric shrinkage of 21 % during gelation, drying and carbonization. Hence, while printing this shrinkage is taken into consideration while setting the dimensions of the sample.

Upon closer examination (Fig. 4.3c) the morphology of the DIW-CA reveals a network of interconnected, fairly smooth micron-sized carbon ligaments that define a continuous macroporous network. This pore morphology is consistent with earlier reports of conventional CAs[6]. The macroporous network results in a relatively low surface area of 26 m^2/g. This relatively low surface area is due to the lack of microporosity in the DIW-CA (Table 4.1) which provided significant surface area for the pre-activated CA in previous reports. After activation resulting in 60 % mass loss, the surface area for the DIW-ACA increases to over 1800 m^2/g which is on the same order of that observed in other activated CAs[6]. Figure 4.3d reveals that after activation, the surface of the carbon particles is much rougher, and a much finer network structure emerges after the CO_2 activation.

Table 4.1 Physical properties of the 3D printed carbon aerogels

Sample	**Density (g/cm^3)**	**BET Surface Area (m^2/g)**	**Total Pore Volume (cm^3/g)**	**Micropore Pore Volume (cm^3/g)**	**Electrical Conductivity (S/m)**
DIW-CA	0.47	26.5	0.083	0.004	995
DIW-ACA	0.24	1894	0.746	0.638	180

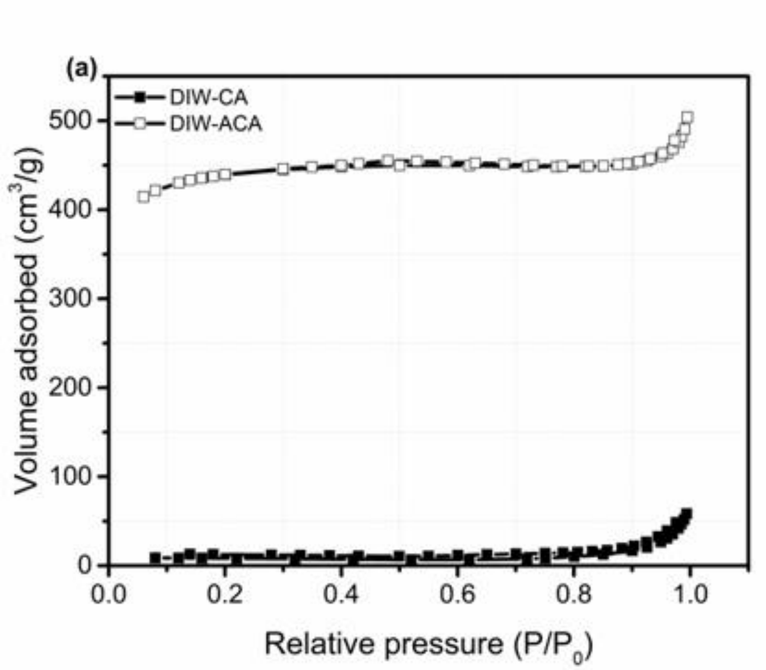

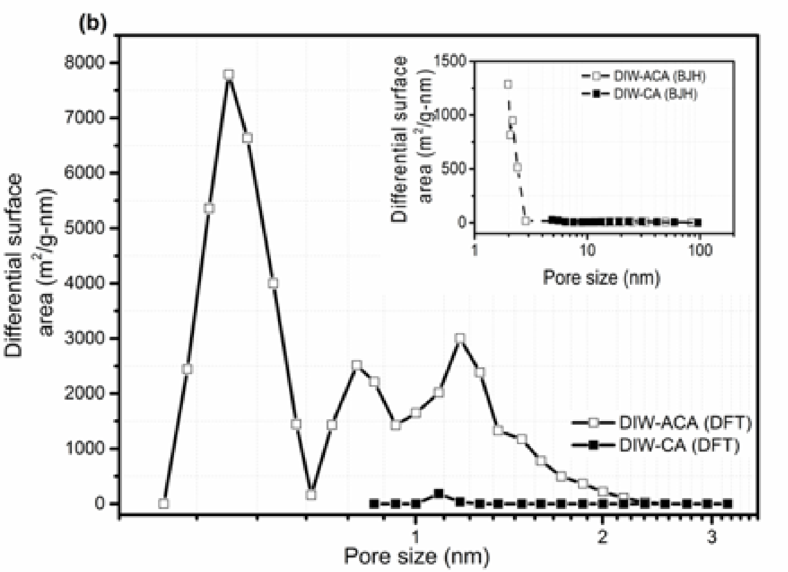

Figure 4.4 (a) Nitrogen adsorption/desorption isotherms and (b) pore size distribution of DIW-CA and DIW-ACA.

The microporous nature of the DIW-ACA is especially clear when examining the type II nitrogen adsorption-desorption isotherms in Fig. 4.4a with large absorbed volumes at low relative pressures. Other physical properties of the DIW-CA and DIW-ACA are summarized in Table 4.1. The two orders of magnitude increase in micropore volume suggests that a significant portion of this additional surface area is due to the formation of micropores. The pore size distributions as determined by Barrett-Joyner-Halenda (BJH) and density functional theory (DFT) methods support this conclusion (Fig. 4.4b). DIW-ACA, unlike the DIW-CA, contained significant microporosity with a sharp increase in surface area at low pore sizes. The BJH method does not accurately determine pore size in the micropore regime (<2 nm) so further analysis via DFT method was performed. Micropore analysis confirmed that nearly all the surface area in the DIW-ACA was due to newly formed pores less than

3 nm in diameter. These micropores give the DIW-ACA surface areas 3-50 times higher than other 3D-printed carbon-based aerogels[12, 15-16]. Together with good electrical conductivity (180 S/m), the DIW-ACA should be a promising electrode material for water purification, electrocatalysis, and energy storage.

The electrochemical performances of the Bulk-CA (*i.e.* CA without architected pores), DIW-CA, and DIW-ACA (1.8 mm thick) electrodes, were evaluated in a three-electrode electrolytic cell in 3M KOH aqueous solution. The cyclic voltammetry (CV) curves and the galvanostatic charge discharge (GCD) curves are presented in Fig. 4.5a-f.

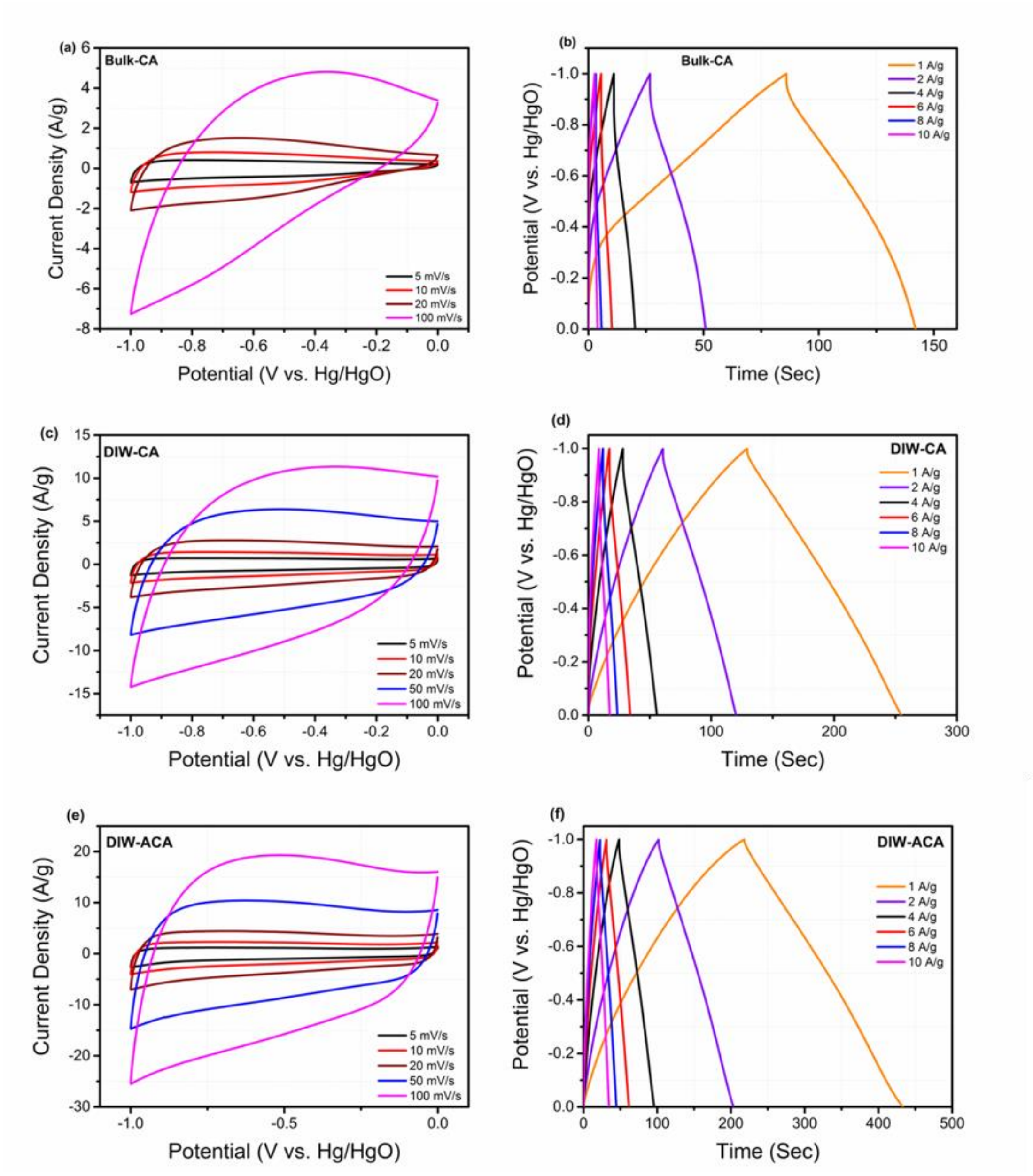

Figure 4.5 Electrochemical performance of Bulk-CA, DIW-CA and DIW-ACA. (a, c and e) Cyclic voltammograms collected as a function of scan rate. (b, d and f) Galvanostatic charge and discharge profiles collected at different current densities.

The CV and GCD curves provide good illustrations of how the pore architecture and surface area impact the capacitive performance of aerogels. The Bulk-CA represents the case without architected porosity, limited to native, random pores of 1 μm and below. Due to the limitations that this pore structure puts on mass transport within thick Bulk-CA, the CV curves exhibit gross distortions from the ideal rectangular shape at higher scan rates and the GCD curves deviate sharply from the ideal symmetric triangle (Fig. 4.5a and b). By contrast, simply adding architected macropores, DIW-CA, produces CV curves with a much more rectangular and triangular shape for the CV and GCD curves, respectively. Finally, adding surface area to the electrode with architected micropores, DIW-ACA, yields CV and GCD curves that are even closer to the ideal shapes indicative of excellent capacitive performance. In particular, DIW-ACA electrodes exhibit considerably enhanced gravimetric capacitance compared with the DIW-CA electrodes. This enhancement in capacitance can be ascribed to the substantially increased specific surface area after thermal activation, which provides more accessible surface area for the electrolyte ions for diffusion. It is presumed that all the surface area detected by nitrogen porosimetry (>1800 m^2/g) in the DIW-ACA is not electrochemically active as there is only factor of two increase in capacitance between the DIW-ACA and DIW-CA while the surface area increases by two orders of magnitude. Efforts to increase the electrochemically active area is being pursued in a separate study. The small *iR* drop in the GCD curves indicate the small internal resistance of the electrodes. DIW-ACA electrodes with a longer discharge time than DIW-CA at all current densities also reflect the increased specific capacitance of activated carbon aerogels[22].

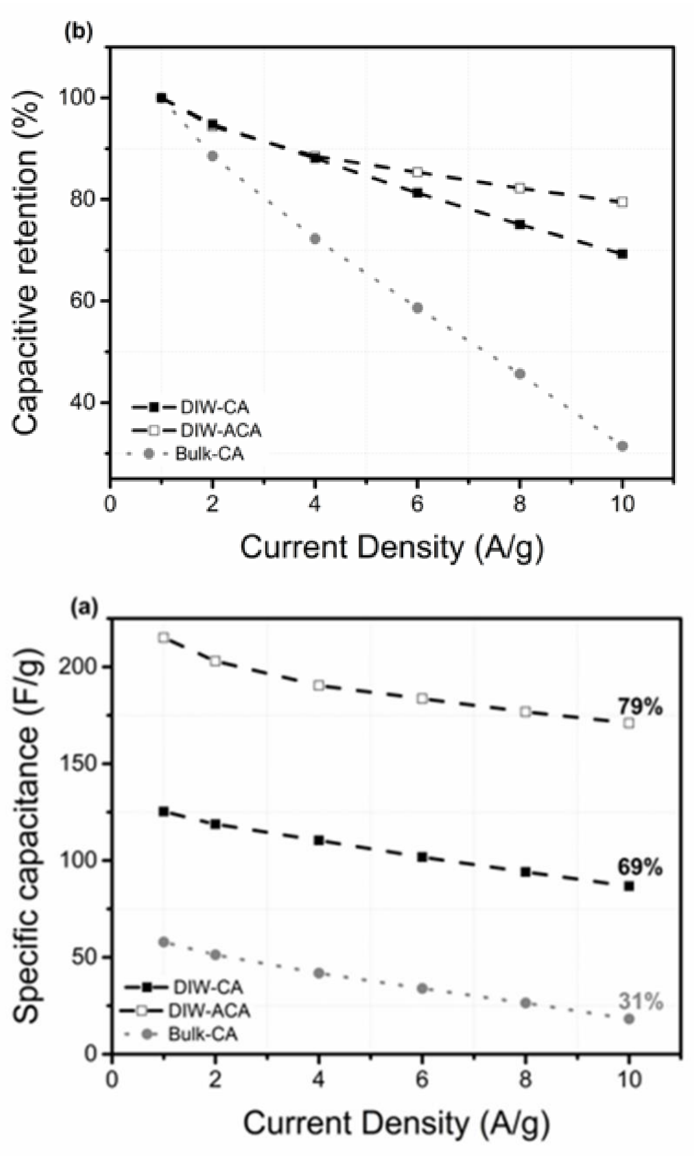

Figure 4.6 (a) Specific capacitance and (b) capacitive retention of DIW-CA, DIW-ACA and bulk-CA.

The specific capacitance for each sample is calculated from the GCD curves collected at different current densities and are summarized in Fig. 4.6a. Comparing the DIW-CA with Bulk-CA (bulk discs prepared and processed in the same manner as DIW-CA) the specific capacitance of the DIW-CA (125 F/g at 1 A/g, 88 F/cm^3 at 1

A/g) is nearly twice that of the Bulk-CA-ink (57 F/g at 1 A/g, 58 F/cm^3 at 1 A/g). As the only difference between the Bulk-CA and DIW-CA is the 3D printed macroporosity (e.g. surface area, conductivity, pore size, etc. are equal), this result suggests that the macropores of the DIW-CA significantly improve ion accessibility[17, 23]. Comparing the DIW-CA and DIW-ACA we see a further increase in capacitance. The DIW-ACA exhibited a high gravimetric capacitance of 215 F/g (103 F/cm^3) at a current density of 1 A/g, which is almost twice as much as that of DIW-CA (125 F/g at 1 A/g, 88 F/cm^3 at 1 A/g). This enhancement in capacitance is attributed to the increased surface area after thermal activation. The gravimetric capacitance of DIW-ACA exceeds the previously reported GO-GNP composite aerogel exhibiting 70 F/g at low current densities[17]. As the current density is increased, efficient electron transport and ion diffusion are necessary for charge build up and the resistance of the sample plays a vital role in the rate capability of the electrode. Both DIW-CA and DIW-ACA also have good capacitive retention of 69% and 79% (Fig. 4.6b) respectively at higher current density (10 A/g), which is more than twice that of the Bulk-CA. After activation, the gravimetric capacitance has been increased, and the rate capability has also been increased, suggesting that the increased porosity after activation improves the ion accessibility. The improved rate capability observed with the DIW-CA and DIW-ACA confirm the importance of using engineered macropores in aerogel electrodes for enhancing charged species transport.

3D printing enables an ordered macropore electrode architecture which facilitates mass transfer by reducing the ion diffusion resistance. To understand the correlation between macroporosity and capacitive performance, electrodes were printed with different nozzle diameters (*d*) (400, 200 and 100 µm) with center-to-center rod spacing (*L*) of 800 µm and the height of the printed electrodes were kept constant to 1.5 mm. DIW-CA electrodes with varied spacing-to-diameter ratio (*L/d*) of 2 (800/400), 4 (800/200) and 8 (800/100) were synthesized in a similar fashion and addressed as DIW-CA-2, DIW-CA-4, and DIW-CA-8, respectively. The electrochemical performance of these samples along with their CV and GCD curves are presented in Fig. 4.7a-f.

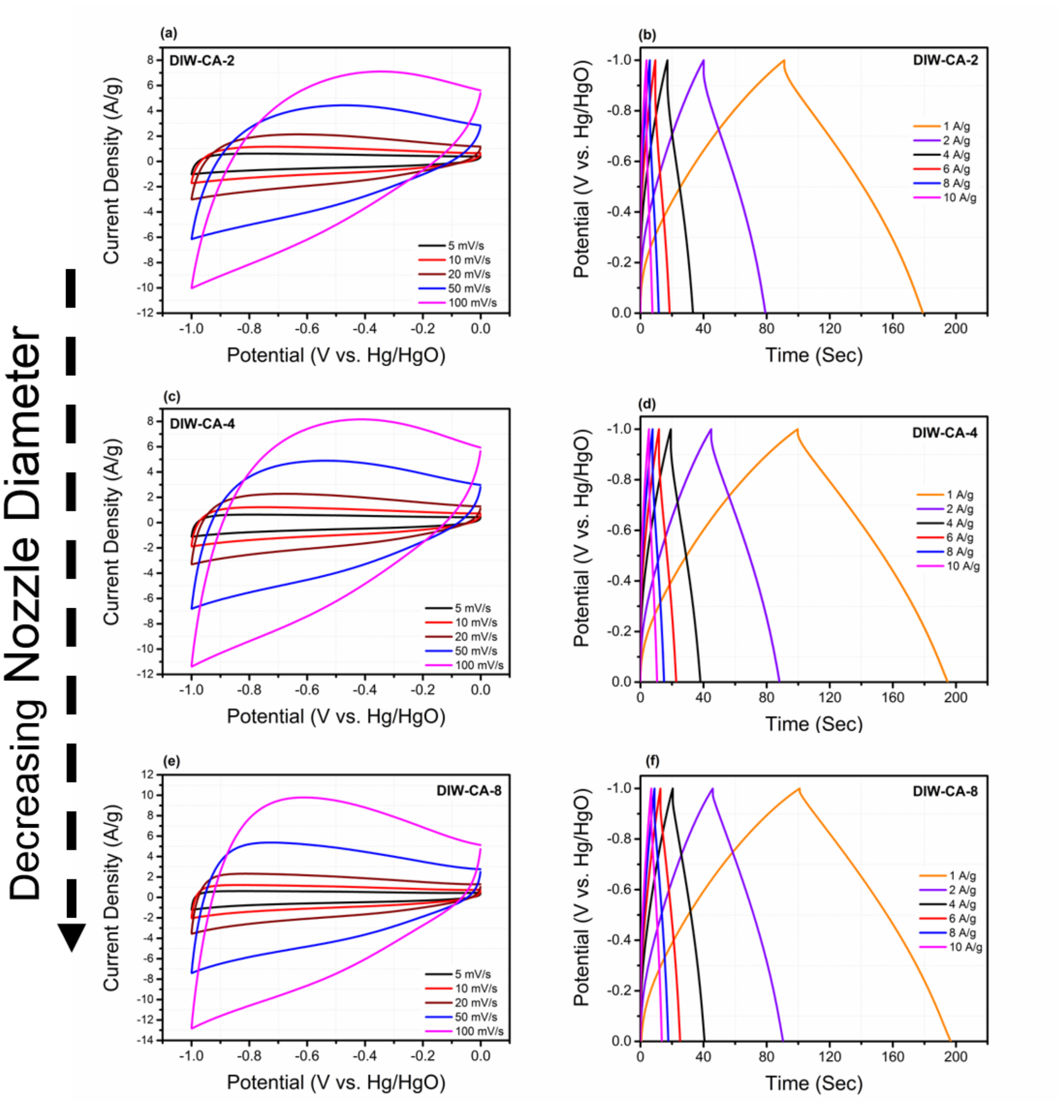

Figure 4.7 (a-c) CV curves and (d-f) GCD curves for DIW-CA-2, DIW-CA-4, and DIW-CA-8, respectively.

As can been seen in Fig. 4.7, when the nozzle diameter decreases from 400 μm to 100 μm, the CV curves (Fig. 4.7a, c, e) collected at higher scan rate (100 mV/s) have larger hysteresis loops which suggests better charge transfer through the ligaments as the ion diffusion length decreases with decreasing the nozzle diameter.

The GCD curves (Fig. 4.7b, d, f) show an increase in discharge time as the nozzle diameter is decreased from 400 µm to 100 µm at a current density of 1 A/g. Although the DIW-CA electrodes with 200 µm and 400 µm show comparable gravimetric and volumetric capacitance under small current densities, their capacitive differences became more obvious when the current is increased. This data is summarized in Fig. 8.

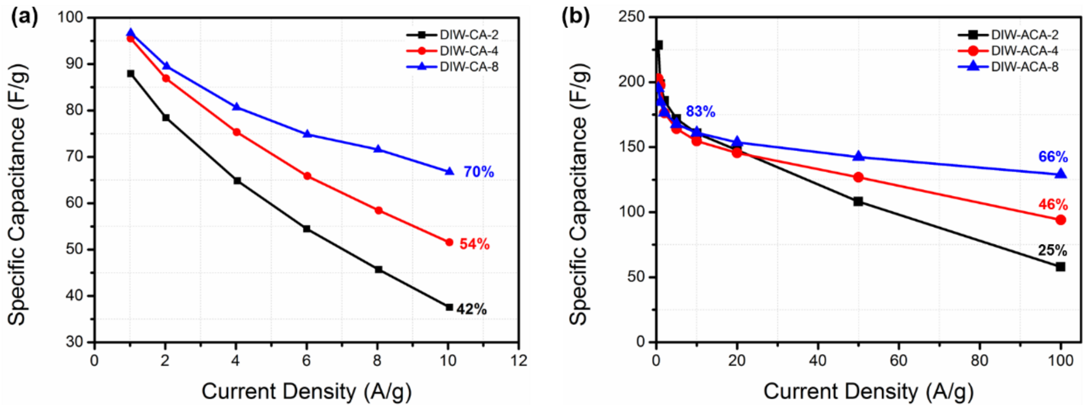

Figure 4.8 Gravimetric capacitance of the (a) DIW-CA-2. DIW-CA-4, DIW-CA-8 and (b) DIW-ACA-2, DIW-ACA-4 and DIW-ACA-8 electrodes obtained at different current densities.

Although these three DIW-CA samples have similar gravimetric capacitances at low current density of 1 A/g, the effect of varying nozzle diameters becomes more significant at the higher current density of 10 A/g. The capacitive retention of the sample printed with 400 µm nozzle is only 42 % and is improved to 70 % when printed with 100 µm nozzle diameter. By varying the filament diameter of the printed electrode, the ion diffusion length is varied and affects the electrochemical performance of these electrodes. After the samples are activated, the DIW-ACA electrodes display more rectangular shapes and increased discharge times, suggesting improved ion diffusion and increased specific surface areas. As observed Fig. 4.8b, both the specific capacitances, volumetric capacitance, and the rate capabilities of DIW-ACA electrodes have further increased compared with the DIW-CA electrodes with the same spacing-to-diameter ratios. For example, the DIW-ACA-8 electrode shows more than twice the specific capacitance of the DIW-CA-8 electrode at 1 A/g. These differences become even more distinct at higher current densities. The DIW-ACA-8 can retain 83 % of its capacitance at 10 A/g (compared to 70 % for DIW-CA-8) and even 66 % at 100 A/g.

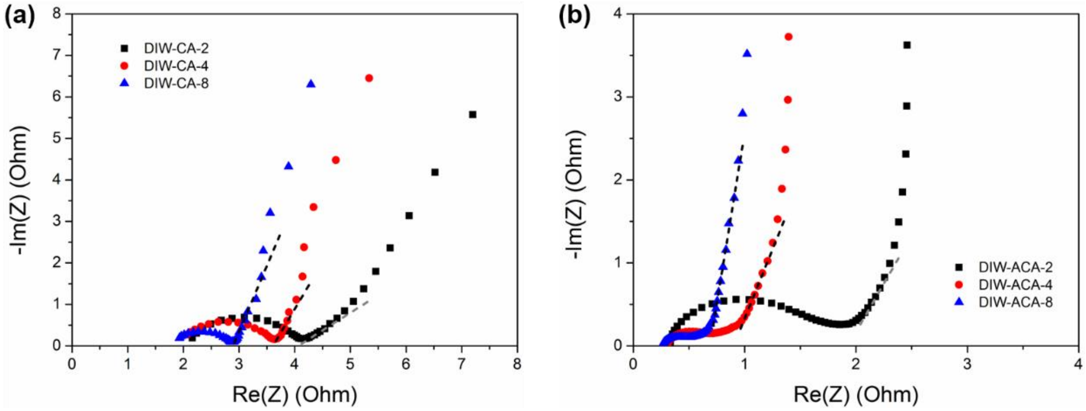

Figure 4.9 Electrochemical impedance spectroscopy of (a) DIW-CA-2. DIW-CA-4, DIW-CA-8 and (b) DIW-ACA-2, DIW-ACA-4 and DIW-ACA-8.

Electrochemical impedance spectroscopy (EIS) was used to gain more insight into the excellent performance of DIW electrodes. As shown in Figure 4.9a, all the DIW-CAs electrodes have similar equivalent series resistance (ESR), which are 2.16, 2.07 and 1.93 ohm for DIW-CA-2, DIW-CA-4 and DIW-CA-8, respectively. The knee frequency is the frequency at which pure capacitance behavior can be obtained and most of its stored energy is accessible at frequencies below this frequency. The knee frequencies of DIW-CA-2, DIW-CA-4 and DIW-CA-8 are 3.85, 18.10 and 25.9 Hz, respectively. The higher the knee frequency represents the less the time is needed for DIW-CA-8 to finish the surface charge accumulation, which is favorable for fast charging and achieving a good rate performance. For the DIW-ACAs electrodes, the ESRs of DIW-ACA-2, DIW-ACA-4 and DIW-ACA-8 are 0.47, 0.31 and 0.26 ohm, respectively (Figure 4.9b). The decreased ESRs of DIW-ACAs electrodes are due to the increased porosity after activation, which is consistent with the previous reports[24-25]. The knee frequencies are 5.48, 56.69 and 90.49 Hz for DIW-ACA-2, DIW-ACA-4 and DIW-ACA-8, respectively. Notably, the considerably higher knee frequencies of the DIW-ACA compared to the DIW-CA electrodes suggests less time is required for the surface charge accumulation at the interface. This improved performance is believed to be due to the improved ion diffusion as a result of the increased porosity after activation and is directly evidenced by the better rate capability.

Previous research has shown that the linear section in the intermediate frequencies (the Warburg region) is associated with ion diffusion resistivity[26-27]. A higher slope in the Warburg region corresponds to the lower diffusion resistivity. As shown in Figure 4.9a and 4.9b, in general the DIW electrodes with higher spacing-to-diameter ratios exhibit lower ion diffusion resistivity compared with the electrode materials with smaller spacing-to-diameter ratios. Importantly, the DIW-ACAs electrodes show improved ion diffusion capability compared to the DIW-CAs at the same spacing-to-diameter ratio, again confirming the additional benefit of activation process.

4.4 Conclusions

In summary, a method to additively manufacture traditional resorcinol-formaldehyde organic aerogels using direct ink writing technology has been demonstrated in this work. The 3D-printed organic aerogel was converted to a carbon aerogel which successfully maintained the engineered microarchitecture of the original organic aerogel print. A critical step for successful 3D printing of the carbon aerogels was the development of a thixotropic, printable sol-gel ink. It was determined that several key features of the microstructure (both macro- and microporosity) can have a profound impact on the electrode performance. Decreasing the minimum feature size from 400 μm to 100 μm also had a significant effect of improving the capacitive retention from 42 % to 70 %, respectively. Lastly, by tuning the surface area of the 3D printed CAs through thermal activation, the specific capacitance of these electrodes was doubled compared to the unactivated electrodes. This resulted in electrodes that exhibited 215 F/g at 1 A/g and an 83% capacitive retention when the current density is increased 10-fold to 10 A/g. Thus, with the possibility to 3D print traditional sol-gel-derived carbon aerogels with engineered macro-pore architecture, future studies will look at the impact of architected porous carbon on other technologies, such as batteries, electrocatalysis and separations.

References

1. R. W. Pekala, C. T. Alviso, *MRS Proc.* **2011**, *270*, 3.
2. C. Moreno-Castilla, F. J. Maldonado-Hodar, *Carbon* **2005**, *43*, 455-465.
3. S. Q. Zhang, J. Wang, J. Shen, Z. S. Deng, Z. Q. Lai, B. Zhou, S. M. Attia, L. Y. Chen, *Nanostruct. Mater.* **1999**, *11*, 375-381.
4. J. Biener, M. Stadermann, M. Suss, M. A. Worsley, M. M. Biener, K. A. Rose, T. F. Baumann, *Energy Environ. Sci.* **2011**, *4*, 656-667.
5. H. Tamon, H. Ishizaka, M. Mikami, M. Okazaki, *Carbon* **1997**, *35*, 791-796.
6. T. F. Baumann, M. A. Worsley, T. Y.-J. Han, J. H. Satcher, Jr., *J. Non-Cryst. Solids* **2008**, *354*, 3513-3515.
7. H. Kabbour, T. F. Baumann, J. H. Satcher, Jr., A. Saulnier, C. C. Ahn, *Chem. Mater.* **2006**, *18*, 6085-6087.
8. M. E. Suss, T. F. Baumann, W. L. Bourcier, C. M. Spadaccini, K. A. Rose, J. G. Santiago, M. Stadermann, *Energy Environ. Sci.* **2012**, *5*, 9511-9519.
9. T. Zhai, X. Lu, H. Wang, G. Wang, T. Mathis, T. Liu, C. Li, Y. Tong, Y. Li, *Nano Lett.* **2015**, *15*, 3189-3194.
10. C. Zhu, T. Liu, F. Qian, W. Chen, S. Chandrasekaran, B. Yao, Y. Song, E. B. Duoss, J. D. Kuntz, C. M. Spadaccini, M. A. Worsley, Y. Li, *Nano Today* **2017**, *15*, 107-120.
11. T. Liu, C. Zhu, T. Kou, M. A. Worsley, F. Qian, C. Condes, E. B. Duoss, C. M. Spadaccini, Y. Li, *ChemNanoMat* **2016**, *2*, 635-641.
12. C. Zhu, T. Y.-J. Han, E. B. Duoss, A. M. Golobic, J. D. Kuntz, C. M. Spadaccini, M. A. Worsley, *Nat. Commun.* **2015**, *6*.

13. J. Bauer, A. Schroer, R. Schwaiger, O. Kraft, *Nat. Mater.* **2016**, *15*, 438-+.

14. J. H. Kim, W. S. Chang, D. Kim, J. R. Yang, J. T. Han, G.-W. Lee, J. T. Kim, S. K. Seol, *Adv. Mater.* **2015**, *27*, 157-161.

15. Y. Lin, F. Liu, G. Casano, R. Bhavsar, I. A. Kinloch, B. Derby, *Adv. Mater.* **2016**, *28*, 7993-8000.

16. Q. Zhang, F. Zhang, S. P. Medarametla, H. Li, C. Zhou, D. Lin, *Small* **2016**, *12*, 1702-1708.

17. C. Zhu, T. Liu, F. Qian, T. Y.-J. Han, E. B. Duoss, J. D. Kuntz, C. M. Spadaccini, M. A. Worsley, Y. Li, *Nano Lett.* **2016**, *16*, 3448-3456.

18. X. Tang, H. Zhou, Z. Cai, D. Cheng, P. He, P. Xie, D. Zhang, T. Fan, *ACS Nano* **2018**, *12*, 3502-3511.

19. Y. Ge, T. Zhang, B. Zhou, H. Wang, Z. Zhang, J. Shen, A. Du, *J. Mater. Res.* **2018**, *33*, 2052-2061.

20. F. Guo, Y. Jiang, Z. Xu, Y. Xiao, B. Fang, Y. Liu, W. Gao, P. Zhao, H. Wang, C. Gao, *Nat. Commun.* **2018**, *9*, 881.

21. Y. Jiang, Z. Xu, T. Huang, Y. Liu, F. Guo, J. Xi, W. Gao, C. Gao, *Adv. Funct. Mater.* **2018**, *28*.

22. B. Fang, Y. Z. Wei, K. Maruyama, M. Kumagai, *J. Appl. Electrochem* **2005**, *35*, 229-233.

23. M. D. Merrill, E. Montalvo, P. G. Campbell, Y. M. Wang, M. Stadermann, T. F. Baumann, J. Biener, M. A. Worsley, *RSC Adv.* **2014**, *4*, 42942-42946.

24. F. Zhang, T. Liu, G. Hou, T. Kou, L. Yue, R. Guan, Y. Li, *Nano Res.* **2016**, *9*, 2875-2888.

25. D. I. Abouelamaiem, G. He, T. P. Neville, D. Patel, S. Ji, R. Wang, I. P. Parkin, A. B. Jorge, M.-M. Titirici, P. R. Shearing, D. J. L. Brett, *Electrochim. Acta* **2018**, *284*, 597-608.

26. X.-L. Wu, Y.-G. Guo, J. Su, J.-W. Xiong, Y.-L. Zhang, L.-J. Wan, *Adv. Energy Mater.* **2013**, *3*, 1155-1160.

27. Y. Song, T. Liu, B. Yao, M. Li, T. Kou, Z.-H. Huang, D.-Y. Feng, F. Wang, Y. Tong, X.-X. Liu, Y. Li, *ACS Energy Lett.* **2017**, *2*, 1752-1759.

28. Y. Hanzawa, K. Kaneko, R. W. Pekala, M. S. Dresselhaus, *Langmuir* **1996**, *12*, 6167-6169.

29. A. Feaver, G. Z. Cao, *Carbon* **2006**, *44*, 590-593.

30. R. Saliger, U. Fischer, C. Herta, J. Fricke, *J. Non-Cryst. Solids* **1998**, *225*, 81-85.

31. C. Lin, J. A. Ritter, *Carbon* **2000**, *38*, 849-861.

32 Gregg S. J., and Sing K. S. W.. *Adsorption, Surface Area and Porosity*.: Academic Press; 1982

33 Rouquerol F., Rouquerol J., Sing K.W.S.. Adsorption by Powders and Porous Solids. Principles, Methodology and Applications, Academic, 1999.

34. P. Yang, W. Mai, *Nano Energy* **2014**, *8*, 274-290.

Chapter 5

3D Printed Five-scale Pore Carbon Aerogels for Supercapacitors at Ultralow Temperatures

Abstract

Achieving sound charging capability at low temperatures represents a major challenge for the energy storage field. Conventional porous carbon electrodes have shown their success for rapid charging at room temperatures. However, their performance deteriorates significantly with the decrease of temperatures due to the sluggish ion and electron transport in the thick electrodes. Herein, by adding another dimension of pore structure in the carbon electrodes *via* 3D printing method, a five-scale pore carbon network has for the first time been fabricated. The 3D printed multiscale porous carbon aerogels with the combination of 3D pores, micron pores, macropores, mesopores and micropores have demonstrated superior capacitance and rate capability than their conventional bulk counterparts. Furthermore, the hierarchical pores in the 3D printed structure have also been proved to be indispensable to achieve the excellent electrochemical performance at the extremely low temperatures. This work advances our understanding of the electrochemical properties and kinetic processes of carbon electrodes at extremely low temperatures, which will inspire the future design on the high-performance low-temperature energy storage devices.

Herein, we have successfully fabricated the 3D-printed multiscale porous carbon aerogels (3D-MCA) with higher surface area *via* direct printing the CNCs-based inks.

The as-synthesized carbon aerogels own hierarchical pore network, with large voids in between 3D-printed ligaments (3D pores), micron-meter size pores by sublimation of ice (micron pores), submicron-meter size pores by removal of SiO_2 microsphere template (macro-pores), and small pores (meso- and micro-pores) *via* the KOH etching on carbon aerogels (**Figure 1a**). Even under extremely low temperature of -70 °C, the 3D-printed carbon aerogels exhibited efficient ion diffusion capability. The 3D-MCA displayed an excellent capacitance of 148.6 F g^{-1} at a scan rate of 5 mV s^{-1} and retained a high capacitance of 71.4 F g^{-1} even at a high scan rate of 200 mV s^{-1}. These are among the best results for ultralow-temperature supercapacitors and are much higher than the capacitance of conventional bulk aerogel electrodes (non-3D-MCA) with 63.8 F g^{-1} at a scan rate of 5 mV s^{-1} and 11 F g^{-1} at a scan rate of 200 mV s^{-1}. Furthermore, the combination of the pores at different scales has been proved to be necessary to achieve the high performance. By eliminating any type of pore, the capacitance reduced significantly due to the increased ion diffusion resistance and charge transfer resistances. This work for *the first time* fabricates 3D printed carbon aerogels with five-scale pores and demonstrates the 3D printed structure with the combination of multiscale pores is essential for the supercapacitors at low temperatures. The findings offer new insights for the design principle of high-performance energy storage devices that can be rapidly charged at ultralow temperatures.

5.1 Introduction

The capability of rapidly store and deliver electricity at ultralow temperatures is critical for the increasing number of space missions and human activities in the polar areas.[1-5] The lowest working temperatures of commercial lithium ion batteries and supercapacitors are typically around -20 ºC to -40 ºC, limited by the freezing of electrolytes.[4] Numerous efforts have been made to improve the low temperature performance of energy storage devices, with a main focus on the development of new electrolytes with improved low temperature properties. For example, mixed solvents and eutectic electrolyte salts were used to increase the solubility and expand the working temperature range.[8-10] Alternatively, energy storage devices can be operated in low temperature environments by incorporating external or self-heating components.[2, 11] Yet, little work has been done to improve the low-temperature device performance by engineering the structural properties of electrodes.[12-13] There are rooms for improvement in respect of electrode capacitance and rate performance.[12, 14-17]

Multiscale pore architectures containing macro-, meso-, and micro-pores have been proven to be effective in improving ion diffusion and rate capability of supercapacitors.[18] The presence of micro-pores can significantly increase the electrode's specific surface area,[18-19] while the macro- and meso-pores serve as electrolyte reservoirs that can shorten the ion diffusion length during fast charging.[20-21] Furthermore, the recently developed 3D printed carbon lattice with aligned pores allows efficient ion diffusion throughout the entire electrode even at large thicknesses. Inspired by these works, we anticipated that a 3D printed lattice structure composed of hierarchical porous carbon ligaments can substantially reduce ion diffusion resistance and distance and, thus, improve the electrode performance at low temperatures.

5.2 Experimental Section

Synthesis of SiO_2 nanospheres:

SiO_2 nanospheres were synthesized via a modified Stöber method. 15.0 mL de-ionized water, 100.0 mL absolute ethanol, and 5.0 mL ammonia solution were mixed together in a 250.0 mL flask by stirring at 500 rpm in 40 °C in a water bath. Then, 6.000 g (6.383 mL) TEOS was added into the mixture and continue stirring for 5 h at 40 °C. The clear solution turned to white after the reaction. The precipitates (SiO_2 nanospheres) were then collected by centrifugation and rinsing with ethanol and de-ionized water until the pH reached around 7.0. The precipitates were then dried in electric oven at 70 °C overnight.

Ink preparation:

1g SiO_2 nanosphere powder was first mixed with 2 mL de-ionized water and sonicated for 2 h in ice water followed by mixing with 1g nanocellulose powder and 2 mL water.

3D Printing:

The ink is loaded into a 5.0-mL syringe barrel (EFD) and centrifuged for two minutes to remove air bubbles. After that, the ink is extruded through a micro nozzle

(200 µm) to print the 3D structures on a silicon wafer substrate. The writing speed was kept around 1.5-2.0 mm/s. Simple lattice structures with multiple orthogonal layers of parallel cylinder rods were printed layer-by-layer. The diameter of the cylinder rods is around the diameter of nozzle and the center-to-center spacing of two parallel rods is 1.00 mm. The height of the electrodes varied from 0.50 mm to 4.00 mm. The spacing in z direction is 0.16 mm. After printing, the samples were put into dry ice immediately to avoid evaporation of water and then transferred to a refrigerator to freeze the samples at -20 °C for 2 h. All the printing was conducted on the Hyrel 30M 3D printer.

Preparation of 3D printed porous carbon aerogel:

After printing, the samples were freeze-dried for 12 h in vacuum to form aerogels using the Labconco Freeze Dryer. The 3D printed cellulose-SiO_2 aerogels were carbonized in a tube furnace at 800 °C for 2 h in nitrogen atmosphere to form 3D printed SiO_2 embedded carbon aerogels. Then the 3D printed carbon aerogels were soaked in 2 M sodium hydroxide (NaOH) aqueous solution at 70 °C for 10 h to dissolve the embedded SiO_2 spheres. The samples were then put in 50 mL de-ionized water at 70 °C to remove any residual NaOH or silicate salts overnight and dried in an electric oven at 70 °C for 2 h. After that, the samples were immersed in 1.0 M KOH aqueous solution for 8 h and then dried in an electric oven at 80 °C for 2 h followed by the annealing in a tube furnace at 800 °C in nitrogen atmosphere for 1 h. After annealing, the sample was immediately washed with de-ionized water to dissolve any soluble impurities. Finally, the samples were rinsed by 0.5 M HCl and ample amount of water until the pH reached 7.0, and then dried in an electric oven at 70 °C for 2 h.

Materials Characterization

The structural properties of the materials were investigated by a field emission SEM (FEI Quanta 3D FEG dual beam) and TEM (FEI Talos F200S). The chemical composition of materials was studied by XPS (ESCALab) and FTIR spectroscopy (Nicolet/Nexus 670), Raman spectroscopy (Renishaw inVia). Textural properties were measured by Brunauer-Emmett-Teller methods using a BELSORP-max-II (Microtrac-BEL, Japan) surface area analyzer via nitrogen porosimetry. The contact angles of electrolyte drop deposited on the surface of carbon aerogels were measured at room temperature using a contact angle meter (SL150, Kino industrial co. LTD, USA).

The electrochemical measurements were conducted on symmetric supercapacitor devices using electrochemical workstations (CHI 660D and BioLogic EC-Lab SP-300). Symmetric supercapacitor based on two pieces of identical carbon aerogels were assembled in a coin cell sandwiching a nanoporous polypropylene membrane separator (Celgard 3501, Celgard LLC). The electrolyte is a mixed solution containing 0.5 M tetraethylammonium tetrafluoroborate ($TEABF_4$) in 1:1 acetonitrile (AN)/methyl formate (MF). An analytical balance (Sitizen Scale, CX265) of a balance with d=0.01 mg was used for the weight measurements. The mass loading of the carbon aerogels is around 4.70 mg cm^{-2}.

Calculations

The gravimetric capacitance (C_G) of single electrodes were calculated based on the galvanostatic charging and discharging curves of symmetric supercapacitors using Equation 1.

$$C_G = \frac{4I \times t}{\Delta U \times m} \text{ (Equation 1)}$$

where C_G is the gravimetric capacitance (F g^{-1}), ΔU is the potential window (V), I is the discharge current (A), t is the discharge time (s), m is the mass loading of the materials on the electrodes (g).

The gravimetric energy density (E, Wh kg^{-1}) and power density (P, W kg^{-1}) of the asymmetric device are calculated using the following equations:

$$E_G = \frac{1000}{2 \times 3600} \frac{C_G}{4} U^2 \text{ (Equation 2)}$$

$$P_G = \frac{3600 \times E_G}{t} \qquad \text{(Equation 3)}$$

Where C_G is the gravimetric capacitance (F g^{-1}), U is the working voltage (V) and t is the discharging time (s) measured in the galvanostatic charging and discharging experiments.

5.3 Results and Discussions

We prepared a 3D-printed multiscale porous carbon aerogels (3D-MCA) with high surface area *via* direct ink writing (DIW) method using cellulose nanocrystals

(CNCs) based inks, as illustrated in Figure 1a. CNCs, derived from plant celluloses, are promising material for 3D printing due to their high abundance in nature and the unique properties in aqueous solution.[33-35] First, the rich hydroxyl groups on cellulose molecule (six in each unit) form strong hydrogen bonding within the cellulose and with water. The cellulose matrix can achieve a high-water retention of 98% in aqueous solution.[36] Second, the extremely negative zeta potential (*ca.* -60 mV) enables nanocellulose work as a surfactant to assist various other materials disperse in aqueous solution.[33] Third, the nanocellulose has a high Young's Modulus of *ca.* 150 GPa, which helps the nanocellulose retain their structure after drying.[37] CNCs has been mainly used as a viscosifier to prepare viscoelastic inks for printing,[22, 24] while there is no report using CNCs as the carbon precursor.

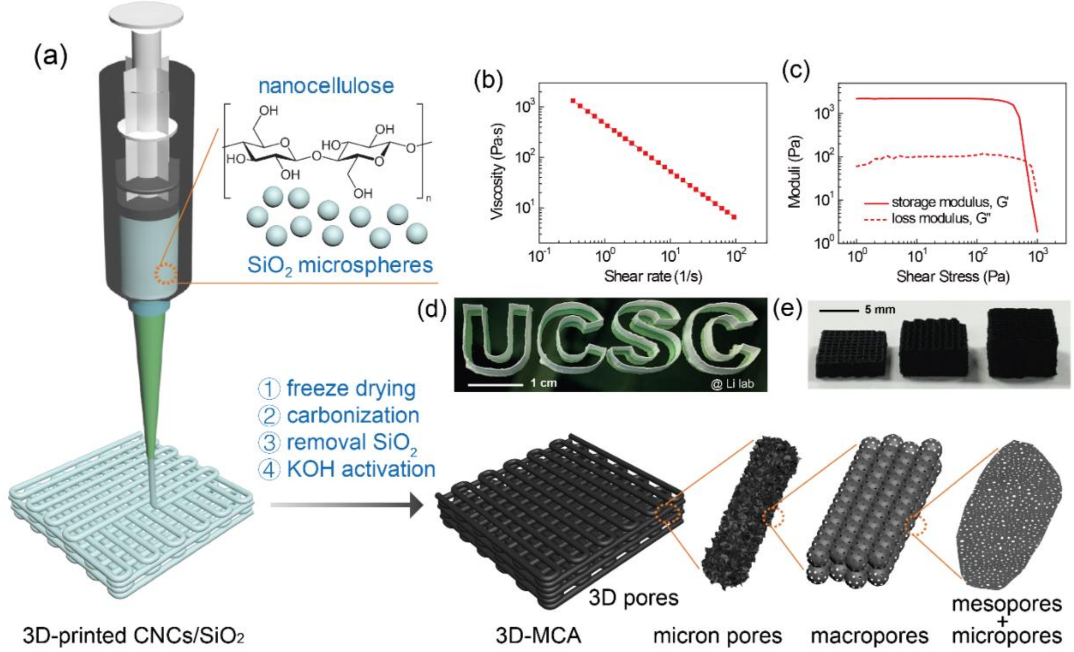

Figure 5.1 (a) Schematic diagram of the fabrication of 3D printed multiscale porous carbon aerogels. (b) Apparent viscosity as a function of shear rate, and (c) the storage modulus (G’) and loss modulus (G”) as a function of shear stress for CNCs/SiO_2 ink. (d) Digital image of the 3D printed CNCs/SiO_2 aerogels with a shape of “UCSC”. (e) Digital image of the 3D-printed multiscale porous carbon aerogels with different thickness.

Here we combine CNCs with silica microsphere suspension to form a homogenous and highly viscous ink, where CNCs is the carbon precursor and silica serves as a hard template for creating macropores. The CNCs ink showed shear-thinning non-Newtonian fluid property. With the increase of shear rates, viscosity is decreasing (Figure 1b). The ink’s viscoelastic fingerprints display predominantly solid-like behavior with a high storage modulus under small shear stresses (Figure 1c). It becomes liquid-like under high shear stress, which enables the continuous extrusion through micro-meter-sized nozzles. The ink is extruded from the syringe with micronozzle to create 3D structures. Complex configurations and structures with different thicknesses can be 3D-printed directly in air with well-retained shapes (Figure 1d and 1e). Multiscale pore structures were generated after carbonization the freeze-dried printed lattices, followed by the removal of the silica template and KOH activation, using a method reported elsewhere. This 3D-printed multiscale porous carbon aerogels is denoted as 3D-MCA. The top-view and cross-sectional SEM images obtained from the carbon aerogel clearly showed the periodic pore channels in the layer-by-layer woodpile structure (Figure 2a and 2b). These pores (denoted as 3D pores) are around 500 μm in diameter, which is defined by the center-to-center distance of carbon ligaments. The open structure ensures the efficient electrolyte infiltration and diffusion even in thick electrodes. Higher magnification SEM image collected from individual carbon ligaments prove that they are porous in nature with micron size pores (*ca.* 5-50 μm) distributed in each ligament (Figure 2c and 2d). These pores were generated by the sublimation of ice during the freeze-drying process. The presence of these pores facilitates the diffusion of electrolyte ions within ligaments. The carbon flakes in each ligament are composed of the interconnected hollow carbon spheres (Figure 2e), which were obtained after the removal of silica microsphere templates. The resultant macropores (*ca.* 300 nm) in these hollow structures could work as electrolyte reservoir to achieve rapid charge accumulation during fast charging. KOH activation was used to create small pores and therefore boost the electrode surface area. An increased I_D/I_G ratio in the Raman spectra disclose that more defects were introduced into the carbon aerogels after KOH activation, which is consistent with previous reports.[18, 38] Transmission electron microscopy (TEM) images together with Brunauer-Emmett-Teller (BET) measurements further revealed that the hollow spheres contain mesopores and micropores (Figure 2f). The thickness of the hollow spheres are at nanometer scale, which is equivalent to only several layers of carbon atoms. The selected area electron diffraction (SAED) pattern showed that 3D-MCA is amorphous in nature. (Figure 2f). Comparing the nitrogen adsorption-desorption isotherms of 3D-CA and 3D-MCA, it is clear that 3D-MCA has significantly higher absorbed nitrogen volume than 3D-CA, indicating the increased specific surface area after KOH activation (Figure 2g).

The steep increase in the absorbed nitrogen at both low relative pressure ($P/P_0<0.1$) and high relative pressure ($P/P_0>0.9$) suggest the existence of the large amount of micropores and macropores, respectively. The hysteresis located at $0.4<P/P_0<1.0$ indicates the presence of mesopores.[18] The pore size distribution profile (Figure 2h) confirmed the observation in the nitrogen absorption-desorption isotherms, with micropores centered at 1.93 nm and mesopores centered at 4.28 nm. Significantly, 3D-MCA exhibits a BET surface area of 1749.7 m^2 g^{-1}, which is considerably larger than that of 3D-CA (322.8 m^2 g^{-1}) (Figure S4) and most other 3D-printed carbon-based supercapacitor electrodes, such as 3D printed macroporous graphene (27 m^2 g^{-1}), 3D printed graphene aerogel (87 m^2 g^{-1}), 3D printed graphene/CNT (222 m^2 g^{-1}) and 3D printed graphene foam (994.2 m^2 g^{-1}).[24-25, 32, 40]

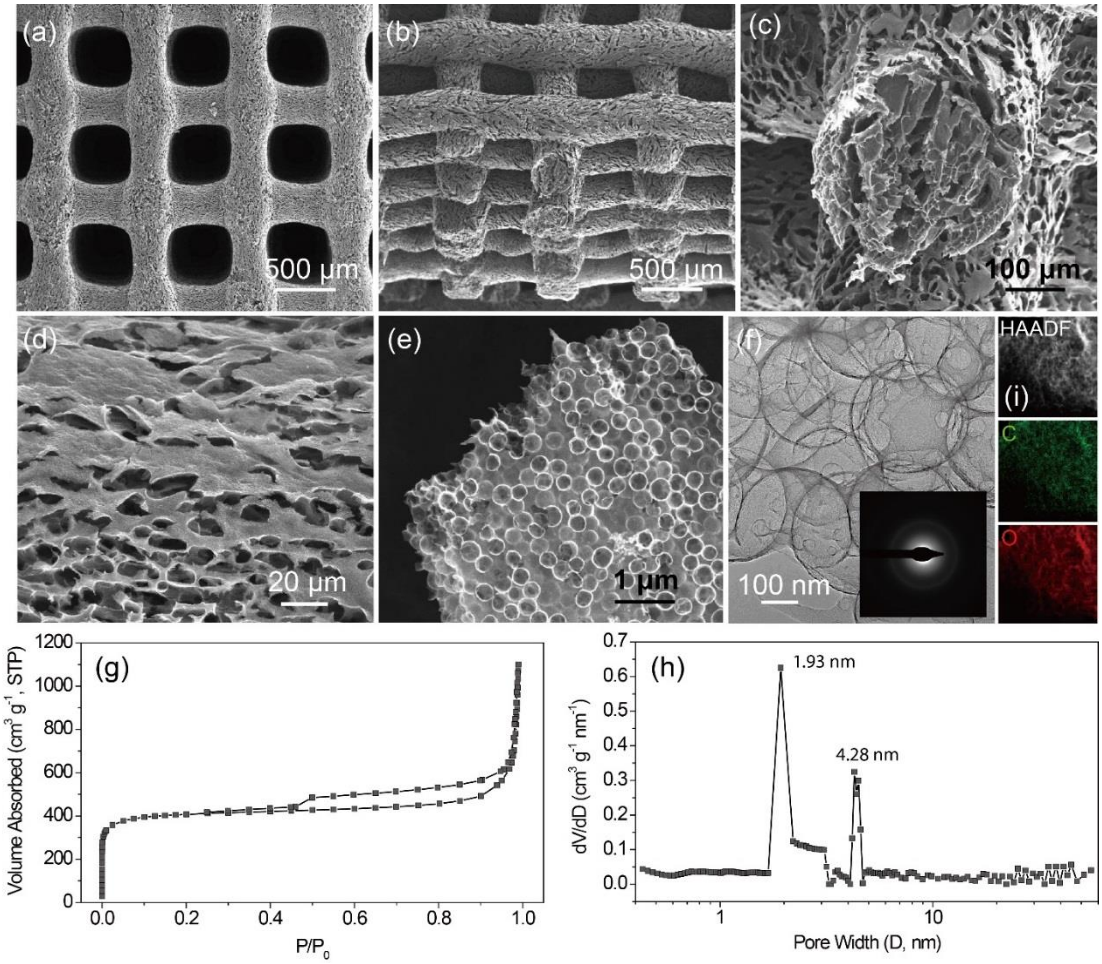

Figure 2. (a) Top-view, and (b) cross-sectional SEM images of 3D-MCA. (c) Cross-sectional SEM image of an individual carbon ligament of 3D-MCA. (d) SEM image collected from the ligament surface. (e) SEM image, and (f) TEM image collected at the edge of a piece of carbon flake. Inset in Figure 1f shows the corresponding SAED pattern. (g) Nitrogen absorption-desorption isotherms, and (h) Pore size distribution of 3D-MCA. (i) HAADF-STEM image of a carbon flake and its corresponding mapping image of element C and O.

The X-ray photoelectron spectroscopy (XPS) spectrum of 3D-MCA exhibit strong carbon and oxygen signals, suggesting the carbon surface contains some oxygen functionalities. It is consistent with the TEM elemental mapping results (Figure 2i). These oxygen moieties make 3D-MCA surface highly hydrophilic that is favorable for electrolyte penetration. The dynamic contact angle measurements showed that an electrolyte droplet was completely absorbed by 3D-MCA within half a second.

The engineered multiscale pore network, high surface area and superior electrolyte wetting of the 3D-MCA make it a promising electrode for supercapacitors, especially at low temperatures, where the ion diffusive properties becoming even more important. The low temperature performance of 3D-MCA electrodes were tested in a homebuilt bath cooling system. Absolute ethanol and water were first mixed in a mass ratio of 4:1.[41] Then dry ice was slowly added into the mixed solution until the temperature stabilized at -70 ºC. The temperature can be maintained for an extended period of time by continuously adding dry ice. Temperatures between 0 to -118 ºC can be obtained by tuning the ratio between ethanol and water. A mixed solvent electrolyte contains 0.5 M tetraethylammonium tetrafluoroborate ($TEABF_4$) in a 1:1 acetonitrile (AN)/methyl formate (MF) was used for the electrochemical measurements. The ultralow freezing point of MF extends the freezing point of the electrolyte below -70 ºC, while the higher dielectric constant of AN enables the high solubility of $TEABF_4$ in the electrolyte.[8]

Symmetric supercapacitors were fabricated via the assembly of two 3D-MCA electrodes . We also fabricated a control device using bulk multiscale porous carbon aerogel without 3D pores (MCA) as electrodes. MCA exhibits similar microstructure and textural property as 3D-MCA (Figure S10-S11). Temperature-dependent capacitive measurements were performed for both samples to tested our hypothesis that the incorporation of 3D pores is critical in enhancing the ion diffusion and, therefore, the device's performance at low temperatures. As shown in Figure 3a, 3D-MCA exhibits a quasi-rectangular shape cyclic voltammogram even at -70 ºC. The 3D-MCA electrode achieved a gravimetric capacitance of 148.6 F g^{-1} at a scan rate of 5 mV s^{-1}, which is considerably higher than that of MCA (63.8 F g^{-1}). It also outperforms many other previously reported carbon electrodes at similar or even higher temperatures, such as graphene films (60 F g^{-1} at 1 mV s^{-1}, -40 ºC), activated graphene (100 F g^{-1} at 1 mV s^{-1}, -50 ºC), activated carbon (92 F g^{-1} at 5 A g^{-1}, -60 ºC), mesoporous graphene (20 F g^{-1} at 1 A g^{-1}, -70 ºC), carbon nanotubes (53.4 F g^{-1} at 100 mV s^{-1}, -70 ºC), and zeolite-templated carbon (117 F g^{-1} at 1 mV s^{-1}, -70 ºC).[12, 14-15, 42-44] Most importantly, 3D-MCA electrode retained 48% of its capacitance when the scan rate increased from 5 to 200 mV s^{-1}, while MCA has a retention rate of 11% only (Figure 3b). The better capacitance retention rate is believed to be related to the open structure of 3D-MCA that preserves a good level of ion diffusion efficiency even at low temperature. At room temperature (20 ºC), the capacitance ratio of 3D-MCA to MCA is around 2.4 at a scan rate of 5 mV s^{-1}, and the ratio just slightly increased to 2.63 at a high scan rate of 200 mV s^{-1}. It indicates that the role of 3D porous channels is insignificant when the ion diffusion into the electrode is enough efficient at 20 ºC. In contrast, at -70 ºC, while the capacitance ratio is still around 2.33 at a slow scan rate of 5 mV s^{-1}, the ratio rapidly increase to 6.5 at a high scan rate of 200 mV s^{-1}. The results clearly showed that 3D-MCA performs significantly better than MCA at higher charging rates and ultralow temperature.

Kinetic analysis was further performed to understand the different electrochemical behaviors of 3D-MCA and MCA electrodes at ultralow temperatures. The CV curves of the 3D-MCA at different scan rates all display box-like shapes (Figure 3d), indicating the efficient ion diffusion and electron transport property, while the MCA shows more distorted CV shapes. The current i scales with the scan rate following the equation: $i = kv^b$.45-46 The value of b provides information about the charge storage kinetics. b=1 represents an ideal capacitive behavior, while b=0.5 suggests a diffusion-controlled process.[46] By plotting the logarithm of the absolute current density against the logarithm of scan rate ($\log i = b \log v + k$), b values can be calculated from the slopes (Figure 3e). The b values of 3D-MCA (Figure 3f) are much higher than the MCA (Figure S13) at the same voltages. As the temperature decrease from 20 ºC to -70 ºC, the b values of the 3D-MCA decrease considerably slower than that of MCA (Figure 3g). The 3D-MCA retains an excellent b value of 0.88 at -70 ºC suggests that the 3D printed open porous structure successfully retained efficient ion diffusion in the electrode.

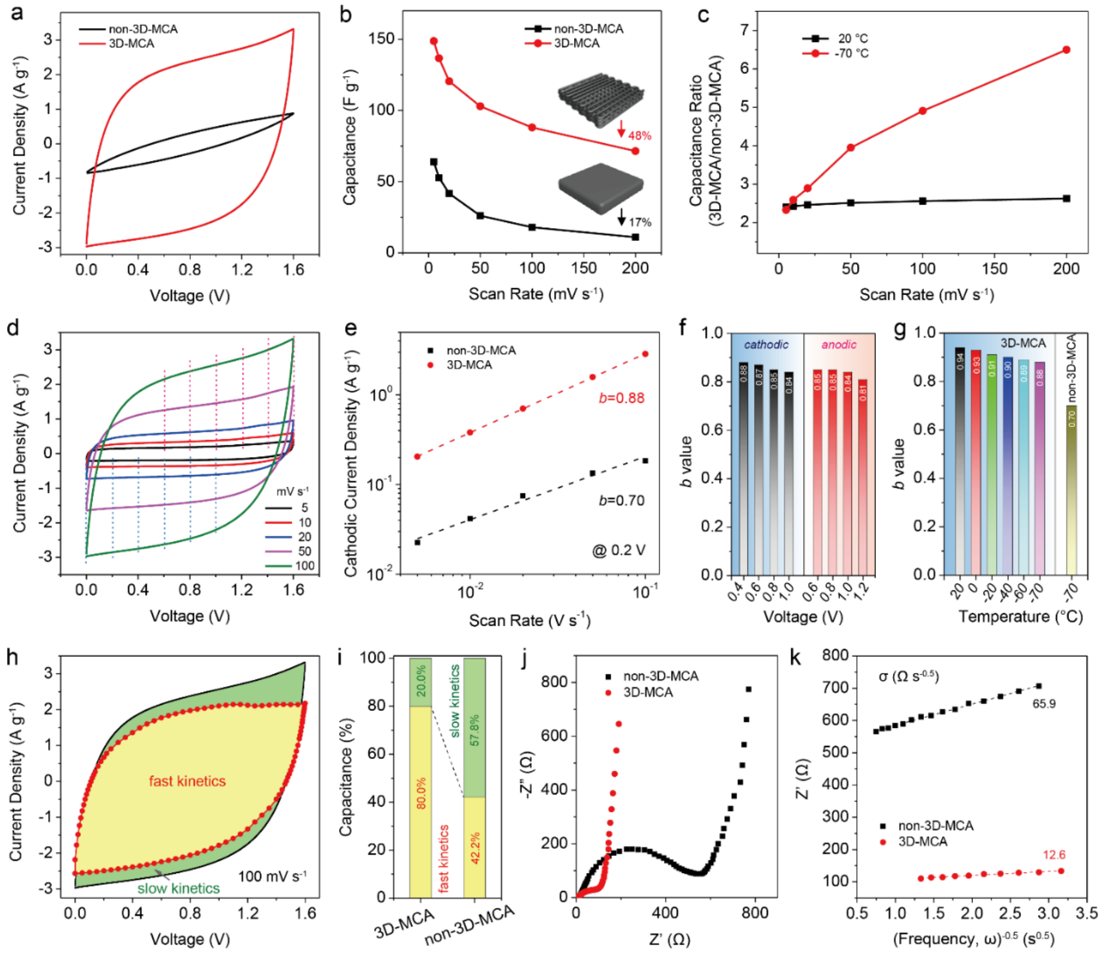

Figure 5.3 (a) Cyclic voltammetry (CV) curves of MCA and 3D-MCA collected at a scan rate of 100 mV s^{-1} at -70 ºC. (b) Gravimetric capacitance of MCA and 3D-MCA obtained at -70 ºC. (c) Capacitance ratio of the 3D-MCA and MCA obtained at 20 ºC and -70 ºC. (d) CV curves of 3D-MCA collected at various scan rates at -70 ºC. Dashed lines highlight the voltages selected for calculating the *b* value. (e) Cathodic current densities of 3D-MCA and MCA obtained at 0.2 V are plotted as a function of scan rate. Dashed lines are the linear fitting lines. (f) A histogram shows the *b* values of 3D-MCA calculated from cathodic currents (left) and anodic currents (right)

obtained at different voltages. (g) A histogram shows the *b* values of the 3D-MCA and MCA at different temperatures. (h) A cyclic voltammogram of 3D-MCA obtained at 100 mV s^{-1} showing the capacitance contribution from the fast-kinetic processes (yellow) and slow-kinetic processes (green). (i) A histogram shows the capacitance contributions by the fast and slow kinetic processes in the 3D-MCA and MCA. (j) Nyquist plots and (k) Z' versus the reciprocal of the square root of frequency in the intermediate frequency range of the 3D-MCA and MCA. Dashed lines are the best fitting lines to calculate the ion diffusion resistance, σ.

We further investigated and compare the capacitance contribution from the fast kinetic and slow kinetic processes in 3D-MCA and MCA.[46-47] The fast kinetics refers to the formation of electric double layer and the charge-transfer processes of surface species, which are not limited by the ion diffusion.[45, 48] The slow kinetics is a result of ion insertion process, which is controlled by the ion diffusion. Figure 3h shows the capacitance contribution from fast-kinetic processes and slow-kinetic process in a cyclic voltammogram of 3D-MCA collected at 100 mV s^{-1}. The current contribution from fast-kinetic processes is dominant among all the voltages with a total contribution of 80%, demonstrating excellent ion accessibility even at -70 ºC (Figure 3i). In contrast, the fast-kinetic contribution for MCA is only 42.2 % under the same conditions. Furthermore, we compared the ion diffusion resistances (σ) of the 3D-MCA and MCA obtained at the same conditions (Figure 3j). The values of σ were extracted from the slope of linear fitting lines of the real part of the impedance (Z') versus the reciprocal of the square root of frequency ($\omega^{0.5}$) (Figure 3k). The 3D-

MCA exhibits a small σ of 12.6 Ω $s^{-0.5}$, which is considerably smaller than that of MCA (65.9 Ω $s^{-0.5}$). The small σ of 3D-MCA at -70 ºC is even comparable to those of other electrodes obtained at room temperature.[21, 49-50] The open channel structure in 3D-printed electrodes also help to shorten the charge transport pathway in the thick electrodes and result in a much smaller charge transfer resistance. The MCA showed a high charge transfer resistance (R_{ct}) of 538 Ω at -70 ºC, while the 3D-MCA displayed a much smaller R_{ct} of 114 Ω. Taken together, these results unambiguously illustrate the critical role of the 3D-printed periodic open porous structure in facilitating the ion accessibility and electron transport at the ultralow temperature.

To study the role of pores on the capacitive performance in the 3D printed carbon aerogels, we prepared three control samples by partially changing the synthetic procedures. The three control samples are denoted as 3D-CA-1, 3D-CA-2 and 3D-CA-3. 3D-CA-1 is a piece of 3D printed carbon aerogel with 3D pores, micron pores, mesopores and micropores, only without macropores. It was fabricated by removing the freeze-drying step. 3D-CA-2 is a piece of 3D printed carbon aerogel with 3D pores, micron pores, macropores, but without mesopores and micropores. It was fabricated without the KOH activation process. 3D-CA-3 is a piece of 3D printed carbon aerogel with 3D pores, micropores, mesopores and micropores, only without macropores. It was fabricated without the use of SiO_2 hard templates.

Figure 4a compares the capacitance of these control samples with 3D-MCA at scan rates from 5 to 100 mV s^{-1}. It is clear that eliminating any type of pores results in significant reduction of the capacitance. EIS spectra and ion diffusion resistances further revealed the internal resistances of these active materials are similar, while the charge transfer resistance and ion diffusion resistance increased significantly (Figure 4b and 4c). The charge transfer resistance of the 3D-MCA at -70 ºC is 114 Ω, which is much smaller than the 196 Ω, 489 Ω and 364 Ω for 3D CA-1, 3D CA-2 and 3D CA-3, respectively. Moreover, the ion diffusion resistance of the 3D-MCA (12.6 $\Omega\ s^{-0.5}$) is also significantly smaller than the 21.5, 129.3 and 113.3 $\Omega\ s^{-0.5}$ for 3D CA-1, 3D CA-2 and 3D CA-3, respectively. This confirms the combination of multiscale pores and 3D printed structure is indispensable to achieve the superior capacitive performance of 3D printed carbon aerogel. To further illustrate the function of each type of pore, we evaluated their imaginary capacitances (C”) as a function of frequency and compared to the C” of the 3D-MCA. It can be found that the control samples without any type of pore exhibit much smaller capacitance in the entire frequency range from 0.01 to 100 Hz (Figure 4d-4f). Those results further confirm the conclusion that the simultaneous presence of 3D printed large pore channels and the hierarchical pores (macron pores, macropores, mesopores and micropores) plays a critical role in the efficient energy storage at low temperatures.

Bin: After some thinking, I am a bit loss about the focus of this work. The studies on macro, meso and micropores concluded that all of them are critical in energy storage at low temperatures. Then why do we use 80% of the manuscript content to talk about the importance of 3D printed porous channels. I feel this last paragraph may confuse reviewers and readers. I would suggest deleting this entire part. The focus of this work in my opinion is to prove our hypothesis that 3D printed lattice structure with aligned pores can improve the electrode performance at ultralow temperature.

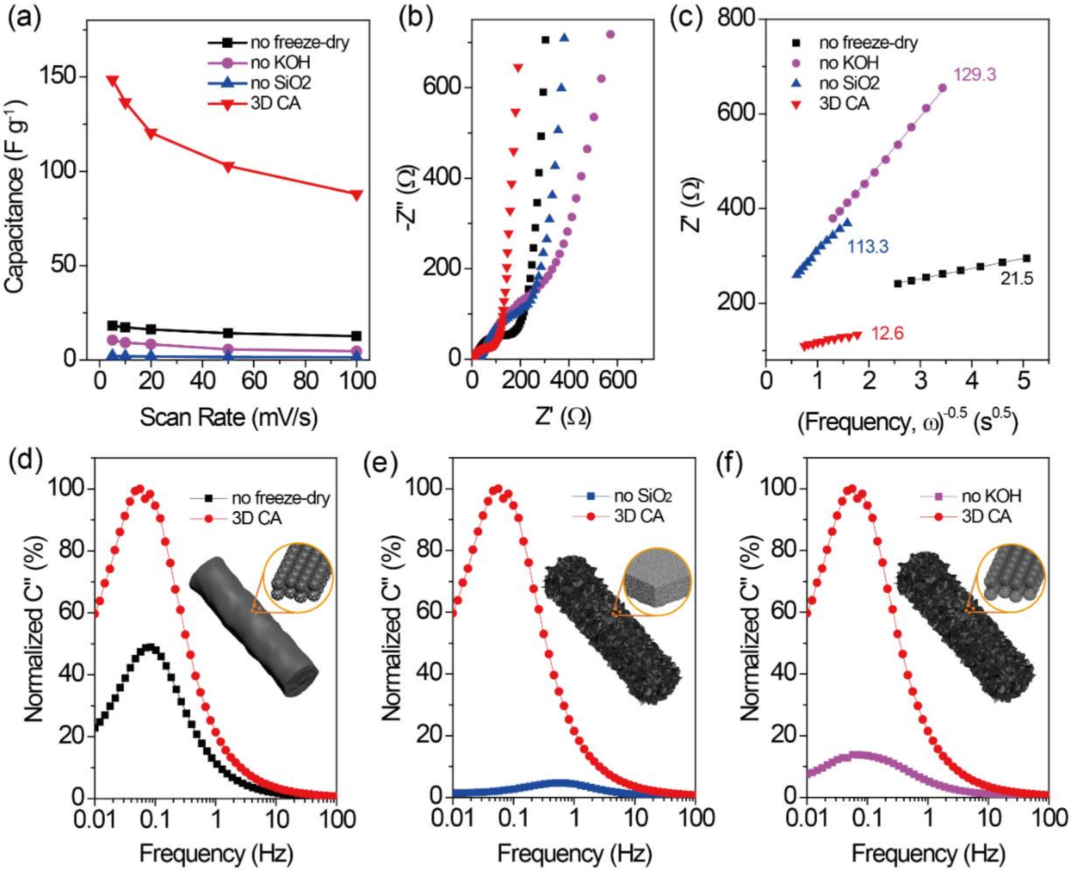

Figure 4. (a) Gravimetric capacitance, (b) EIS spectra, (c) Z' as a function of the reciprocal of the square root of frequency in the intermediate frequency range of the 3D-MCA, 3D-CA-1, 3D-CA-2, and 3D-CA-3 at -70 ºC, respectively. (d-f) Role of pores on capacitance and rate capability of 3D-printed carbon aerogels. Plot of normalized C" (normalized to the maximum C") as a function of frequency for 3D-CA-1, 3D-CA-2, and 3D-CA-3 at -70 ºC, respectively. Insets are the corresponding schematic illustrations of their structural characteristics.

5.4 Conclusions

In summary, for the first time 3D printed carbon aerogels with tunable five-scale pore network *via* low-cost CNCs inks have been successfully fabricated. The 3D printed carbon aerogels exhibited much higher capacitance than the non-3D printed bulk counterpart at an ultralow temperature of -70 ºC. Furthermore, the combination of 3D printed structure with micron pores, macropores, mesopores and micropores in the 3D printed lattices have enabled their excellent capacitive performance at ultralow temperatures. The 3D-MCA displayed a high capacitance of 148.6 F g^{-1} at a scan rate of 5 mV s^{-1} and retained a high capacitance of 71.4 F g^{-1} at a high scan rate of 200 mV s^{-1}, which are among the best results for supercapacitors at ultralow temperatures. More importantly, this work for the first time demonstrates the essential role of 3D printed structure and the presence of multiscale pore network to achieve outstanding performance for electrochemical energy storage devices at ultralow temperatures, which may inspire the further work on the design and construction of high-performance energy storage systems.

References

1 M.-T. F. Rodrigues, G. Babu, H. Gullapalli, K. Kalaga, F. N. Sayed, K. Kato, J. Joyner, P. M. Ajayan, *Nat. Energy* **2017**, *2*, 17108.

2 C.-Y. Wang, G. Zhang, S. Ge, T. Xu, Y. Ji, X.-G. Yang, Y. Leng, *Nature* **2016**, *529*, 515.

3 X. Fan, X. Ji, L. Chen, J. Chen, T. Deng, F. Han, J. Yue, N. Piao, R. Wang, X. Zhou, X. Xiao, L. Chen, C. Wang, *Nat. Energy* **2019**, *4*, 882-890.

4 X. Dong, Z. Guo, Z. Guo, Y. Wang, Y. Xia, *Joule* **2018**, *2*, 902-913.

5 E. Pomerantseva, F. Bonaccorso, X. Feng, Y. Cui, Y. Gogotsi, *Science* **2019**, *366*, eaan8285.

6 L. Hall, *2015 NASA Technology Roadmap* **2015**.

7 D. Miranda, *2020 NASA Technology Taxonomy* **2019**.

8 E. J. Brandon, W. C. West, M. C. Smart, L. D. Whitcanack, G. A. Plett, *J. Power Sources* **2007**, *170*, 225-232.

9 J. Xu, X. Wang, N. Yuan, J. Ding, S. Qin, J. M. Razal, X. Wang, S. Ge, Y. Gogotsi, *Energy Storage Mater.* **2019**.

10 M. C. Smart, B. L. Lucht, S. Dalavi, F. C. Krause, B. V. Ratnakumar, *J. Electrochem. Soc.* **2012**, *159*, A739-A751.

11 Y. Ji, C. Y. Wang, *Electrochimica Acta* **2013**, *107*, 664-674.

12 Y. Korenblit, A. Kajdos, W. C. West, M. C. Smart, E. J. Brandon, A. Kvit, J. Jagiello, G. Yushin, *Adv Funct Mater* **2012**, *22*, 1655-1662.

13 J. Xu, N. Yuan, J. M. Razal, Y. Zheng, X. Zhou, J. Ding, K. Cho, S. Ge, R. Zhang, Y. Gogotsi, R. H. Baughman, *Energy Storage Mater.* **2019**, *22*, 323-329.

14 W.-Y. Tsai, R. Lin, S. Murali, L. Li Zhang, J. K. McDonough, R. S. Ruoff, P.-L. Taberna, Y. Gogotsi, P. Simon, *Nano Energy* **2013**, *2*, 403-411.

15 J. Tian, C. Cui, Q. Xie, W. Qian, C. Xue, Y. Miao, Y. Jin, G. Zhang, B. Guo, *J. Mater. Chem. A* **2018**, *6*, 3593-3601.

16 Q. Abbas, F. Béguin, *ChemSusChem* **2018**, *11*, 975-984.

17 Z. Wang, J. Cheng, J. Zhou, J. Zhang, H. Huang, J. Yang, Y. Li, B. Wang, *Nano Energy* **2018**, *50*, 106-117.

18 F. Zhang, T. Liu, M. Li, M. Yu, Y. Luo, Y. Tong, Y. Li, *Nano Lett.* **2017**, *17*, 3097-3104.

19 T. Y. Liu, F. Zhang, Y. Song, Y. Li, *J. Mater. Chem. A* **2017**, *5*, 17705-17733.

20 Z. Zhou, T. Liu, A. U. Khan, G. Liu, *Sci. Adv.* **2019**, *5*, eaau6852.

21 T. Liu, Z. Zhou, Y. Guo, D. Guo, G. Liu, *Nat. Commun.* **2019**, *10*, 675.

22 S. Chandrasekaran, B. Yao, T. Liu, W. Xiao, Y. Song, F. Qian, C. Zhu, E. B. Duoss, C. M. Spadaccini, Y. Li, M. A. Worsley, *Mater. Horiz.* **2018**, *5*, 1166-1175.

23 C. Zhu, T. Liu, F. Qian, T. Han, E. Duoss, J. Kuntz, C. Spadaccini, M. Worsley, Y. Li, *Nano Lett.* **2016**, *16*, 3448-3456.

24 B. Yao, S. Chandrasekaran, J. Zhang, W. Xiao, F. Qian, C. Zhu, E. B. Duoss, C. M. Spadaccini, M. A. Worsley, Y. Li, *Joule* **2019**, *3*, 459-470.

25 X. Tang, H. Zhou, Z. Cai, D. Cheng, P. He, P. Xie, D. Zhang, T. Fan, *ACS Nano* **2018**, *12*, 3502-3511.

26 W. Yang, J. Yang, J. J. Byun, F. P. Moissinac, J. Xu, S. J. Haigh, M. Domingos, M. A. Bissett, R. A. W. Dryfe, S. Barg, *Adv. Mater.* **2019**, *31*, e1902725.

27 M. A. Skylar-Scott, J. Mueller, C. W. Visser, J. A. Lewis, *Nature* **2019**, *575*, 330-335.

28 D. A. Walker, J. L. Hedrick, C. A. Mirkin, *Science* **2019**, *366*, 360-364.

29 G. Hu, J. Kang, L. W. T. Ng, X. Zhu, R. C. T. Howe, C. G. Jones, M. C. Hersam, T. Hasan, *Chem. Soc. Rev.* **2018**, *47*, 3265-3300.

30 K. Fu, Y. Yao, J. Dai, L. Hu, *Adv. Mater.* **2017**, *29*, 1603486-1603505.

31 C. Zhu, T. Y. Liu, F. Qian, W. Chen, S. Chandrasekaran, B. Yao, Y. Song, E. B. Duoss, J. D. Kuntz, C. M. Spadaccini, M. A. Worsley, Y. Li, *Nano Today* **2017**, *15*, 107-120.

32 C. Zhu, T. Y. Han, E. B. Duoss, A. M. Golobic, J. D. Kuntz, C. M. Spadaccini, M. A. Worsley, *Nat. Commun.* **2015**, *6*, 6962.

33 D. Cao, Y. Xing, K. Tantratian, X. Wang, Y. Ma, A. Mukhopadhyay, Z. Cheng, Q. Zhang, Y. Jiao, L. Chen, H. Zhu, *Adv. Mater.* **2019**, *31*, 1807313.

34 B. Thomas, M. C. Raj, A. K. B, R. M. H, J. Joy, A. Moores, G. L. Drisko, C. Sanchez, *Chem. Rev.* **2018**, *118*, 11575-11625.

35 W. Chen, H. Yu, S.-Y. Lee, T. Wei, J. Li, Z. Fan, *Chem. Soc. Rev.* **2018**, *47*, 2837-2872.

36 H. Zhu, W. Luo, P. N. Ciesielski, Z. Fang, J. Y. Zhu, G. Henriksson, M. E. Himmel, L. Hu, *Chem. Rev.* **2016**, *116*, 9305-9374.

37 S. Iwamoto, W. Kai, A. Isogai, T. Iwata, *Biomacromolecules* **2009**, *10*, 2571-2576.

38 Y. Zhu, S. Murali, M. D. Stoller, K. J. Ganesh, W. Cai, P. J. Ferreira, A. Pirkle, R. M. Wallace, K. A. Cychosz, M. Thommes, D. Su, E. A. Stach, R. S. Ruoff, *Science* **2011**, *332*, 1537-1541.

39 J. C. Wang, S. Kaskel, *J. Mater. Chem.* **2012**, *22*, 23710-23725.

40 X. Xu, C. Guan, L. Xu, Y. H. Tan, D. Zhang, Y. Wang, H. Zhang, D. J. Blackwood, J. Wang, M. Li, J. Ding, *ACS Nano* **2019**.

41 E. W. Flick, *Industrial solvents handbook*, **1998**.

42 Z. Lin, P.-L. Taberna, P. Simon, *Electrochimica Acta* **2016**, *206*, 446-451.

43 F. Cheng, X. Yu, J. Wang, Z. Shi, C. Wu, *Electrochimica Acta* **2016**, *200*, 106-114.

44 Y. Gao, Z. Qin, L. Guan, X. Wang, G. Z. Chen, *Chemical Communications* **2015**, *51*, 10819-10822.

45 J. Wang, J. Polleux, J. Lim, B. Dunn, *J. Phys. Chem. C* **2007**, *111*, 14925-14931.

46 H. S. Kim, J. B. Cook, H. Lin, J. S. Ko, S. H. Tolbert, V. Ozolins, B. Dunn, *Nat. Mater.* **2017**, *16*, 454-460.

47 Z. H. Huang, Y. Song, D. Y. Feng, Z. Sun, X. Sun, X. X. Liu, *ACS Nano* **2018**, *12*, 3557-3567.

48 H. Lindström, S. Södergren, A. Solbrand, H. Rensmo, J. Hjelm, A. Hagfeldt, S.-E. Lindquist, *J. Phys. Chem. B* **1997**, *101*, 7717-7722.

49 B. Yao, M. Li, J. Zhang, L. Zhang, Y. Song, W. Xiao, A. Cruz, Y. Tong, Y. Li, *Nano-Micro Lett.* **2019**, *12*, 3.

50 J. Zhou, X. Liu, W. Cai, Y. Zhu, J. Liang, K. Zhang, Y. Lan, Z. Jiang, G. Wang, Y. Qian, *Adv. Mater.* **2017**, *29*, 1700214.

Chapter 6

Efficient 3D Printed Pseudocapacitive Electrodes with Ultrahigh MnO_2 Loading

Abstract

Retaining sound electrochemical performance of electrodes at high mass loading holds significant importance to energy storage. Pseudocapacitive materials such as manganese oxide (MnO_2) deposited on current collectors have achieved outstanding gravimetric capacitances sometimes even close to their theoretical values. Yet, this is only achievable with very small mass loading of active material typically less than 1.0 mg cm^{-2}. Increasing mass loading often leads to drastic decay of capacitive performance due to sluggish ion diffusion in bulk material. Here, we demonstrate a 3D printed graphene aerogel structure that can support MnO_2 to hundreds mg/cm^2 level without sacrificing their performance. Moreover, this 3D printed graphene aerogel/MnO_2 electrode can simultaneously achieve excellent capacitance normalized to area, gravimetry and volume, which is the trade-off for most electrodes. This work successfully validates the feasibility of printing practical pseudocapacitive electrodes, which might revolutionize the way of fabricating pseudocapacitors.

6.1 Introduction

Pseudocapacitors are an important class of energy storage devices that could balance the need of high energy density and fast charging/discharging.[1-6] Among many pseudocapacitive materials, manganese oxide (MnO_2) stands out for its high theoretical specific capacitance, wide availability and environmental friendliness.[7, 8]

Since the pioneering study of MnO_2 by Goodenough *et al.* in 1999, various strategies have been employed to improve the capacitive performance of MnO_2, including crystallinity engineering, crystal structure selection, morphology control, defect introduction and elemental doping.[9-14] Excellent specific capacitance (150-600 F g^{-1}) were obtained from electrodes with small mass loadings of MnO_2 (0.1-0.8 mg cm^{-2}). However, increasing MnO_2 loading often causes severe deterioration of capacitive performance due to inefficient electron transport and ion diffusion.[15-17] Deposition of MnO_2 nanomaterials onto conductive and high surface area current collectors have proven to be an effective way to improve electron transport,[8] they are less effective in addressing the sluggish ion diffusion in thick MnO_2 film, especially for thick electrodes. Therefore, developing a current collector that simultaneously enables efficient electron transport and ion diffusion is particularly important for realizing practical feasible pseudocapacitors.

The advance in 3D printing techniques offers new possibilities in addressing this outstanding challenge for pseudocapacitors. In a recent study, a 3D printed carbon electrode showed considerably improved rate capability compared its bulk counterpart.[18] The enhancement was believed to be due to periodic macropores, which facilitate the diffusion of electrolyte ions, and thus, improve the electric double layer capacitance at high current densities. Significantly, the findings also suggested that the 3D printed carbon aerogels might serve as good scaffolds for pseudocapacitive materials. However, the microporous structure in the previous reported 3D printed carbon aerogels is not favorable for loading of pseudocapacitive materials. In this work, the 3D printed graphene aerogels were rationally designed as a scaffold for supporting pseudocapacitive MnO_2. They are predominantly macroporous with 5 to 50 µm pores within the 3D printed ligaments. Although this results in a considerably lower specific surface area (*ca.* 27 m^2/g) compared with the graphene aerogel reported previously[18-20], the larger pores, coupled with 3D printing facilitate uniform deposition of MnO_2 throughout the entire graphene aerogel and efficient ion diffusion during charging/discharging even at ultrahigh mass loading of MnO_2. A 4 mm thick graphene aerogel with MnO_2 loading of 182.2 mg cm^{-2} achieves a record high areal capacitance of 44.13 F cm^{-2}, which to our knowledge is the highest value reported for any supercapacitor electrode and the first report of a current collector that is capable of supporting MnO_2 loading at hundreds mg cm^{-2} level. Most importantly, the areal capacitance increases linearly with the mass loading of MnO_2 and electrode thickness while the gravimetric capacitance remains almost unchanged, indicating that the capacitive performance is not limited by ion diffusion, even at such a high mass loading. A device fabricated via a symmetric assembly of two 4 mm thick electrodes yields a maximum energy density of 1.56 mWh cm^{-2}, which is significantly higher than the reported values of any aqueous symmetric capacitors. These findings validate the concept of “printing” a practically feasible pseudocapacitive electrode, which could revolutionize the way of fabricating pseudocapacitor electrodes and devices.

6.2 Experimental Section

Materials Synthesis

Single layer graphene oxide sheets (GO) having a lateral dimension of 300-800 nm purchased from Cheaptubes Inc. were used to prepare the aerogel inks. The GO suspension was prepared by ultra-sonicating 0.800 g of GO in 20.000 g of water for 24 h in a sonication bath. This combination yields a GO concentration of 40.0 mg/mL. The suspension is then mixed with 5.0 wt% of hydroxypropyl methylcellulose (from DOW chemicals) in a planetary Thinky mixer at 2000 rpm for 5 minutes.

The ink is loaded into a 3ml syringe barrel (EFD) and centrifuged for a minute at 4500 rpm to remove air bubbles, after which the ink is extruded through a micro nozzle (400 µm diameter) to pattern 3D structures on a glass substrate. For direct ink writing, the syringe was attached by a luer-lock to a smooth-flow tapered nozzle whose inner diameter(d) is 400 µm. The ink was then extruded by means of an air powered fluid dispenser (Ultimus V, EFD) which provides an appropriate pressure (in the range of 15-20 psi) for writing and the writing speed was kept at 3 mm/sec for all the 3D printed structures. Simple cubic lattices with multiple orthogonal layers of parallel cylindrical rods were printed alternately. The diameter of the cylindrical rods equals the diameter of nozzle and the center-to-center rod spacing of 0.8 mm (for 400 µm nozzle). The height of the electrodes was varied from 1 mm to 4 mm and the layers were stacked on the structure such that each layer has a z spacing of 0.24 mm. To avoid cracking or drying due to evaporation of water, soon after printing, the 3D printed structures are immersed in liquid nitrogen and freeze dried for 48 h in vacuum to form aerogels. The printed aerogels are then subjected to a heat treatment process where the samples were heated in a tube furnace under nitrogen atmosphere at 1050 °C for 3 h with a heating and cooling rate of 2 °C/min to form graphene aerogels.

MnO_2 nanosheets were electrodeposited on the 3D printed graphene electrodes under a constant current density of 10 mA cm^{-2} in a three-electrode electrolytic cell using 0.1 M manganese acetate aqueous solution as electrolyte. The 3D printed graphene aerogel, graphite foil and saturated calomel electrode (SCE) were used as working electrode, counter electrode and reference electrode, respectively. For the 1 mm thick 3D printed graphene aerogel, the deposition time was varied from 300 s to 7200 s to obtain a mass loading of MnO_2 from 2.0 to 45.2 mg cm^{-2}. After deposition, the electrodes were washed with deionized water to remove any residuals and then dried in air at 70 °C overnight. For electrodes with thickness of 2, 3 and 4 mm, the MnO_2 deposition time was increased to 14400, 21600 and 28800 s, respectively.

Control samples were prepared by electrodepositing a comparable amount of MnO_2 onto different substrates including non-3D printed graphene aerogel, carbon cloth, carbon paper, carbon fiber and carbon foil, under the same current density of 10 mA cm^{-2}. The non-3D printed graphene aerogel is prepared under the similar manner with 3D printed graphene aerogel only without employing 3D printing process. Carbon cloth, carbon paper and carbon fiber are purchased from Fuel Cell Earth company, US and carbon foil is purchased from SLG group, Germany.

Mixed-valence vanadium oxide nanowires were deposited on 3D printed graphene electrodes at ambient conditions using cyclic voltammetry from -1.5 to 1.4

V vs. SCE at 50 mV s^{-1} for thirty cycles in an aqueous solution mixture of 0.1 M of vanadium (Ⅳ) oxide sulfate hydrate and 0.2 M ammonium acetate. The as-prepared vanadium oxide nanowires were further reduced at a constant potential of -1.5 V vs. SCE for 1 min in the same electrolyte solution.[43]

Materials Characterization

X-ray diffraction (XRD) spectra of the samples were collected on a powder X-ray diffractometer (Rigaku D-MAX 2200 VPC). Diffraction spectra were recorded from a 2θ angle of 10 to 70° with a step size of 0.02° at a rate of 10° min^{-1}. The structural properties of the materials were investigated by a field emission scanning electron microscope (SEM, FEI Quanta 3D FEG dual beam) and transmission electron microscope (TEM, JEM 2010-HR). X-ray photoelectron spectroscopy (XPS, ESCALab 250) was employed to analyze the chemical composition of samples. Textural properties were determined by Brunauer-Emmett-Teller (BET) and Barrett-Joyner-Halenda (BJH) methods using an ASAP 2020 Surface Area Analyzer (Micromeritics Instrument Corporation) via nitrogen porosimetry. Samples of approximately 0.100 g were heated to 423 K under vacuum (10^{-3} Pa) for at least 24 hours to remove all adsorbed species before the measurements. The electrochemical performance of the electrodes and devices were evaluated in a 3.0 M LiCl aqueous electrolyte using electrochemical workstations (CHI 660D and BioLogic EC-Lab SP-300). The geometric area of all working electrodes is 0.2 cm^2.

Calculations

Gravimetric capacitance (C_G), areal capacitance (C_A) and volumetric capacitance (C_V) of single electrodes and devices are calculated based on the galvanostatic charging and discharging curves using Equation 1, Equation 2 and Equation 3, respectively.

$$C_G = \frac{I \times t}{\Delta U \times m} \text{ (Equation 1)}$$

$$C_A = \frac{I \times t}{\Delta U \times A} \text{ (Equation 2)}$$

$$C_V = \frac{I \times t}{\Delta U \times V} \text{ (Equation 3)}$$

Where C_G, C_A and C_V are the gravimetric, areal and volumetric capacitance (F g^{-1}, F cm^{-2} or F cm^{-3}), ΔU is the potential window (V), I is the discharge current (A), t is the discharge time (s), m is the mass loading of the materials on the electrodes (g), A is the geometric electrode working area (cm^2), and V is the volume of the electrodes (cm^3). For the devices, m is the total mass of two identical electrodes (g), A is the geometric electrode working area (cm^2), and V is the total volume of the two electrodes (cm^3)

Areal energy density (E, mWh cm^{-2}) and power density (P, mW cm^{-2}) of the symmetric device are calculated using the following equations:

$$E_A = \frac{1000}{2 \times 3600} C_A U^2 \text{ (Equation 4)}$$

$$P_A = \frac{3600 \times E_A}{t} \qquad \text{(Equation 5)}$$

Where C_A is the areal capacitance (F cm^{-2}), U is the working voltage (V) and t is the discharging time (s) measured in the galvanostatic charging and discharging experiments.

6.3 Results and Discussions

The fabrication process of 3D printed graphene/MnO_2 electrodes is illustrated in Figure 6.1. 3D graphene oxide structures were printed by direct ink writing method using an “ink” containing a mixture of graphene oxide (GO) suspension (40 mg/mL) and 5% hydroxypropyl methylcellulose. The 3D printed structures were consequently freeze dried to form aerogels, followed by annealing in nitrogen gas to convert graphene oxide to graphene (G). The printed lattice structure is constructed with multiple orthogonal layers of parallel porous cylindrical rods (Figure 6.2A, B). The diameter of the cylindrical rods and the center-to-center rod spacing are around 400 and 800 µm, respectively. The lattice structure has a reasonably low mass density of 46.0 mg/cm^3 and specific surface area of 27 m^2/g. MnO_2 nanosheets were then electrodeposited onto the graphene aerogel lattice (Figure 6.1). As shown in Figure 2C and D, the porous cylindrical rods are coated with MnO_2. Importantly, the deposition of MnO_2 take place not only on the exterior surface, but also the interior of the entire lattice (Figure 6.2 and 6.3). The uniform deposition of MnO_2 indicates that the graphene aerogel has good electrical conductivity and the 3D printed lattice allows efficient diffusion of electrolyte solution. In contrast, for the bulk graphene aerogels, most of the MnO_2 are deposited only on the exterior surface due to the mass transport limited ion diffusion (Figure 6.4 and 6.5). Notably, the thickness of MnO_2 layer on the 3D printed graphene aerogel increases slowly with the electrodeposition time, as shown in Figure 6.2E. It provides good control on the mass loading of MnO_2. SEM images revealed that the MnO_2 layer contains interconnected nanosheets, which have an average diameter of hundreds of nanometers and thickness of several nanometers (Figure 6.2F). The addition of these ultrathin nanosheets increase the specific surface area of the graphene aerogel lattice to around 100 m^2/g. X-ray diffraction (XRD) and X-ray photoelectron spectroscopy (XPS) results identified the nanosheets are ε-MnO_2.[10] Transmission electron microscopic (TEM) images together with energy dispersive X-ray spectroscopy (EDS) mapping results revealed the uniform distribution of polycrystalline MnO_2 nanosheets on the graphene nanosheets (Figure 6.7 and 6.8). Taken together, these results confirm the successful integration of the 3D printed graphene aerogel and pseudocapacitive MnO_2 nanosheets and demonstrate the importance of using the 3D printed graphene aerogel as scaffold in achieving a uniform coating of MnO_2 at high mass loadings.

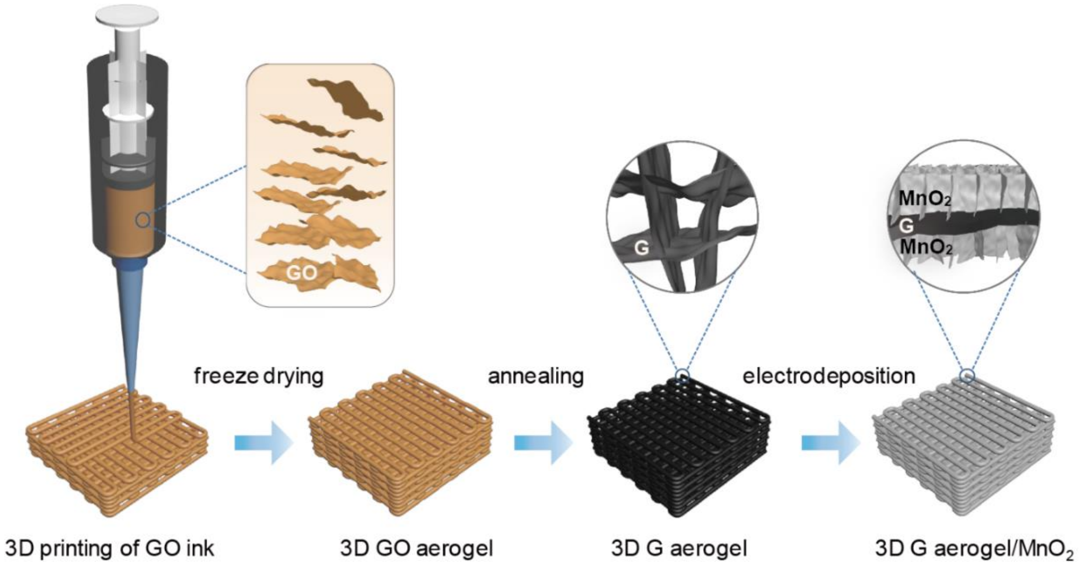

Figure 6.1 Schematic illustration of fabrication of 3D printed graphene aerogel/MnO_2 electrode

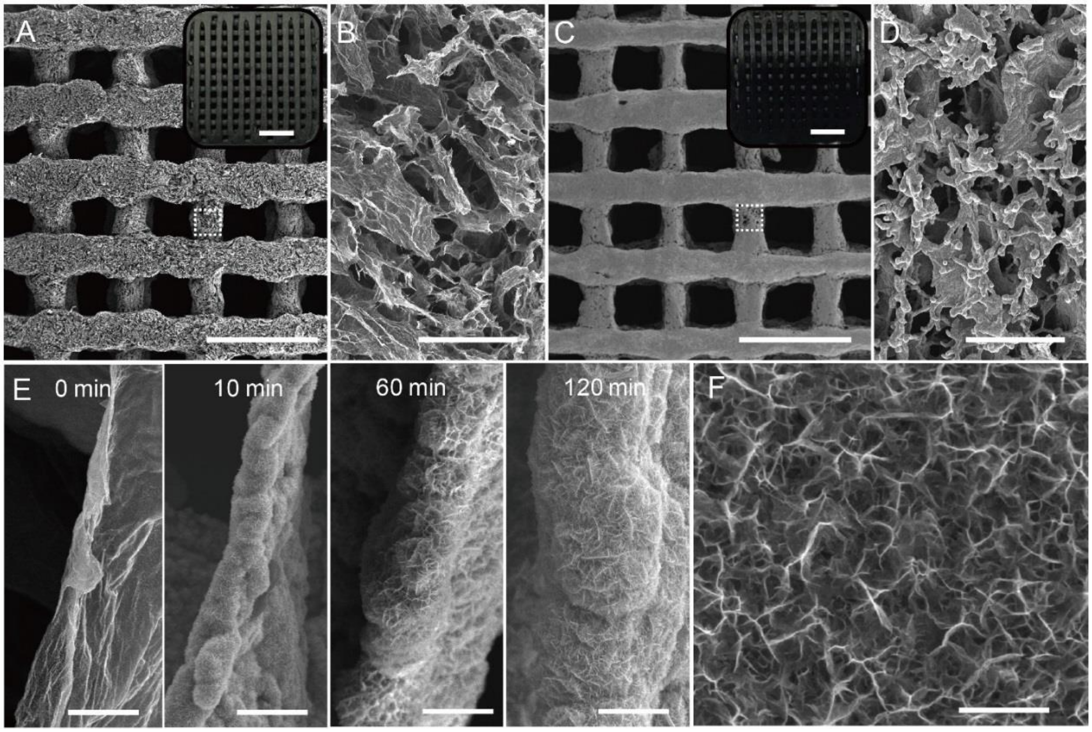

Figure 6.2 Microscopic characterization of 3D printed electrodes

(A) Top view SEM image of a 3D printed graphene aerogel lattice. Scale bar: 1 mm.

(B) Magnified image collected from a cylindrical rod highlighted in A. Scale bar: 40 μm.

(C) Top view SEM image of a 3D printed graphene aerogel lattice electrodeposited with MnO_2 for 600 s. Scale bar: 1 mm.

(D) Magnified image collected from a cylindrical rod highlighted in C. Scale bar: 40 μm. Insets in A and C are top view digital images of 3D printed graphene aerogel and graphene aerogel/MnO_2, respectively. Scale bars in insets are 5 mm.

(E) SEM images collected from the edge of a graphene nanosheet at different stages of electrodeposition of MnO_2. Scale bars: 2 μm.

(F) SEM image of MnO_2 nanosheets electrodeposited on a graphene nanosheet. Scale bar: 300 nm.

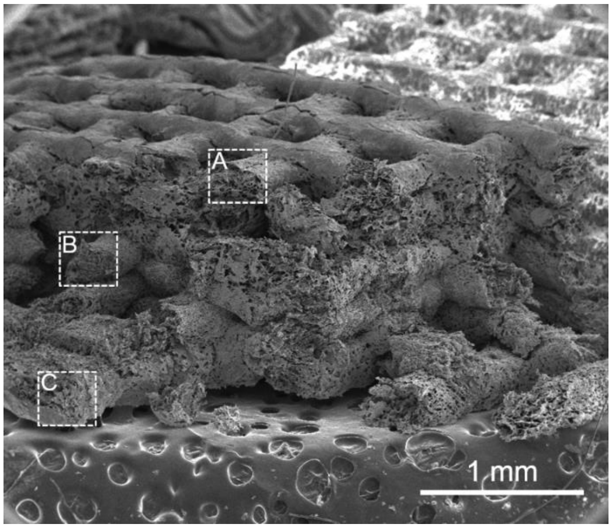

Figure 6.3 SEM image collected from a cross section of a 3D G/MnO_2 electrode.

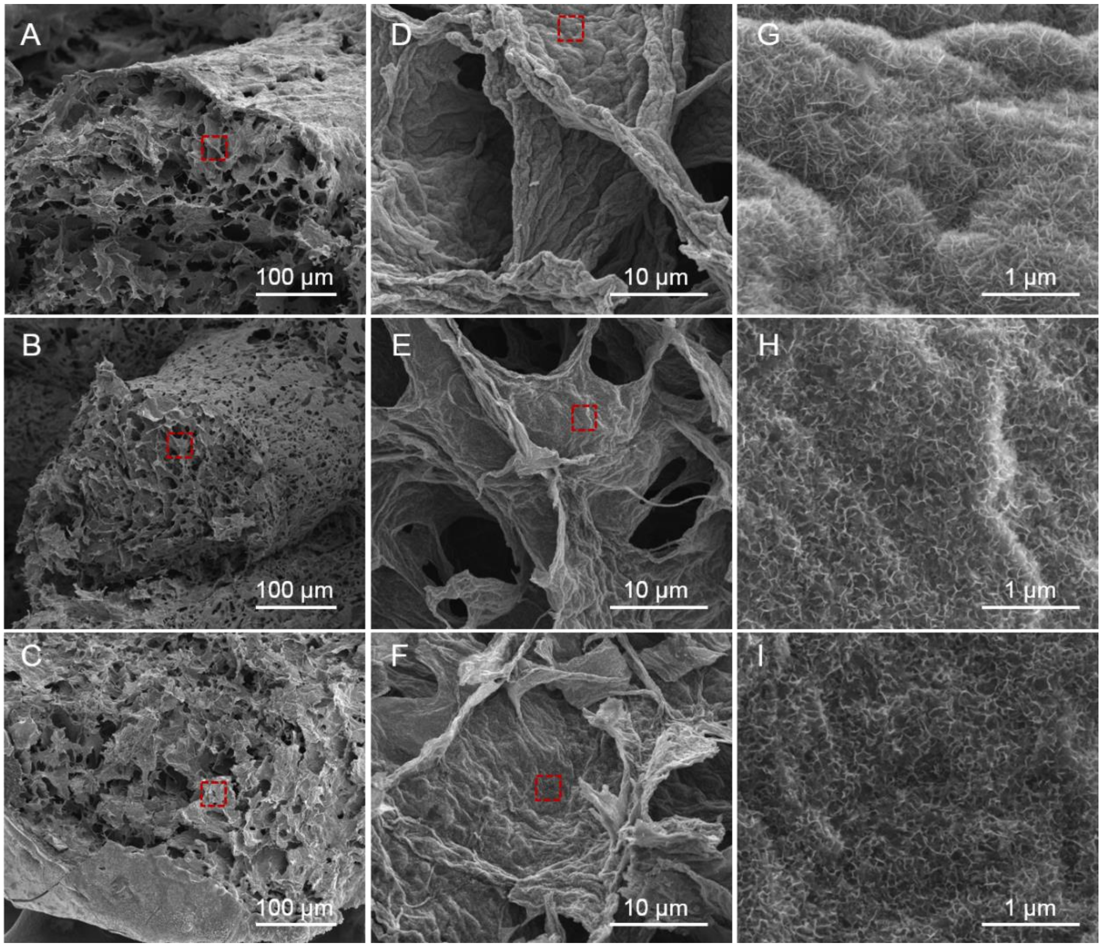

Figure 6.4 SEM images collected from the interior of graphene aerogel lattice.

(A-C) Magnified SEM images collected from the dashed boxes highlighted in Figure S2. (D-F) Magnified SEM images collected from the dashed boxes highlighted in A, B and C. (G-I) Magnified SEM images collected from the dashed boxes highlighted in D, E and F.

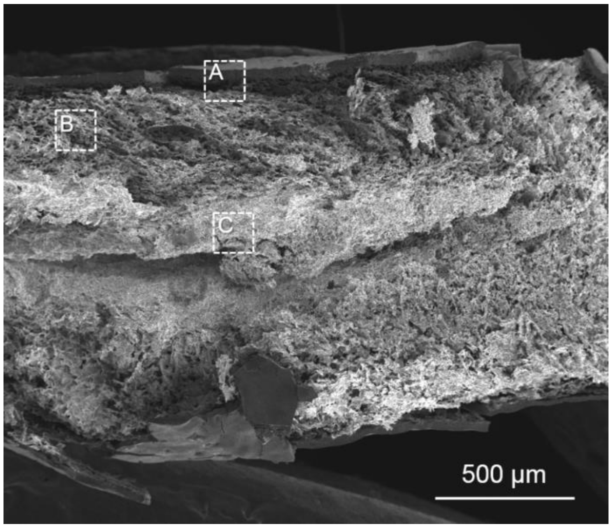

Figure 6.5 SEM image collected from a cross section of a bulk G/MnO_2 electrode.

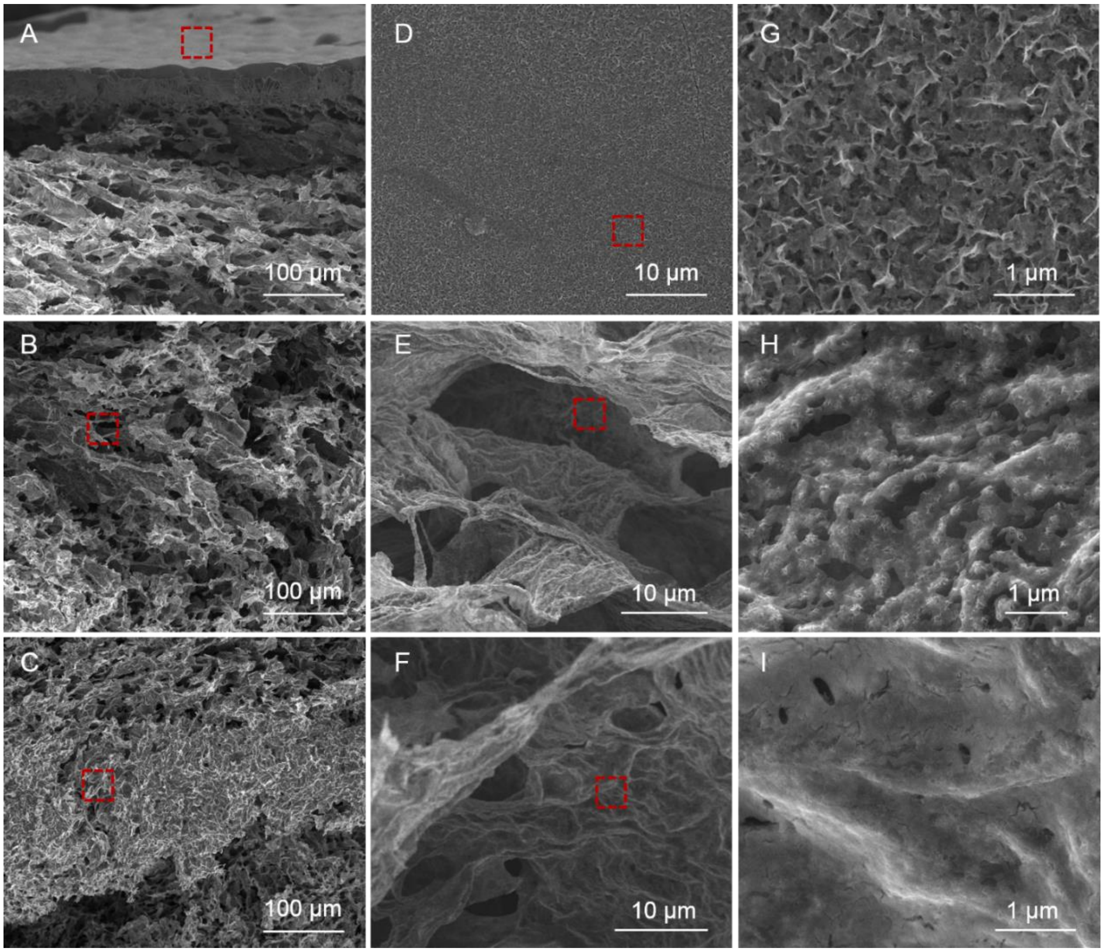

Figure 6.6 SEM images collected from the interior of bulk graphene aerogel. (A-C) Magnified SEM images collected from the dashed boxes highlighted in Figure S4. (D-F) Magnified SEM images collected from the dashed boxes highlighted in A, B and C. (G-I) Magnified SEM images collected from the dashed boxes highlighted in D, E and F.

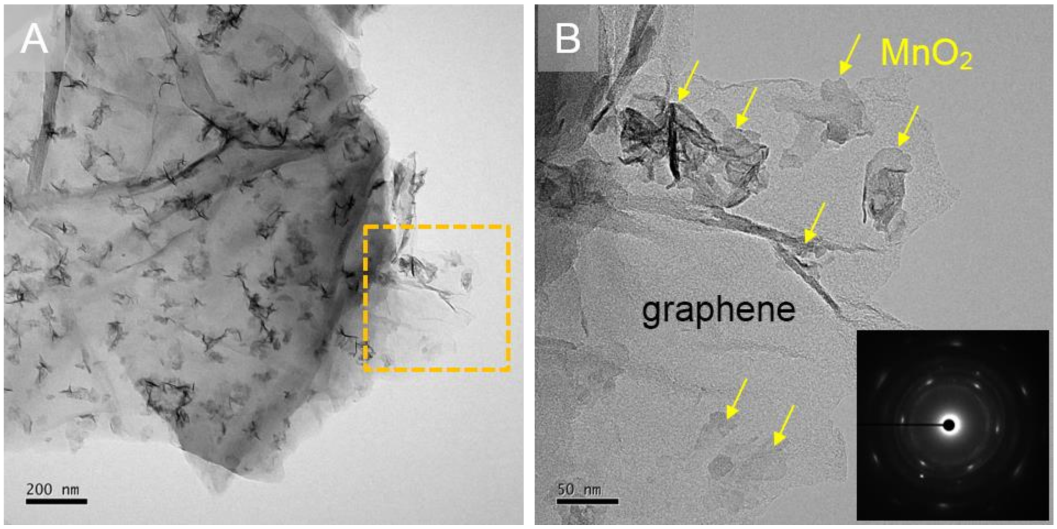

Figure 6.7 (A) TEM image of MnO_2 nanosheets deposited on 3D printed graphene nanosheets. (B) Magnified TEM images collected from the dashed box highlighted in A. Insert shows the SAED pattern of graphene/MnO_2 composite.

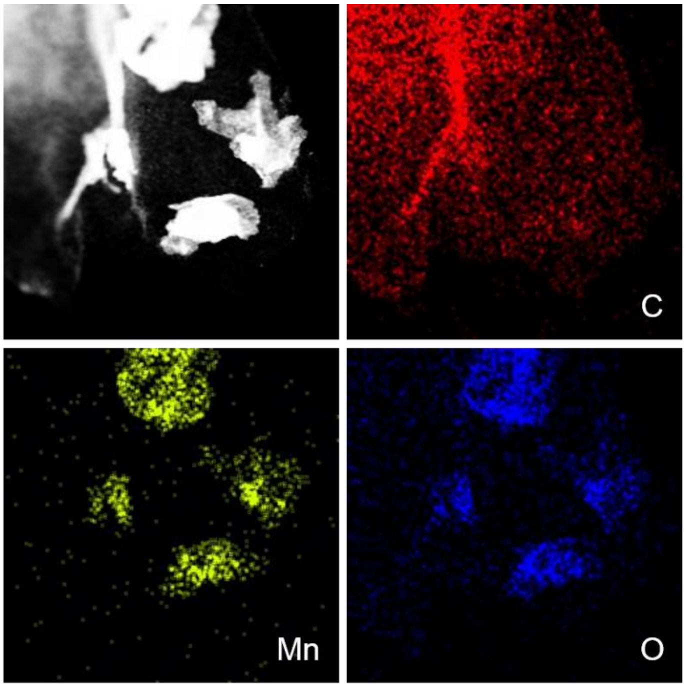

Figure 6.8 EDS mapping of MnO_2 nanosheets deposited on 3D printed graphene nanosheets.

Electrochemical properties of 1 mm thick 3D printed graphene aerogel (G) and graphene aerogel/MnO_2 (G/MnO_2) electrodes were investigated in 3M LiCl solution in a three-electrode electrolytic cell. As shown in Figure 6.9A, the deposition of MnO_2 on a graphene aerogel electrode for just 5 mins (with a loading of 2 mg cm^{-2}) significantly increases its capacitance. The areal capacitance of G/MnO_2 electrode is ~25 times higher than the value of bare G electrode obtained at the same current densities (Figure 6.9B). There is a linear relationship between mass loading of MnO_2 and electrodeposition time, which allows precise control of MnO_2 loading (Figure 6.9C). An ultrahigh mass loading of 45.2 mg cm^{-2} MnO_2 was obtained after 120 mins deposition. Significantly, the areal and volumetric capacitance of 3D G/MnO_2 electrodes also increase almost linearly with the MnO_2 loading at different current densities (Figure 6.9D). The most highly loaded (45.2 mg cm^{-2}) electrode delivers excellent areal and volumetric capacitances of 11.55 F cm^{-2} and 115.5 F cm^{-3}, respectively (Figure 6.10). Most importantly, under such an ultrahigh mass loading, the 3D G/MnO_2 electrode retains an extraordinarily high rate capability of 73.2 % from 0.5 to 10 mA cm^{-2} (Figure 6.11). These results unambiguously show that charge transfer and ion diffusion in these 3D printed electrodes are highly efficient.

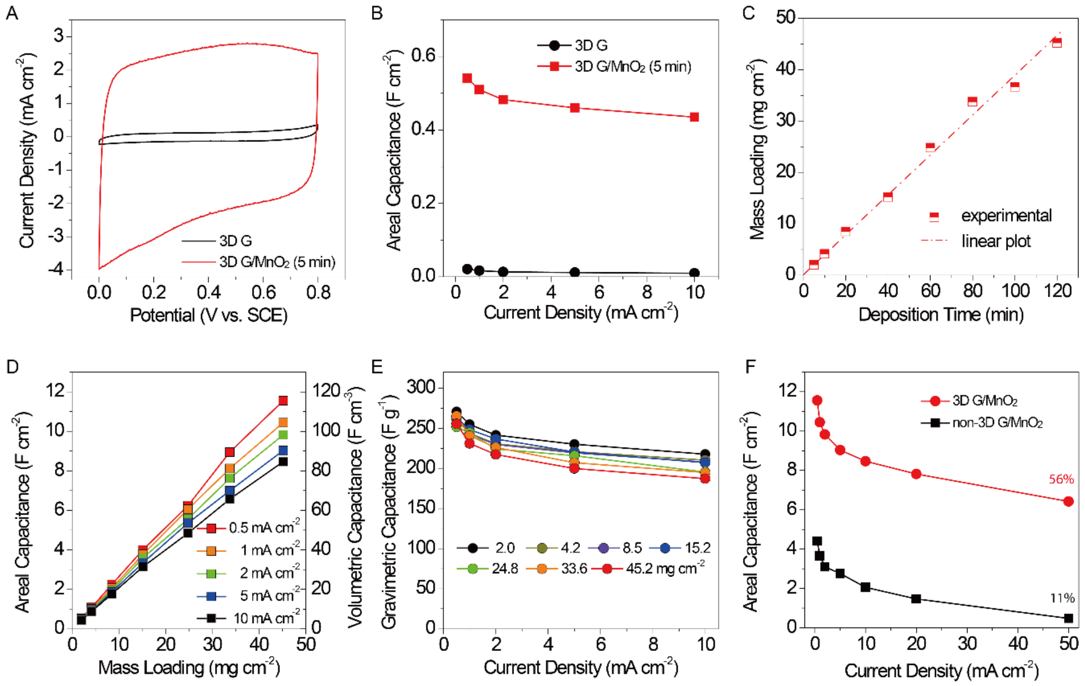

Figure 6.9 Electrochemical performance of 3D G/MnO_2 electrodes

(A) CV curves of 3D G and 3D G/MnO_2 electrodes (5 min deposition) collected at 5 mV/s.

(B) Areal capacitance of 3D G and 3D G/MnO_2 electrodes (5 min deposition) obtained at different current densities.

(C) Relationship between the mass loading of MnO_2 and the electrodeposition time.

(D) Areal capacitances and volumetric capacitances obtained from 3D G/MnO_2 electrodes with different mass loading of MnO_2 at different current densities.

(E) Gravimetric capacitances obtained at different current densities from 3D G/MnO_2 electrodes loaded with different amount of MnO_2.

(F) Areal capacitances of 3D G/MnO_2 and non-3D printed G/MnO_2 electrodes obtained at different current densities. The percentage values are the capacitance retention percentages when the current density increase from 0.5 to 50 mA cm^{-2}.

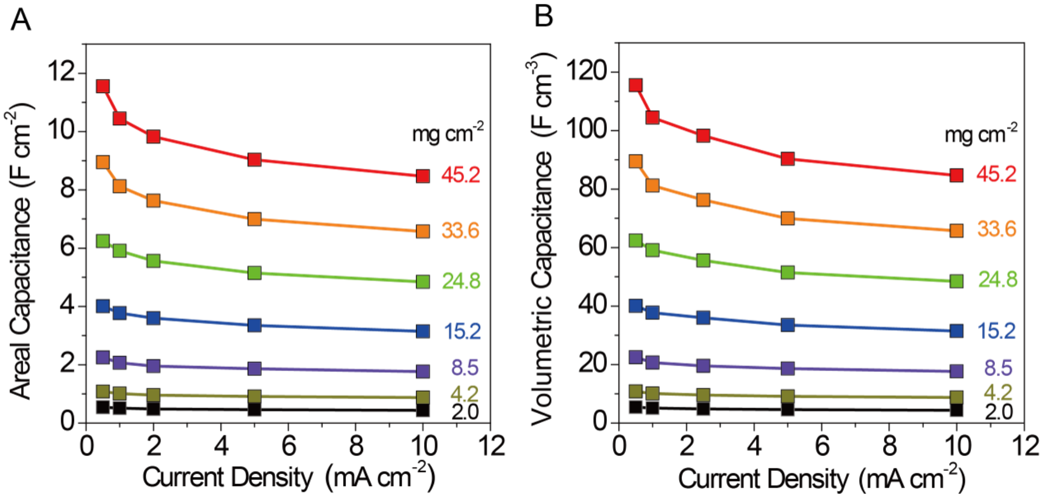

Figure 6.10 (A) Areal and (B) volumetric capacitance collected for 3D G/MnO_2 electrodes with different MnO_2 mass loadings at different current densities.

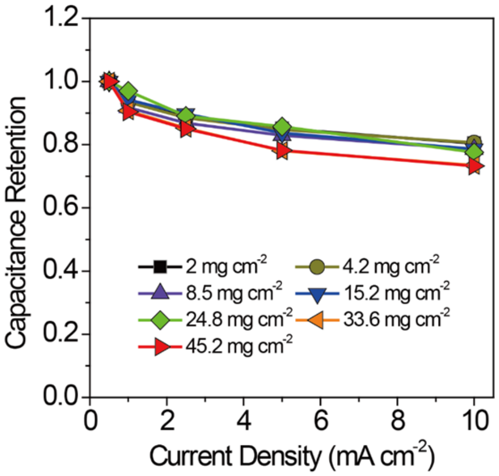

Figure 6.11 Capacitance retention of 3D G/MnO_2 electrodes with different MnO_2 mass loadings obtained at different current densities.

As a result, their gravimetric capacitances normalized to the mass of MnO_2 only slightly decrease when the MnO_2 loading increased drastically from 2.0 to 45.2 mg cm^{-2} (Figure 6.9E). The electrode with MnO_2 loading of 45.2 mg cm^{-2} achieved a specific capacitance of 187.2 F/g at 10 mA cm^{-2}, which is even higher than the values reported for most of the MnO_2-based electrodes with fractions of the present mass loading.[7, 10, 15, 16, 21, 22] Moreover, when the gravimetric capacitance is normalized to the mass of the entire G/MnO_2 electrode, it increases with the loading MnO_2 and remains almost unchanged when the loading of MnO_2 is significantly higher than the mass of graphene aerogel (4.6 mg cm^{-2}) (Figure 6.12). These results demonstrates the practical importance of having an electrode with the mass of active material considerably higher than the weight of current collector.[23] A major breakthrough demonstrated in these results is the capability of substantially increasing the loading of pseudocapacitive material without sacrificing the rate capability and gravimetric capacitance, which is essential for developing practically useful pseudocapacitors.

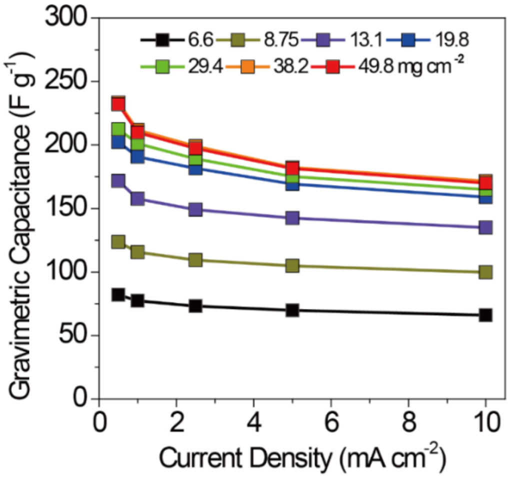

Figure 6.12 Gravimetric capacitance of 3D G/MnO_2 electrodes collected at different current densities. The gravimetric capacitances are normalized to the mass of the entire electrode (the total weight of graphene aerogel and MnO_2).

The outstanding performance of 3D G/MnO_2 electrodes is believed to be closely related to its unique 3D porous architecture that is highly conductive and favourable for electrolyte and ion diffusion. A number of control experiments were performed to understand the role of 3D printed lattice structure on the electrode performance.

First, we compare the performance difference between a 3D printed and a non-3D printed graphene aerogel, which are made by the same method (except printing) and have comparable electrical conductivity, sample thickness and electrochemically active surface area. The morphology of MnO_2 nanosheets grown on both samples are also similar. Under the same loading of MnO_2 (~45.0 mg cm^{-2}), the non-3D printed graphene aerogel/MnO_2 exhibits considerably lower areal capacitance compared to its 3D printed counterpart, as shown in Figure 6.9F. The capacitance discrepancy between these two samples is even larger at high current densities, suggesting that ion diffusion is the key limiting factor in the non-3D printed structure. This is also supported by electrochemical impedance spectroscopy (EIS) results. As shown in Figure 6.13, while the 3D G/MnO_2 and non-3D G/MnO_2 exhibit similar equivalent series resistances (R_s), the 3D G/MnO_2 shows considerably smaller charge transfer resistance and ion diffusion resistances (Table 6.1).

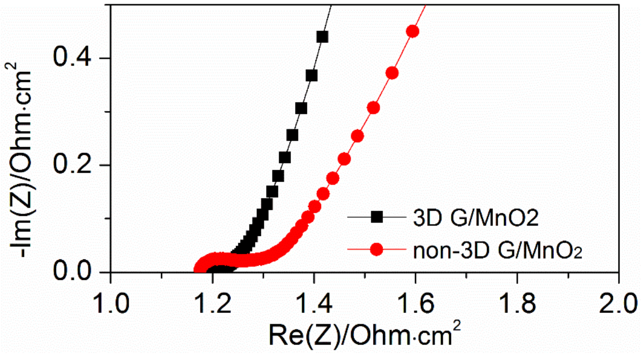

Figure 6.13 Nyquist plots of 3D printed G/MnO_2 and non-3D printed G/MnO_2 electrodes with the same thickness.

Table 6.1 Equivalent series resistances (R_s), charge-transfer resistances (R_{ct}) and Warburg resistances (W) of the equivalent circuit fitted with the Nyquist plots for 3D printed G/MnO_2 electrode and non-3D printed G/MnO_2 electrode.

Electrode	**R_s ($\Omega\cdot cm^2$)**	**R_{ct} ($\Omega\cdot cm^2$)**	**W ($\Omega\cdot cm^2\cdot s^{0.5}$)**
3D printed G/MnO_2	1.19	0.0254	0.1073
Non-3D printed G/MnO_2	1.18	0.1196	0.1662

We also conduct further comparisons between 3D printed graphene aerogel and other commonly used carbon substrates, including carbon cloth, carbon paper, carbon fiber and carbon foil. Under similar loading of MnO_2 (~45.0 mg cm^{-2}), 3D G/MnO_2 again showed significantly higher areal capacitance than all control samples at all current densities we studied (Figure 6.14). These comparative studies confirmed the important role of 3D printed lattice structure as a scaffold for supporting high mass loading of MnO_2. We believe the unique structural features of the 3D printed graphene aerogel in enhancing the performance under ultrahigh mass loading is the reasonably large surface area of porous graphene aerogel and the periodic arrangement of macroscopic scale pores that enables sufficient and rapid diffusion of ions to the electrode surface.

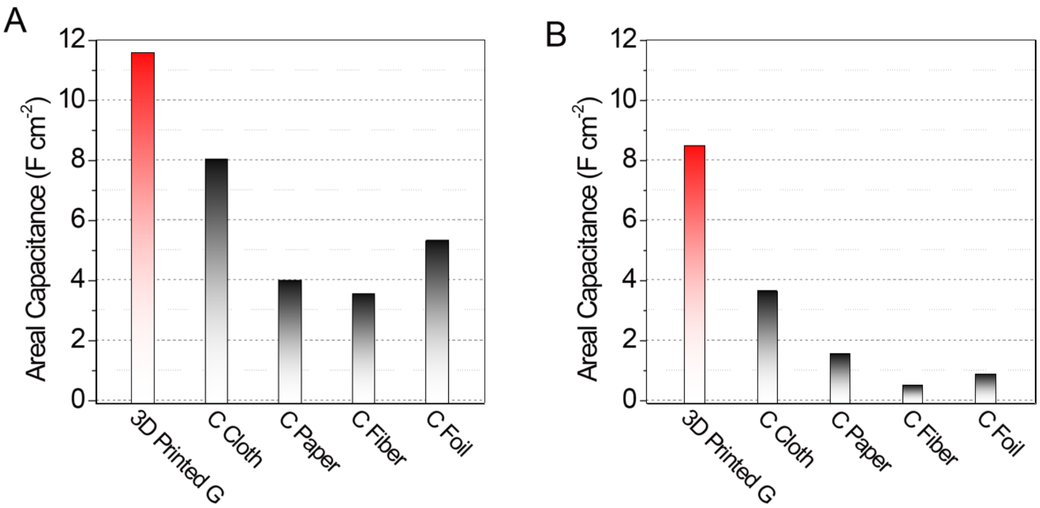

Figure 6.14 Comparison of the areal capacitance of 3D G/MnO_2, carbon cloth/MnO_2, carbon paper/MnO_2, carbon fiber/MnO_2, and carbon foil/MnO_2, at current densities of (A) 0.5 mA cm^{-2} and (B) 10 mA cm^{-2}.

The capability of increasing mass loading of pseudocapacitive materials on 3D printed graphene aerogel could open up exciting new opportunities in supercapacitor electrode design and fabrication. Currently, the commercial supercapacitor electrodes were fabricated by depositing thin carbon-based film on metal current collectors.[1] The film thickness is limited by the sluggish ion diffusion and/or charge transfer in the electrode, as the performance of most electrodes deteriorate rapidly with the increase of electrode thickness. To achieve higher capacitance and energy density for practical application, these thin carbon film electrodes have to be stacked together, resulting in additional weight and material cost as multiple layers of metal current collector and separator are required. The excellent ion diffusion demonstrated in the 1 mm thick 3D G/MnO_2 electrode suggests that the electrode thickness could be further increased without significantly affecting the capacitive performance. Eliminating the need of stacking multiple thin film electrodes by directly “printing” the entire thick, monolithic electrode could revolutionize the way of fabricating supercapacitor electrodes and devices.

To investigate the feasibility of this electrode fabrication concept, we increase the thickness of 3D printed graphene aerogel lattice from 1 mm up to 4 mm (Figure 6.15A). Extremely high mass loading of 89.8, 135.3 and 182.2 mg cm^{-2} were obtained on the 2 mm, 3 mm and 4 mm thick electrodes, respectively. To our knowledge, this is the first report of a supercapacitor electrode with mass loading of active material over 100 mg cm^{-2}. Remarkably, the areal capacitance of the 3D G/MnO_2 electrodes increases linearly with the electrode thickness at both low current density of 0.5 mA cm^{-2} and high current density of 10 mA cm^{-2} (Figure 6.15B). Electrodes with different thicknesses all have similar gravimetric and volumetric capacitances (Figure 6.15C), indicating that ion diffusion is still not limiting the capacitive performance even in the thickest 4 mm electrode.

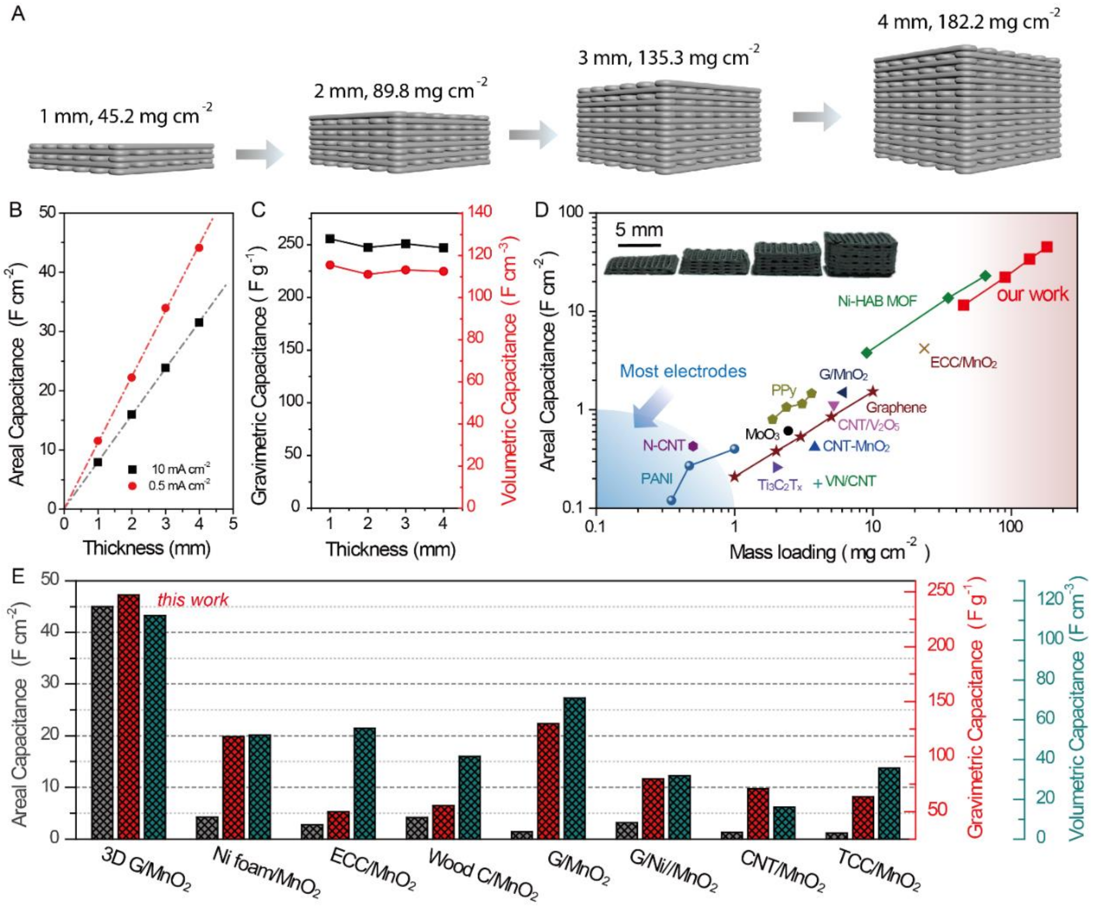

Figure 6.15 Electrochemical performance of 3D printed graphene/MnO_2 electrodes with different thicknesses (1-4 mm)

(A) Schematic illustration of 3D G/MnO_2 electrodes with different thicknesses and mass loadings of MnO_2.

(B) Areal capacitance of the electrodes measured at 0.5 mA cm^{-2} and 10 mA cm^{-2} are plotted as a function of electrode thickness.

(C) Gravimetric capacitance and volumetric capacitances are plotted as a function of electrode thickness.

(D) A plot compares the areal capacitances of 3D G/MnO_2 electrodes with the values of previously reported electrodes with high mass loading of pseudocapacitive materials (PANI,[24] N-CNT,[25] MoO_3,[26] PPy,[27] Graphene,[28] G/MnO_2,[29] $Ti_3C_2T_x$,[6] VN/CNT,[30] CNT-MnO_2, CNT/V_2O_5,[31] ECC/MnO_2,[10] Ni-HAB MOF[32]). Inset: digital image of 3D printed graphene/MnO_2 electrodes with different thicknesses (1-4 mm). (E) A plot compares the areal capacitance, gravimetric capacitance and volumetric capacitance of the 4 mm thick 3D printed graphene/MnO_2 electrode with the values of previously reported high mass loading MnO_2-based electrodes (Ni foam/MnO_2,[21] ECC/MnO_2,[10] Wood C/MnO_2,[38] G/MnO_2,[15] G/Ni/MnO_2,[29] CNT/MnO_2,[22] TCC/MnO_2[39]).

The 4 mm thick electrode achieves an ultrahigh areal capacitance of 44.13 F cm^{-2}, which is the highest areal capacitance reported for supercapacitor electrodes (Figure 6.15D).[6, 10, 22, 24-37] It also achieves impressive gravimetric capacitance of 242.19 F g^{-1} and volumetric capacitance of ~110 F cm^{-3} (Figure 6.15E). These values (gravimetric and volumetric capacitances) are considerably higher than the values reported for MnO_2-based electrodes with substantially smaller loadings of MnO_2 (Figure 6.15E).[10, 15, 21, 22, 38, 39] EIS analysis show that the 3D printed G/MnO_2 electrodes with different thicknesses have similar R_s and Warburg resistances (Figure 6.16 and Table 6.2), reflecting their superior conductivity and ion diffusion efficiency. It explains why when the electrode thickness increase, the areal capacitance increased almost linearly while retaining the gravimetric and volumetric capacitances. The 3D printed graphene aerogel as a scaffold successfully breaks the trade-off between high areal capacitance, high gravimetric capacitance and high volumetric capacitance. Notably, 4 mm is not the thickness limit for 3D G/MnO_2 electrode, we anticipate that the areal capacitance can be further increased by increasing the electrode thickness until the performance is eventually limited by ion diffusion, while further performance optimization is beyond the scope of this work. These results have validated the concept of “printing” a practically feasible electrode, which could pave a new way for fabricating high areal capacitance supercapacitor electrodes.

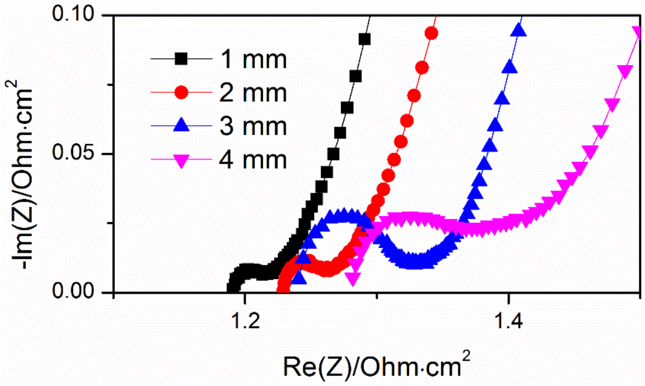

Figure 6.16 Nyquist plots of 3D printed G/MnO$_2$ electrodes with different thickness

Table S4. Equivalent series resistances (R_s), charge-transfer resistances (R_{ct}) and Warburg resistances (W) of the equivalent circuit fitted with the Nyquist plots for the 3D printed G/MnO$_2$ electrodes with different thickness.

Electrode Thickness (mm)	**R_s ($\Omega\cdot cm^2$)**	**R_{ct} ($\Omega\cdot cm^2$)**	**W ($\Omega\cdot cm^2\cdot s^{0.5}$)**
1	1.19	0.0254	0.1073
2	1.23	0.0385	0.1156
3	1.24	0.1050	0.1186
4	1.28	0.1234	0.1329

Symmetric supercapacitor devices were fabricated through the assembly of two 4 mm thick 3D G/MnO$_2$ electrodes. The device shows characteristic capacitive behaviour with triangular galvanostatic charging and discharging curves (Figure 6.17A). It delivered an excellent areal capacitance of 18.74 F cm^{-2} at 1 mA cm^{-2} and was able to retain ~67% of the capacitance at high current density of 20 mA cm^{-2} (Figure 6.17B). The areal capacitance of the 8 mm thick device is approximately 4 times higher than the 2 mm thick device, which demonstrate the scalability of 3D G/MnO_2 device. Furthermore, good cycling stability is equally important for any charge storage devices. This symmetric device retains a remarkable 92.9 % of its initial capacitance after 20000 cycles (Figure 6.17C). The 3D printed structure and the nanosheet morphology of MnO_2 are well preserved after cycling (Figure 6.18).

Low energy density has been considered as a major drawback of supercapacitors as energy storage devices. Since the energy density is directly proportional to the device capacitance, achieving ultrahigh areal capacitance in 3D G/MnO_2 devices offer new possibility in addressing this long-standing challenge. The 8 mm thick device yields a maximum areal energy density of 1.56 mWh cm^{-2}, which is the highest value reported for aqueous symmetric capacitors (Figure 6.17D and Figure 6.19).[5, 16, 24, 27, 40-42]

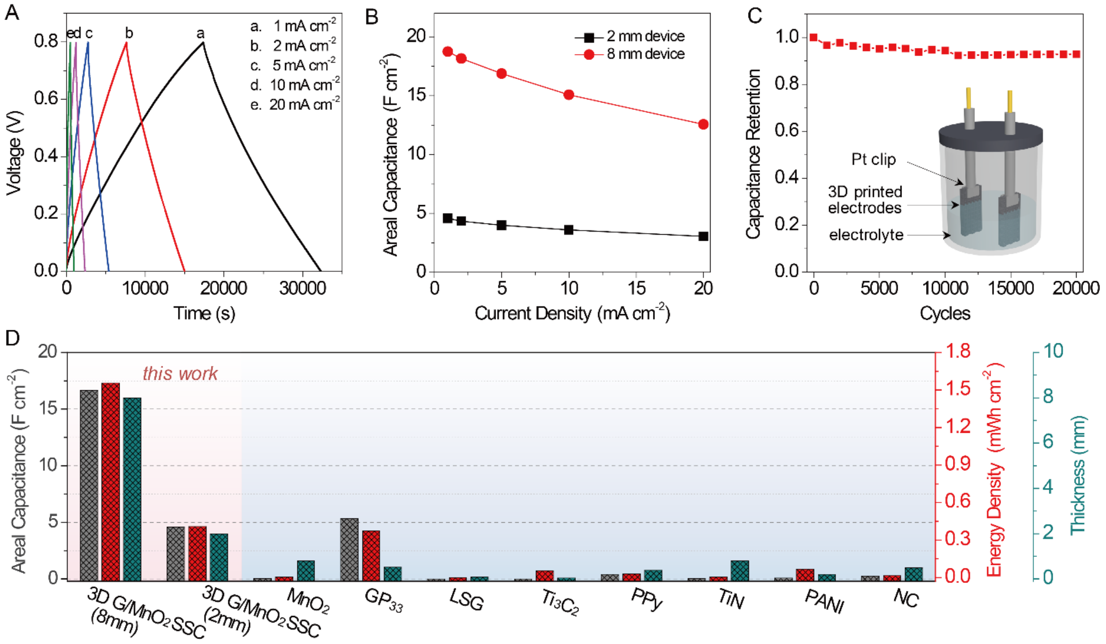

Figure 6.17 Electrochemical performance of symmetric 3D G/MnO_2 // 3D G/MnO_2 supercapacitor devices

(A) Galvanostatic charging and discharging curves of an 8 mm thick symmetric supercapacitor measured at different current densities.

(B) Areal capacitances of 2 mm and 8 mm thick device obtained at different current densities.

(C) Capacitance retention of a 2 mm thick device tested at a scan rate of 20 mV/s for 20000 cycles. Inset: schematic illustration of a symmetric supercapacitor device tested in aqueous electrolyte.

(D) A plot compares the areal capacitance, energy density and device thickness of 3D printed graphene/MnO_2 based supercapacitors with the values of previously reported symmetric supercapacitor devices (MnO_2,[15] GP_{33},[35] LSG,[40] Ti_3C_2,[5] PPy,[27] TiN,[41] PANI,[24] NC[42]).

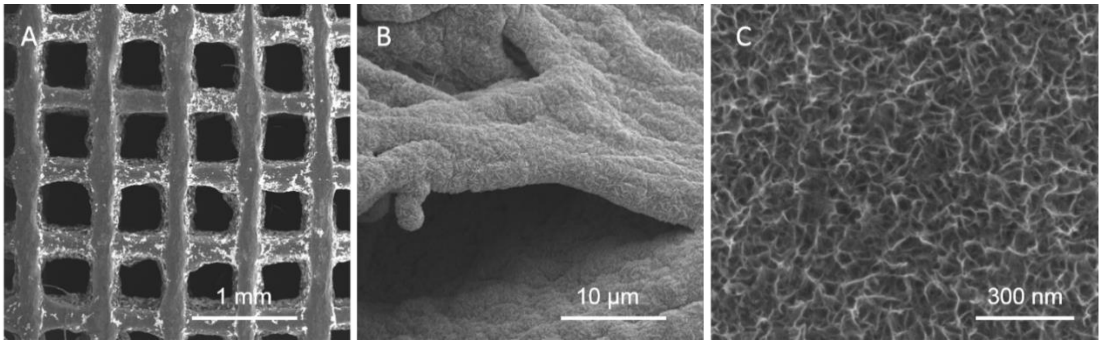

Figure 6.18 SEM images of the 3D G/MnO_2 electrodes after stability test.

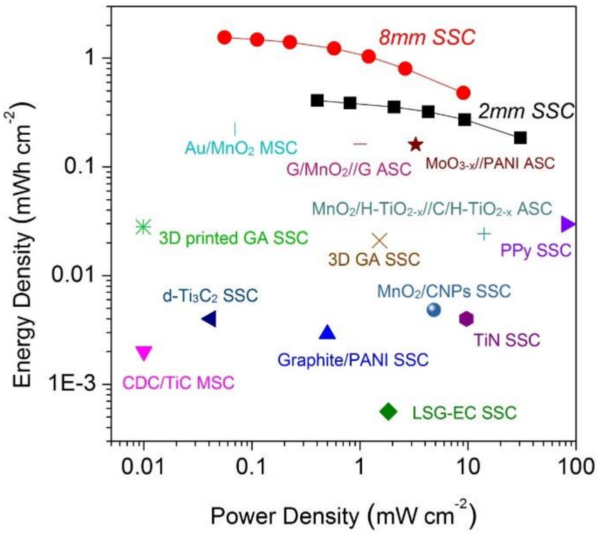

Figure 6.19 Ragone plots compare the energy densities and power densities of the 8 mm-thick and 2 mm-thick 3D G/MnO$_2$ symmetric supercapacitor devices with the benchmark values previously reported for representative supercapacitors (Au/MnO$_2$ SSC,[8] G/MnO$_2$//G ASC,[9] MoO$_{3-x}$//PANI ASC,[10] MnO$_2$/H-TiO$_{2-x}$//C/H-TiO$_{2-x}$ ASC,[11] 3D printed GA SSC,[12] 3D GA SSC,[13] PPy SSC,[14] d-Ti$_3$C$_2$ SSC,[15] MnO$_2$/CNPs SSC,[16] CDC/TiC MSC,[17] Graphite/PANI SSC,[18] TiN SSC,[19] LSG-EC SSC[20]).

We also prepare an asymmetric device by employing the 3D G/MnO$_2$ (10.3 mg/cm^2) as positive electrode and 3D printed graphene aerogel deposited with mixed-valence vanadium oxide (3D G/VO$_x$, 3.6 mg/cm^2) as negative electrode. This asymmetric device achieves a working voltage window of 2.2 V. When two devices are connected in series, they can be charged to 4.4 V at a rate of 50 mA/cm^2 within 36 s. This tandem device with a working area of only 0.2 cm^2 can power a blue LED (3.0V, 5 mm) for 5 min. It shows that the devices can be used for applications that requires higher voltage output. More development of asymmetric devices using this ultrahigh loading of active materials is the focus of a future study.

6.4 Conclusions

In summary, we demonstrated the capability of 3D printed macro-porous graphene aerogel scaffold for supporting hundreds mg cm^{-2} level MnO_2 loading for the first time. The engineered porous structure allows efficient ion diffusion and therefore enables the ultrahigh mass loading of pseudocapacitive materials without sacrificing their gravimetric and volumetric capacitive performance. Most importantly, the linear increase of areal capacitance with the thickness of 3D printed monolithic electrodes suggests their great promises for practical application and could innovate the conventional layer-by-layer stacking fabrication process of commercial supercapacitors.

References

1. P. Simon, Y. Gogotsi, *Nat. Mater.* **2008**, *7*, 845-854.
2. V. Augustyn, P. Simon, B. Dunn, *Energy Environ. Sci.* **2014**, *7*, 1597-1614.
3. V. Augustyn, J. Come, M. Lowe, J. Kim, P. Taberna, S. Tolbert, H. Abruna, P. Simon, B. Dunn, *Nat. Mater.* **2013**, *12*, 518-522.
4. M. Acerce, D. Voiry, M. Chhowalla, *Nat. Nanotechnol.* **2015**, *10*, 313-318.
5. M. Lukatskaya, O. Mashtalir, C. Ren, Y. Dall'Agnese, P. Rozier, P. Taberna, M. Naguib, P. Simon, M. Barsoum, Y. Gogotsi, *Science* **2013**, *341*, 1502-1505.
6. M. Ghidiu, M. Lukatskaya, M. Zhao, Y. Gogotsi, M. Barsoum, *Nature* **2014**, *516*, 78-81.

7. J. Wang, F. Kang, B. Wei, *Prog. Mater. Sci.* **2015**, *74*, 51-124.

8. X. Lu, T. Zhai, X. Zhang, Y. Shen, L. Yuan, B. Hu, L. Gong, J. Chen, Y. Gao, J. Zhou, Y. Tong, Z. Wang, *Adv. Mater.* **2012**, *24*, 938-944.

9. H. Lee, J. Goodenough, *J. Solid. State. Chem.* **1999**, *144*, 220-223.

10. Y. Song, T. Liu, B. Yao, M. Li, T. Kou, Z. Huang, D. Feng, F. Wang, Y. Tong, X. Liu, Y. Li, *ACS Energy Lett.* **2017**, *2*, 1752-1759.

11. S. Devaraj, N. Munichandraiah, *J. Phys. Chem. C* **2008**, *112*, 4406-4417.

12. P. Yang, Y. Ding, Z. Lin, Z. Chen, Y. Li, P. Qiang, M. Ebrahimi, W. Mai, C. Wong, Z. Wang, *Nano Lett.* **2014**, *14*, 731-736.

13. T. Zhai, S. Xie, M. Yu, P. Fang, C. Liang, X. Lu, Y. Tong, *Nano Energy* **2014**, *8*, 255-263.

14. J. Kang, A. Hirata, L. Kang, X. Zhang, Y. Hou, L. Chen, C. Li, T. Fujita, K. Akagi, M. Chen, *Angew. Chem. Int. Ed.* **2013**, *52*, 1664-1667.

15. Y. He, W. Chen, X. Li, Z. Zhang, J. Fu, C. Zhao, E. Xie, *ACS Nano* **2013**, *7*, 174-182.

16. L. Hu, W. Chen, X. Xie, N. Liu, Y. Yang, H. Wu, Y. Yao, M. Pasta, H. Alshareef, Y. Cui, *ACS Nano* **2011**, *5*, 8904-8913.

17. M. F. El-Kady, M. Ihns, M. Li, J. Y. Hwang, M. F. Mousavi, L. Chaney, A. T. Lech, R. B. Kaner, *Proc. Natl. Acad. Sci. U.S.A.* **2015**, *112*, 4233-4238.

18. C. Zhu, T. Liu, F. Qian, T. Han, E. Duoss, J. Kuntz, C. Spadaccini, M. Worsley, Y. Li, *Nano Lett.* **2016**, *16*, 3448-3456.

19. C. Zhu, T. Y. Han, E. B. Duoss, A. M. Golobic, J. D. Kuntz, C. M. Spadaccini, M. A. Worsley, *Nat. Commun.* **2015**, *6*, 6962.

20. H. Sun, Z. Xu, C. Gao, *Adv. Mater.* **2013**, *25*, 2554-2560.

21. J. Yang, L. Lian, H. Ruan, F. Xie, M. Wei, *Electrochimica Acta* **2014**, *136*, 189-194.

22. P. Lv, Y. Feng, Y. Li, W. Feng, *J. Power Sources* **2012**, *220*, 160-168.

23. T. Zhai, X. Lu, H. Wang, G. Wang, T. Mathis, T. Liu, C. Li, Y. Tong, Y. Li, *Nano Lett.* **2015**, *15*, 3189-3194.

24. B. Yao, L. Yuan, X. Xiao, J. Zhang, Y. Qi, J. Zhou, J. Zhou, B. Hu, W. Chen, *Nano Energy* **2013**, *2*, 1071-1078.

25. T. Lin, I. Chen, F. Liu, C. Yang, H. Bi, F. Xu, F. Huang, *Science* **2015**, *350*, 1508-1513.

26. B. Yao, L. Huang, J. Zhang, X. Gao, J. Wu, Y. Cheng, X. Xiao, B. Wang, Y. Li, J. Zhou, *Adv. Mater.* **2016**, *28*, 6353-6358.

27. L. Yuan, B. Yao, B. Hu, K. Huo, W. Chen, J. Zhou, *Energy Environ. Sci.* **2013**, *6*, 470-476.

28. X. Yang, C. Cheng, Y. Wang, L. Qiu, D. Li, *Science* **2013**, *341*, 534-537.

29. T. Zhai, F. Wang, M. Yu, S. Xie, C. Liang, C. Li, F. Xiao, R. Tang, Q. Wu, X. Lu, Y. Tong, *Nanoscale* **2013**, *5*, 6790-6796.

30. X. Xiao, X. Peng, H. Jin, T. Li, C. Zhang, B. Gao, B. Hu, K. Huo, J. Zhou, *Adv. Mater.* **2013**, *25*, 5091-5097.

31. J. Wu, X. Gao, H. Yu, T. Ding, Y. Yan, B. Yao, X. Yao, D. Chen, M. Liu, L. Huang, *Adv Funct Mater* **2016**, *26*, 6114-6120.

32. D. Feng, T. Lei, M. Lukatskaya, J. Park, Z. Huang, M. Lee, L. Shaw, S. Chen, A. Yakovenko, A. Kulkarni, J. Xiao, K. Fredrickson, J. Tok, X. Zou, Y. Cui, Z. Bao, *Nat. Energy* **2018**, *3*, 30-36.

33. R. Vinny, K. Chaitra, K. Venkatesh, N. Nagaraju, N. Kathyayini, *J. Power Sources* **2016**, *309*, 212-220.

34. Y. Xia, T. S. Mathis, M.-Q. Zhao, B. Anasori, A. Dang, Z. Zhou, H. Cho, Y. Gogotsi, S. Yang, *Nature* **2018**, *557*, 409-412.

35. M. Zhang, X. Yu, H. Ma, W. Du, L. Qu, C. Li, G. Shi, *Energy Environ. Sci.* **2018**, *11*, 559-565.

36. Y. Wang, Y.-Z. Zhang, D. Dubbink, J. E. ten Elshof, *Nano Energy* **2018**, *49*, 481-488.

37. H. Hu, Z. Pei, H. Fan, C. Ye, *Small* **2016**, *12*, 3059-3069.

38. C. Chen, Y. Zhang, Y. Li, J. Dai, J. Song, Y. Yao, Y. Gong, I. Kierzewski, J. Xie, L. Hu, *Energy Environ. Sci.* **2017**, *10*, 538-545.

39. M. Nakayama, S. Osae, K. Kaneshige, K. Komine, H. Abe, *J. Electrochem. Soc.* **2016**, *163*, A2340-A2348.

40. M. El-Kady, V. Strong, S. Dubin, R. Kaner, *Science* **2012**, *335*, 1326-1330.

41. X. Lu, G. Wang, T. Zhai, M. Yu, S. Xie, Y. Ling, C. Liang, Y. Tong, Y. Li, *Nano Lett.* **2012**, *12*, 5376-5381.

42. Y. Cheng, L. Huang, X. Xiao, B. Yao, L. Yuan, T. Li, Z. Hu, B. Wang, J. Wan, J. Zhou, *Nano Energy* **2015**, *15*, 66-74.

43. Y. Song, T. Y. Liu, B. Yao, T. Y. Kou, D. Y. Feng, X. X. Liu, Y. Li, *Small* **2017**, *13*, 1700067-1700073.

44. Gregg, S., and Sing K. (**1982**) Adsorption, Surface Area, and Porosity (Academic Press)

Chapter 7

Surface Functionalization Boosting the Capacitance of 3D Printed Graphene Aerogels

Abstract

The performances of pseudocapacitive electrodes at fast charging rates are typically limited by the slow kinetics of faradaic reactions and sluggish ion diffusion in the bulk structure. This is particularly problematic for thick electrodes and electrodes highly loaded with active materials. Here we present a surface functionalized 3D printed graphene aerogel (SF-3D GA) that achieves not only a benchmark areal capacitance of 2195 mF cm^{-2} at a high current density of 100 mA cm^{-2} but also an ultrahigh intrinsic capacitance of 309.1 μF cm^{-2} even at a high mass loading of 12.8 mg cm^{-2}. Importantly, kinetic analysis revealed that the capacitance of SF-3D GA electrode is primarily (93.3%) contributed from fast kinetic processes. This is because the 3D printed electrode has an open structure that ensures excellent coverage of functional groups on carbon surface and facilitates the ion accessibility of these surface functional groups even at high current densities and large mass loading/electrode thickness. An asymmetric device assembled with SF-3D GA as anode and 3D printed GA decorated with MnO_2 as cathode achieves a remarkable energy density of 0.65 mWh cm^{-2} at an ultrahigh power density of 164.5 mW cm^{-2}, outperforming carbon-based supercapacitors operated at the same power density.

7.1 Introduction

3D printing technologies have been extensively used in different research fields such as energy storage devices,[1-6] catalysis,[7-8] electronics,[9-10] microfluidics[11-13] and biotechnology[14-16]. These printing technologies have enabled the creation of unique material and device structures that cannot be achieved by conventional methods.[17-18] Moreover, by exploring new complex architectures, these 3D printed materials can achieve novel and/or improved functionality. Direct ink writing (DIW) is one of the most commonly used 3D printing techniques. It offers great flexibility in the material (ink) selection[3, 19] and has been recently applied to prepare electrodes for electrochemical energy storage devices, including lithium-ion batteries,[6, 20-22] sodium-ion batteries,[23] lithium-sulfur batteries,[24] lithium metal batteries,[18] and supercapacitors[25-28]. In comparison to bulk electrodes, these 3D printed electrodes have shown improved electrolyte infiltration and ion diffusion.[17, 29-30]

Carbons are attractive active materials for supercapacitors because most of them are inexpensive and highly conductive. Charges are typically stored on carbon electrodes by forming an electric double layer in an electrolyte. It enables ultrafast charging/discharging rate and outstanding cycling stability, while the capacitance of carbon-based electrodes is ultimately limited by their surface area.[31-34] A strategy commonly used to increase the capacitance is decorating the carbon structures with pseudocapacitive materials, such as metal oxides and conjugated polymers.[35-41] These composite structures typically show significantly enhanced capacitance at slow charging rates. However, their performance at fast charging rates is limited by the slow kinetics of faradaic reactions and sluggish ion diffusion in the bulk electrode structure.[42] This is particularly problematic for thick electrodes and electrodes with high mass loading of active materials.

Here we present a new surface functionalized 3D printed graphene aerogel (SF-3D GA) electrode that achieves not only a benchmark areal capacitance of 2195 mF cm^{-2} at a high current density of 100 mA cm^{-2} but also an ultrahigh intrinsic capacitance of 309.1 μF cm^{-2}, even at a high mass loading of 12.8 mg cm^{-2}. Importantly, the kinetic analysis revealed that the capacitance of SF-3D GA electrode is primarily (93.3%) attributed to fast kinetic processes. This work demonstrates the role of 3D printed structure in boosting the kinetics and intrinsic capacitance of pseudocapacitive GA.

7.2 Experimental Section

Inks Preparation. The GO ink was prepared by ultra-sonicating 0.800 g single-layer GO sheets (lateral dimension, 300-800 nm, Cheaptubes, Inc.) in 20.000 g MilliQ water for 24 h in a sonication bath with the temperature maintained at 12 ºC. The concentration of the GO ink is 40.0 mg/mL. The suspension was then mixed with 5.0 wt% of hydroxypropyl methylcellulose (DOW Chemical, Inc.) in a Thinky planetary mixer at 2000 rpm for 5 min.

3D Printing. The prepared GO ink was loaded into a 3 mL syringe barrel (EFD) and centrifuged at 4500 rpm for 1 minute to remove air bubbles. Then the ink was extruded through a micro nozzle (400 μm diameter) to pattern 3D structures on a glass structure. For direct ink writing, the syringe was attached to a smooth-flow tapered nozzle (400 μm diameter) by a Luer lock. The ink was then extruded by means of an air-powered fluid dispenser (Ultimus V, EFD) under a pressure of 15-20 psi. The writing speed was kept at 5 mm/s for all the 3D printed structures. Simple cubic lattices with multiple orthogonal layers of parallel cylindrical rods were printed alternately. The diameter of the cylindrical rods equals the diameter of the nozzle and the center-to-center rod spacing is 800 μm. The height of the 3D printed electrodes was varied from 1 to 4 mm with a z spacing of 240 μm. The 3D printed structures were immersed in liquid nitrogen soon after printing to avoid the evaporation of water, which would result in cracking and drying of the structures. Then the structures were freeze-dried for 48 h in a vacuum to form aerogels. The as-prepared aerogels were then annealed in a nitrogen atmosphere under a tube furnace at 1050 ºC for 3 h with a heating and cooling rate of 2 ºC/min to form graphene aerogels. This high-temperature annealing process was used to convert 3D printed graphene oxide aerogels to highly conductive graphene aerogels, which then can be used as a conductive scaffold to ensure fast electron transport during fast charging and discharging as well as achieving uniform surface functionalization.

In-situ Functionalization of 3D printed Graphene Aerogels. Electrochemical activation was used to functionalize the 3D printed graphene aerogels. The activation was carried out in 0.5 M KNO_3 electrolyte at a potential of 1.9 V for 3 h under a conventional three-electrode system, which a 3D printed graphene aerogel works as working electrode, saturated calomel electrode (SCE) as reference electrode and graphite foil as the counter electrode, respectively. This electrochemical oxidization introduced oxygen-containing groups on the conductive graphene aerogel surface. Then, the electrochemical oxidized 3D printed graphene aerogel was immersed into 20 mL 0.1 % hydrazine hydrate (20 μL) at 50 ºC for 1 h. The reduction in hydrazine solution was used to remove unstable surface functionalities and recover the conductivity of the graphene aerogel electrode.[1] The as-prepared electrode was then washed with deionized water and ethanol to remove any impurities. The functionalization of the non-3D printed graphene aerogels follows the same manner as to the 3D printed graphene aerogels.

Deposition of MnO_2 Nanosheets on 3D Printed Graphene Aerogels. MnO_2 nanosheets were electrodeposited on 3D printed graphene aerogels under a constant current density of 10 mA cm^{-2} in a three-electrode electrolytic cell using 0.1 M manganese acetate aqueous solution as the electrolyte. The freestanding 3D printed graphene aerogel, graphite foil and SCE were used as working electrode, counter electrode, and reference electrode, respectively.

Fabrication of Asymmetric Devices. Asymmetric supercapacitor devices were fabricated by using SF-3D GA as a negative electrode, and 3D printed GA/MnO_2 as a positive electrode. As shown in Figure S12, the two electrodes are separated apart to avoid short circuit.

The charge stored in the positive and the negative electrode should be balanced according to the relationship $q^+=q^-$. The charge stored in each electrode depends on the areal capacitance (C_A), potential range for the charging/discharging processes (ΔU), and the area of the electrode (A), as shown in the following equation

$$q = C_A * \Delta U * A$$

To achieve $q^+ = q^-$ at 5 mA/cm^2, the areal capacitance can be balanced as follows:

$$\frac{C_A^+}{C_A^-} = \frac{\Delta U^- * A^-}{\Delta U^+ * A^+} = \frac{1*0.2}{1*0.2} = 1$$

where both ΔU^+ and ΔU^- are 1 V. Both A^+ and A^- are 0.2 cm^2.

The required areal capacitances for 2 mm-thick and 4-mm thick positive electrodes are 1.583 F/cm^2 and 3.231 F/cm^2 at 5 mA/cm^2, respectively. Due to the nearly linear relationship of areal capacitance with the deposition time and mass loading of MnO_2 on the 3D GA as reported previously.[5] The MnO_2 deposition time for the 2 mm-thick and 4-mm thick positive electrodes were adjusted to obtain the mass loadings of 6.0 mg/cm^2 and 12.0 mg/cm^2, respectively.

Materials Characterization: The structural properties of the materials were studied by a field emission SEM (FEI Quanta 3D FEG dual beam) and TEM (JEM, 2010-HR). The chemical composition of the functional groups was investigated by XPS (ESCALab) and FTIR spectroscopy (Nicolet/Nexus 670), Raman spectroscopy (Renishaw inVia). Textural properties were examined by Brunauer-Emmett-Teller methods using a JW-BK200C (JWGB SCI. & TECH) surface area analyzer via nitrogen porosimetry.

The electrochemical performance of electrode materials was measured in a three-electrode configuration using electrochemical workstations (CHI 660D and BioLogic EC-Lab SP-300). The 3D printed GA and non-3D printed GA with a geometric area of 0.2 cm^2 were used as working electrodes. SCE and graphite foil were used as reference electrode and counter electrode, respectively. All the electrochemical measurements were performed in a 3.0 M LiCl solution at room temperature. Asymmetric supercapacitor devices were fabricated by assembling activated 3D printed GA as negative electrode and 3D printed GA/MnO_2 as positive electrode.

Calculations: The areal capacitance (C_A), gravimetric capacitance (C_G) and volumetric capacitance (C_V) of single electrodes were calculated based on the galvanostatic charging and discharging curves using Equation 1, Equation 2 and Equation 3, respectively.

$$C_A = \frac{I\times t}{\Delta U\times A} \text{ (Equation 1)}$$

$$C_G = \frac{I\times t}{\Delta U\times m} \text{ (Equation 2)}$$

$$C_V = \frac{I\times t}{\Delta U\times V} \text{ (Equation 3)}$$

here C_A, C_G and C_V are the areal, gravimetric and volumetric capacitance (F cm^{-2}, F g^{-1} or F cm^{-3}), ΔU is the potential window (V), I is the discharge current (A), t is the discharge time (s), m is the mass loading of the materials on the electrodes (g), A is the geometric electrode working area (cm^2) and V is the volume of the electrodes (cm^3). For the asymmetric supercapacitor devices, m is the total mass of two electrodes (g), A is the geometric electrode working area (cm^2) and V is the volume of the two electrodes (cm^3).

The areal energy density (E, mWh cm^{-2}) and power density (P, mW cm^{-2}) of the asymmetric device are calculated using the following equations:

$$E_A = \frac{1000}{2\times 3600} C_A U^2 \text{ (Equation 4)}$$

$$P_A = \frac{3600 \times E_A}{t} \qquad \text{(Equation 5)}$$

Where C_A is the areal capacitance (F cm^{-2}), U is the working voltage (V) and t is the discharging time (s) measured in the galvanostatic charging and discharging experiments.

The gravimetric energy density (E, Wh kg^{-1}) and power density (P, W kg^{-1}) of the asymmetric device are calculated using the following equations:

$$E_G = \frac{1000}{2 \times 3600} C_G U^2 \text{ (Equation 6)}$$

$$P_G = \frac{3600 \times E_G}{t} \qquad \text{(Equation 7)}$$

Where C_G is the gravimetric capacitance (F g^{-1}), U is the working voltage (V) and t is the discharging time (s) measured in the galvanostatic charging and discharging experiments.

The volumetric energy density (E, mWh cm^{-3}) and power density (P, mW cm^{-3}) of the asymmetric device are calculated using the following equations:

$$E_V = \frac{1000}{2 \times 3600} C_V U^2 \text{ (Equation 8)}$$

$$P_V = \frac{3600 \times E_V}{t} \qquad \text{(Equation 9)}$$

Where C_V is the volumetric capacitance (F cm^{-3}), U is the working voltage (V) and t is the discharging time (s) measured in the galvanostatic charging and discharging experiments.

Kinetics Analysis: There are three charge storage mechanisms: the non-faradaic contribution from the formation of electric double layer, the faradaic contribution (pseudocapacitance) from charge-transfer processes of surface atoms, and the ion insertion process.[2] The first two charge storage processes are fast-kinetic processes, which are not limited by ion diffusion. The ion insertion process is a diffusion-controlled process.[2-5]

Cyclic voltammetry can provide a great insight into the difference in charge storage kinetics. By analyzing the current dependence on the sweep rate, v, the nature of the kinetic processes of the electrode materials can be obtained. Both equations of $i = kv^b$ and $i = k_1 v + k_2 v^{0.5}$ can be used to determine the kinetic behavior.

For the equation of $i = kv^b$, both k and b are adjustable parameters, with b-value determined from the slope of log i vs. log v. There are two well-defined conditions: $b=0.5$ and $b=1$. For the $b=0.5$, the current is proportional to the square root of the scan rate, v, according to the following equation[6]:

$$i = nFAC^{*}D^{1/2}v^{1/2}(\alpha nF/RT)^{1/2}\pi^{1/2}\chi(bt) \quad \text{(Equation 10)}$$

where C^* is the surface concentration of the electrode material, α is the transfer coefficient, D is the chemical diffusion coefficient, n is the number of electrons involved in the electrode reaction, A is the surface area of the electrode material, F is the Faraday constant, R is the molar gas constant, T is the temperature, and the $\chi(bt)$ function is the normalized current for a totally irreversible system as indicated by the cyclic voltammetry response. The current response in Equation 10 is diffusion controlled, which is indicative of a faradaic intercalation process.

$b=1$ represents a capacitive response because the capacitive current is proportional to the sweep rate, according to the following equation[4]:

$$i = vC_dA \quad \text{(Equation 11)}$$

where C_d is the capacitance.

Under different potentials, the b value can vary between 0.5 to 1, depending on the specific potential required the faradaic reactions. The values of b determined by equation $i = kv^b$ can tell whether an electrochemical process is dominated by a capacitive process or diffusion-controlled process, but it is unable to quantify the contribution from each process.

Equation 12 ($i = k_1 \nu + k_2 \nu^{0.5}$) can further distinguish the fraction of current contributed from the surface capacitive effects and diffusion-controlled insertion processes by determining the values of k_1 and k_2. $k_1 \nu$ and $k_2 \nu^{1/2}$ correspond to the current contributions from the fast-kinetic processes (surface capacitive process) and the show-kinetic processes (diffusion-controlled intercalation process), respectively.

We used a method reported by Prof. Bruce Dunn's group to quantify the capacitance contribution from fast-kinetic processes and slow-kinetic processes.[2][3] First, the current density at a fixed potential and scan rate, i, was extracted from the CV curves. The current density, i, is a function of scan rate, v, and can be expressed as the sum of two items v:

$$i = k_1 \nu + k_2 \nu^{0.5} \quad \text{(Equation 12)}$$

where k_1 and k_2 are constants. $k_1 \nu$ and $k_2 \nu^{0.5}$ represent the current contribution of fast kinetic (or capacitive-controlled) process and slow kinetic (or diffusion-controlled) process, respectively. Dividing $\nu^{0.5}$ into both sides of Equation (1) gives:

$$i\nu^{-0.5} = k_1 \nu^{0.5} + k_2 \quad \text{(Equation 13)}$$

By plotting $i\nu^{-0.5}$ as a function of $\nu^{0.5}$, we can determine k_1 (slope) and k_2 (y-axis intercept). The calculation was repeated for each potential to determine the contribution from fast kinetic and slow kinetic processes.

The ion diffusion resistance (σ) was determined from a plot of the real part of impedance (Z’) in the EIS spectrum as a function of the square root of frequency ($\omega^{-0.5}$) in the intermediate frequency range. The slopes of the linear fitting line of this plot are the values of the ion diffusion resistance, which is also called Warburg coefficient.

7.3 Results and Discussions

The fabrication process of SF-3D GA is depicted in Scheme 7.1. The graphene oxide (GO) ink prepared by mixing 40 mg mL^{-1} single-layer GO sheets with 5.0 wt% hydroxypropyl methylcellulose was extruded through a micro nozzle of 400 μm diameter to print a lattice structure with multiple orthogonal layers of parallel cylindrical rods. The 3D printed structures were freeze dried and annealed at 1050 ºC to convert GO aerogels into graphene aerogels. The graphene aerogels were then electrochemically oxidized in 0.5 M KNO_3 solution at a potential of 1.9 V *vs.* saturated calomel electrode (SCE) for 3 h to introduce surface functional groups.[43-44] Finally, the surface functionalized 3D GA was further reduced in 0.1% hydrazine hydrate solution at 50 ºC for 1h to improve its electrical conductivity.

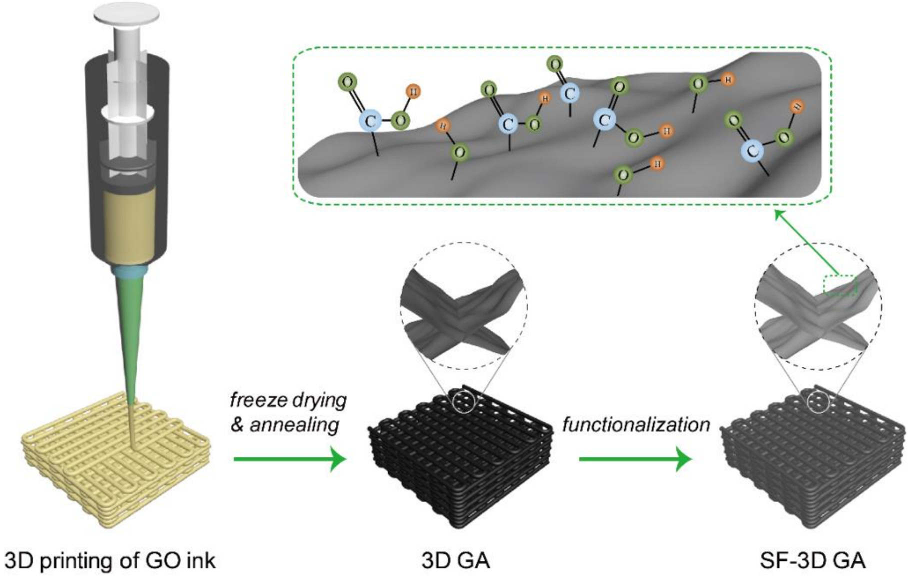

Scheme 7.1 Schematic illustration of preparing SF-3D GA.

The structural properties of GAs before and after surface functionalization were characterized by electron microscopy studies. Scanning electron microscopy (SEM) images showed that the diameter of the cylindrical rod and center-to-center rod spacing are around 400 μm and 800 μm, respectively (Figure 7.1a). Each cylindrical rod is composed of graphene nanosheets with thickness of tens of nanometer (Figure 7.1c and e). Notably, the electrochemical oxidation process did not change the 3D printed structure and nanosheets' morphology (Figure 7.1b, d and f). On the other hand, high-resolution transmission electron microscopy (TEM) images revealed that the crystallinity of graphene nanosheets decreased after electrochemical oxidation (Figure 7.1g-h). Some mesopores were also formed. Selected area electron diffraction (SAED) patterns confirmed the amorphous nature of the oxidized graphene nanosheets (Figure 7.1g-h insets). The two diffraction rings shown in Figure 7.1g inset are corresponding to the (002) and (100) facets of the hexagonal carbon (JCPDS No. 75-1621). Contact angle test further showed that the 3D GA changed from hydrophobic with a contact angle of 140° to super-hydrophilic with a contact angle of 0° after surface functionalization (Figure 7.1g-h insets). TEM elemental mapping analysis showed that the surface functionalized graphene nanosheet contains only C and O elements (Figure 7.1i), suggesting the surface is covered with oxygen containing species. According to the nitrogen adsorption/desorption measurement, the surface area of the 3D GA only slightly increased from 78.3 m^2 g^{-1} to 81.7 m^2 g^{-1} (Figure 7.1j) after surface functionalization. The SF-3D GA has a larger amount of mesopores with a width between 4-8 nm (Figure 7.1j inset), which is consistent with the TEM results.

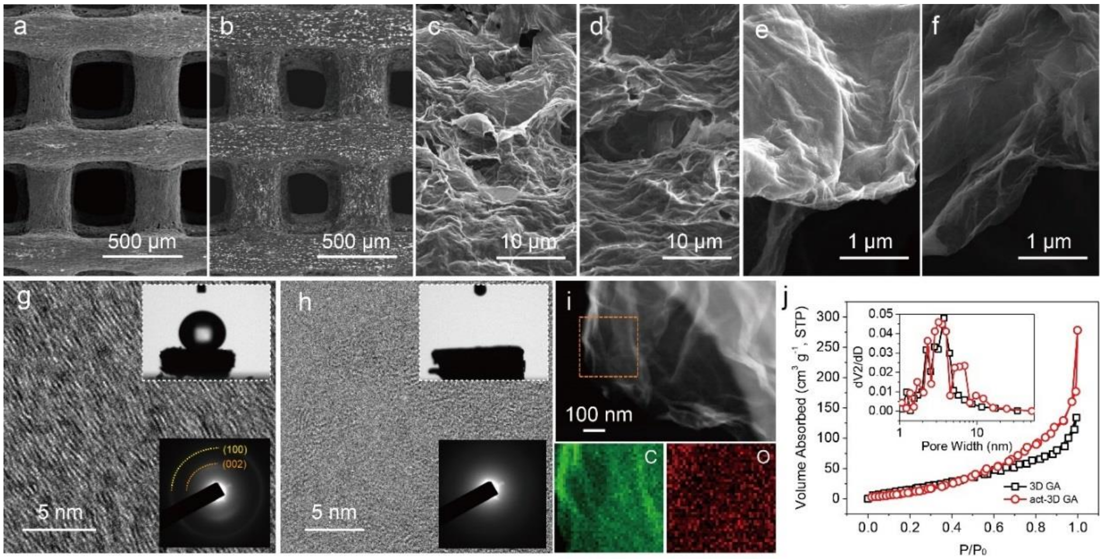

Figure 1. SEM images of the 3D GA (a, c, e) and SF-3D GA (b, d, f). TEM images and corresponding SAED patterns (bottom insets) of the (g) 3D GA and (h) SF-3D GA. The upper insets show the water droplet on the surface of the two GAs. (i) High angle annular dark field scanning transmission electron microscopy image of a

surface functionalized GA nanosheet and its corresponding X-ray dispersive spectroscopy (EDS) mapping images of carbon and oxygen elements. (j) Nitrogen adsorption/desorption isotherms of the 3D GA and SF-3D GA. Inset shows the pore size distribution plots of the two samples.

The chemical composition of 3D GAs and SF-3D GAs were analyzed by different spectroscopic techniques. In comparison to 3D GAs, the SF-3D GA exhibits stronger infrared absorption peaks at 3429 cm^{-1} and 1169 cm^{-1}, indicating a substantial increase of C-OH (hydroxyl) groups (Figure 7.2a).[45] The increased peak intensity at 1576 cm^{-1} can be attributed to the $O=C-O^-$ group and the C-C stretching mode.[46] The extra peak at 1716 cm^{-1} observed in the spectrum of SF-3D GA can be assigned to C=O stretching vibration in O=C-OH (carboxyl) and C=O (carbonyl) groups.[45, 47] The FTIR results confirmed the successful introduction of oxygen-containing groups onto 3D GA surface. Graphene typically shows two strong peaks at 1350 cm^{-1} (D band) and 1580 cm^{-1} (G band) in a Raman spectrum, where D band represents the presence of defects in the graphitic lattice with A_{1g} symmetry, while the G band is associated with the in-plane E_{2g} mode of single crystalline graphitic carbon atoms in the honeycomb lattice.[48] The increased I_D/I_G ratio from 0.95 (3D GA) to 1.28 (SF-3D GA) suggests the increase of surface disorder (Figure 7.2b),[49] consistent with the increased amorphous nature of SF-3D GA. The chemical composition of 3D GAs and SF-3D GAs were further probed by X-ray photoelectron spectroscopy (XPS). As shown in Figure 7.2c, the SF-3D GA exhibits a significantly broader shoulder peak in the core-level C 1s spectrum. This shoulder peak can be deconvoluted into three peaks, corresponding to C-OH (286.2 eV), C=O (284.5 eV) and O=C-OH (289 eV) groups.[50-52] Likewise, SF-3D GA has a broader O 1s peak, which can also be deconvoluted into peaks corresponding to O=C-OH (533.4 eV), C=O (532.4 eV) and C-OH (531.2 eV) groups, in agreement with the C 1s XPS results (Figure 7.2d).[49, 51, 53] Furthermore, the oxygen ratio (defined as O/(C+O), where C and O represents the number of carbon and oxygen atoms) calculated from XPS survey spectra increased substantially from 3.8 % (3D GA) to 17.6 % (SF-3D GA), again confirming the successful functionalization of oxygen-containing groups on the graphene sheets.

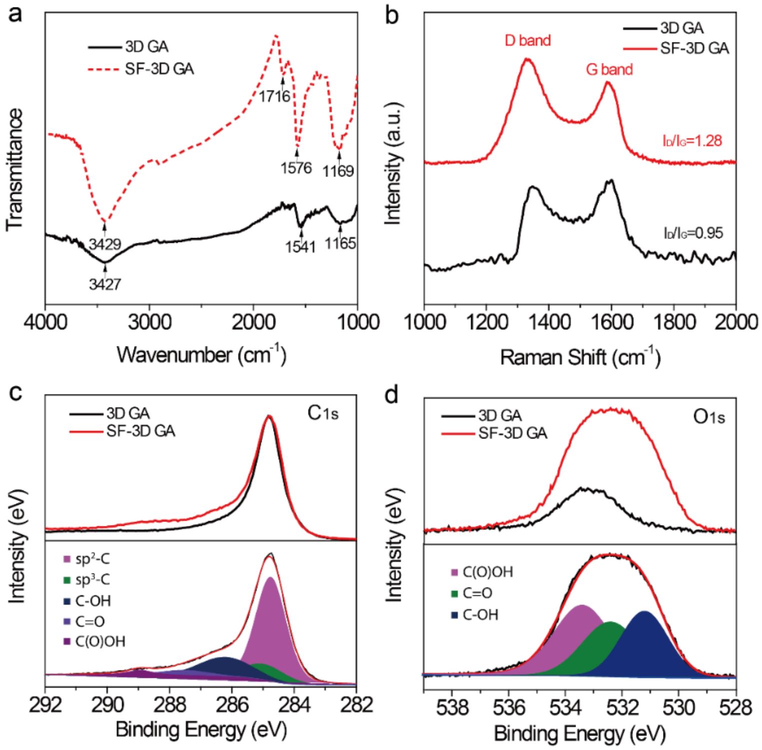

Figure 7.2 (a) FTIR spectra, (b) Raman spectra, (c) core-level C 1s XPS spectra, and (d) core-level O 1s spectra of the 3D GA and SF-3D GA. The bottom figures in (c) and (d) respectively show the deconvoluted peaks of C1s and O1s spectra of the SF-3D GA.

The electrochemical performance of 3D GA and SF-3D GA electrodes were studied in a three-electrode cell using a 3M LiCl solution as the electrolyte, a saturated calomel electrode (SCE) and a piece of graphite foil as the reference and counter electrode, respectively. To investigate the effect of 3D printed structure on the electrode's performance, a non-3D printed GA electrode was surface functionalized and tested under the same conditions as a control sample (denoted as SF-GA). In comparison to 3D GA, both SF-GA and SF-3D GAs showed substantially increased area in their cyclic voltammograms (CV) (Figure 7.3a), proving that the surface functionalization is highly effective in enhancing the charge storage capability of GAs. The SF-3D GA also showed typical capacitive behavior with a highly rectangular shape of CV and isosceles triangular galvanostatic charging-discharging (GCD) profiles (Figure 7.3b), suggesting the electron transport and ion diffusion in the structure are highly efficient.

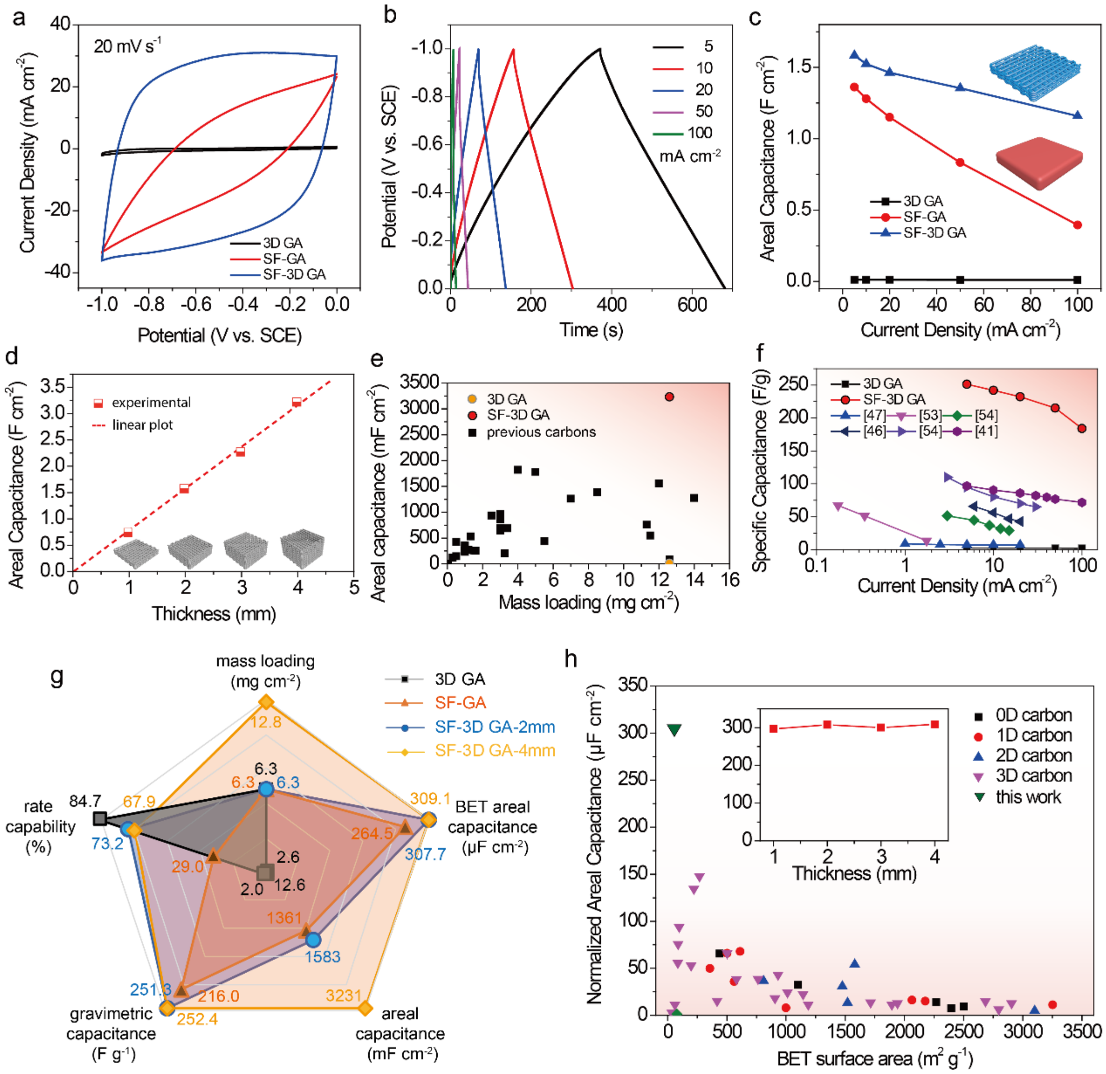

Figure 7.3 (a) Cyclic voltammograms of 3D GA, SF-GA and SF-3D GA. All these electrodes are 2 mm thick and have a mass loading of 6.3 mg cm^{-2}. (b) GCD curves of the SF-3D GA. (c) Areal capacitances of 3D GA, SF-GA and SF-3D GA obtained at different current densities. (d) Areal capacitances of SF-3D GA electrodes obtained at 5 mA cm^{-2} are plotted as a function of electrode thickness. (e) A plot compares the areal capacitance of the 3D GA and SF-3D GA with the values previously reported for carbon electrodes. (f) A plot compares the specific capacitance of 3D GA and SF-3D GA with other high mass loading supercapacitor electrodes, activated CC,[50] rGO paper,[54] Bi_2O_3/CNF,[55] activated CC',[49] MnO_2/CNF,[55] tri-layered graphite[44]. (g) A

radar chart compares the five figure-of-merits of 3D GA, SF-GA and SF-3D GAs: mass loading of the electrode materials, rate capability (from 5 mA cm^{-2} to 100 mA cm^{-2}), gravimetric capacitance, areal capacitance based on geometric area and BET surface area. All capacitances were obtained at 5 mA cm^{-2}. (h) A plot compares the intrinsic capacitance (gravimetric capacitance normalized to the BET surface area) of the SF-3D GA with the values previously reported for 0D, 1D, 2D and 3D carbon materials.

The SF-3D GA achieved an areal capacitance of 1583.2 mF cm^{-2} (volumetric capacitance of 7.92 F/cm^3) at 5 mA cm^{-2}, which is 125-fold higher than that of 3D GA (12.6 mF cm^{-2}, 0.063 F/cm^3) obtained at the same current density. It also retained a high capacitance of 1159.2 mF cm^{-2} (5.8 F/cm^3) when the current density increased to 100 mA cm^{-2}, showing excellent rate capability. In contrast, the capacitance of the SF-GA dropped drastically with the increase of current density. This comparison confirms the importance of having a 3D printed porous structure that allows rapid ion diffusion and provides a large ion accessible area even at fast charging rates. Significantly, the advantage of the 3D printed structure is also evidenced by the linear relationship between areal capacitance and electrode thickness (Figure 7.3d). The 4-mm thick SF-3D GA with a high mass loading of 12.8 mg cm^{-2} yielded an exceptionally high areal capacitance of 3231 mF cm^{-2} at 5 mA cm^{-2}, which is much higher than the values reported for other carbon-based electrodes, such as activated carbon cloth (88 mF cm^{-2}),[50] 3D printed hierarchical macroporous graphene aerogels (206.7 mF cm^{-2}),[28] 3D printed carbon aerogels (645 mF cm^{-2})[56] and activated carbon fibers (1385 mF cm^{-2})[57]. To our knowledge, this is the best value reported for a free-standing carbon-based supercapacitor electrode (Figure 7.3e). This remarkable areal capacitance is a result of the combination of large electrode thickness and high loading of active mass per unit area. Most importantly, even under such a high mass loading, the 4-mm thick SF-3D GA still achieved an excellent gravimetric capacitance of 252.4 F g^{-1} at 5 mA cm^{-2} and 171.5 F g^{-1} at a very high current density of 100 mA cm^{-2} (Figure 7.3f). The gravimetric capacitances and excellent rate capability of SF-3D GA electrodes are significantly higher than that of 3D GA (2.46 F g^{-1} at 5 mA cm^{-2}, with the mass loading of 12.8 mg cm^{-2}), and other carbon-based electrodes with similar mass loading (Figure 7.3f).[44, 49-50, 54-55] The results imply that most of the active material in the thick SF-3D GA electrode were utilized for charge storage even at high charging rates. The 3D printed lattice structure allows great ion accessible area per unit mass in the SF-3D GA.

It is noteworthy that SF-3D GAs show excellent areal and gravimetric capacitances, while they have a relatively small surface area (~82 m^2 g^{-1}). The surface functionalization process only slightly increased the surface area of 3D GA, the substantially enhanced capacitances are therefore not likely due to the increase of electric double layer capacitance but the increased contribution of pseudocapacitance from the surface functional groups.[58-59] The redox reactions of the oxygen-containing groups on the graphene aerogel surface are:[60]

$$^{*}\mathrm{C=O} + \mathrm{H^{+}} + \mathrm{e^{-}} \leftrightarrow {}^{*}\mathrm{C-OH} \quad (1)$$

$$^{*}\mathrm{COO} + \mathrm{H^{+}} + \mathrm{e^{-}} \leftrightarrow {}^{*}\mathrm{COOH} \quad (2)$$

$$^{*}\mathrm{C=O} + \mathrm{e^{-}} \leftrightarrow {}^{*}\mathrm{C-O^{-}} \quad (3)$$

By normalizing gravimetric capacitance to BET surface area, the SF-3D GA achieved an extremely high intrinsic capacitance of 309.1 μF cm^{-2}, which is two orders of magnitude larger than that of 3D GA (2.56 μF cm^{-2}). This value is also much higher than the state-of-the-art carbon materials (5-50 μF cm^{-2})[32, 48, 50, 61-63] and is even comparable to some high mass-loading pseudocapacitive materials, such as mesoporous carbon fiber/MnO_2 (246.3 μF cm^{-2}, 6.8 mg cm^{-2})[64] (Figure 7.3h). The simultaneous achievement of outstanding total capacitance and intrinsic capacitance is attributed to the high ion accessibility of SF-3D GA structure enabled by 3D printing. First, during the surface functionalization (electrochemical oxidation) process, this open electrode structure ensures excellent coverage of functional groups on the carbon surface, maximizing the effectiveness of the functionalization. Second, in the electrochemical measurement, the 3D printed lattice structure also allows easy ion accessibility to the surface functional groups even at high current densities and large mass loading/electrode thickness.

Figure 7.3g shows a radar chart that summaries and compares the five figure-of-merits, i.e. mass loading, gravimetric capacitance, areal capacitance normalized to the geometric surface area, areal capacitance normalized to BET surface area, and rate capability of different GA electrodes we studied. Due to the additional pseudocapacitance contribution from the surface functional groups, the SF-3D GA-2 mm achieved higher areal capacitance and gravimetric capacitance than that of 3D GA-2 mm. Furthermore, the areal capacitance of SF-3D GA is doubled when the electrode thickness increased from 2 mm to 4 mm (amount of active materials is doubled as well), while retaining the same gravimetric capacitance and rate capability. Last, despite the SF-3D GA exhibiting only slightly higher areal and gravimetric capacitances than that of SF-GA under the same mass loadings at low current density, its rate capability is significantly better than SF-GA, again confirming the important role of the 3D printed structure for improving the capacitance of high mass loading electrodes at high current densities.

Given the significant contribution of pseudocapacitance in SF-3D GAs, it is surprising that it can simultaneously achieve high capacitance and an excellent rate capability. Kinetics analysis was performed to better understand the pseudocapacitive behavior of the SF-3D GA electrodes. There are three charge storage mechanisms: the non-faradaic contribution from the formation of electric double layer, the faradaic contribution (pseudocapacitance) from charge-transfer processes of surface species, and the ion insertion process.[3] The first two charge storage processes are fast-kinetic processes, which are not limited by ion diffusion. The ion insertion process is a diffusion-controlled process.[64-67] The cyclic voltammograms of the SF-3D GA were nearly box-shaped, reflecting the rapid electron and ion transport in the electrode (Figure 7.4a). The current density of a supercapacitor electrode, i, scales with the scan rates, ν, following the relationship of $i = k\nu^b$.[58, 67] The power-law exponent, b, is an important indicator to evaluate the charge storage kinetics. b=1 represents the ideal capacitive behavior, while b=0.5 represents battery-type charge storage process. By plotting the logarithm of the absolute current densities against the logarithm of scan rates ($\log i = b \log \nu + k$), the slope is the b-value. For example, the b-value of the anodic current densities obtained at -0.5 V vs. SCE was calculated to be 1.00, suggesting the ideal capacitive behavior and the ultrafast charge storage kinetics (Figure 7.4b). To get a full picture of the charging kinetics of the SF-3D GA electrode, we analyzed the b-values under different potentials for both cathodic and anodic currents (Figure 7.4c). Significantly, all the b-values are close to 1, supporting the fast kinetics in the charging/discharging processes observed for SF-3D GA. The relatively small b values of the cathodic currents (0.77~0.93) imply the kinetic process for charging is less efficient than discharging.

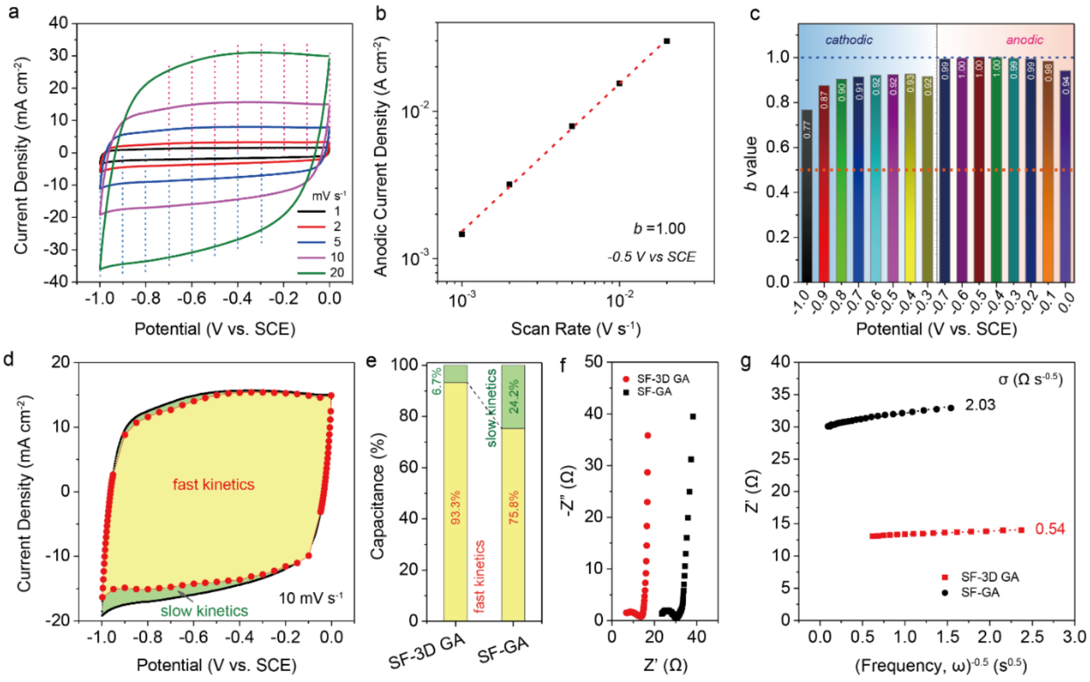

Figure 7.4 (a) Cyclic voltammograms of SF-3D GA collected at various scan rates. The dashed lines highlight the potentials selected for *b* value calculation. (b) A plot of anodic current densities at -0.5 V *vs.* SCE as a function of scan rates. (c) A histogram shows the *b* values calculated from anodic currents (right) and cathodic currents (left) obtained at different potentials. (d) A cyclic voltammogram of SF-3D GA obtained at 10 mV s^{-1} showing the capacitance contribution from the fast-kinetic processes

(yellow) and the slow-kinetic processes (green). (e) The comparison of the capacitance contributions by the fast and slow kinetic processes in the SF-3D GA and SF-GA. (f) Nyquist plots, and (g) Z’ *vs.* the reciprocal of the square root of frequency ($\omega^{-0.5}$) in the intermediate frequency range of the SF-3D GA and SF-GA. The dashed lines are the best fitting lines to calculate the diffusion resistance, σ.

We further analyzed the capacitance contributions from fast and slow kinetic processes.[65, 68] At a fixed potential and scan rate, the current density, *i*, is composed of two terms related to the scan rate, *v*:

$$i = k_1 v + k_2 v^{0.5} \qquad (1)$$

where k_1 and k_2 are constants.[65, 68] $k_1 v$ and $k_2 v^{0.5}$ represent the current contribution of fast kinetic (or capacitive-controlled) process and slow kinetic (or diffusion-controlled) process, respectively. Dividing $v^{0.5}$ on both sides of Equation (1) gives:

$$i v^{-0.5} = k_1 v^{0.5} + k_2 \qquad (2)$$

By plotting $i v^{-0.5}$ as a function of $v^{0.5}$, we can determine k_1 (slope) and k_2 (y-axis intercept). The calculation was repeated for each potential to determine the contribution from fast kinetic and slow kinetic processes. Figure 7.4d shows an example of differentiated cyclic voltammogram of SF-3D GA collected at 10 mV s^{-1}. The capacitance contribution from the fast kinetic process (yellow region) is dominant at all potentials, with a total contribution of 93.3% (Figure 7.4e). This value is much higher than the values reported for other pseudocapacitive materials at the same scan rate, demonstrating the excellent ion accessibility of the SF-3D GA electrode.[64, 69-71] In contrast, the SF-GA only has 75.8% of the capacitance comes from the fast kinetic process. Furthermore, we compared the ion diffusion resistances

(σ) of SF-3D GA and SF-GA obtained in the same electrolyte and at the same potential, the values of σ should be related to the electrode structure and charge storage mechanism. The values of σ were extracted from the slopes of the linear fitting lines of the real part of impedance (Z') versus the reciprocal of the square root of frequency ($\omega^{-0.5}$).[64, 72-73] The SF-3D GA exhibits an ultra-small σ value of 0.54 Ω $s^{-0.5}$, which is only around one fourth of the value of SF-GA (2.03 Ω $s^{-0.5}$) (Figure 7.4e-f). The σ value is impressively small given that the majority of charge is stored through pseudocapacitive reactions. It is even smaller than the values reported for carbon fibers (3.33 Ω $s^{-0.5}$), mesoporous carbon fibers (0.64 Ω $s^{-0.5}$), and most other carbon-based materials.[64, 71, 73] Taken together, these results unambiguously confirmed the critical role of 3D printed periodic porous structure in facilitating ion diffusion and accessibility. The fast kinetics of SF-3D GA makes it a unique and attractive pseudocapacitive electrode for fast-charging devices.

We have recently demonstrated a 3D printed GA structure highly loaded with MnO_2 (denoted as 3D GA/MnO_2) that achieved outstanding capacitance in the positive potential region.[17] Nevertheless, MnO_2 based pseudocapacitive materials have a relatively small potential window in aqueous electrolyte, typically 0.8 V, which limits the energy density of supercapacitor device fabricated with symmetric MnO_2 based electrodes. While the device's voltage window can be broadened by forming an asymmetric supercapacitor (ASC) device via the assembly of two different electrodes, the challenge was to find a negative electrode that can match the large capacitance of 3D GA/MnO_2. The SF-3D GA showed outstanding capacitive performance in the negative potential region (vs. SCE) which makes it an attractive anode material for ASCs. Therefore, we fabricated an ASC device with 3D GA/MnO_2 as cathode and SF-3D GA as anode, denoted as 3D GA/MnO_2//SF-3D GA.

The 3D GA/MnO_2 was prepared by electrodepositing porous MnO_2 nanosheets on 3D GA, as reported elsewhere.[17] 3D GA/MnO_2//SF-3D GA achieved a stable working voltage window of 2 V (Figure 7.5a). The rectangular-like cyclic voltammograms (Figure 7.5a) and symmetric triangular GCD curves (Figure 7.5b) suggest that the ASC device has excellent capacitive behavior and fast charging/discharging properties. The 4-mm thick ASC yields an excellent areal capacitance of 853.3 mF cm^{-2} at a current density of 5 mA cm^{-2}. It was able to retain 72.8% of the capacitance when the current density was increased to 100 mA cm^{-2}. The areal capacitance of the 8-mm thick ASC (1700.6 mF cm^{-2}) is approximately 2 times higher than the 4-mm ASC device, demonstrating its great scalability (Figure 7.5c). Furthermore, the 3D GA/MnO_2//SF-3D GA ASC retained a remarkable 93 % of its initial capacitance after 100,000 charging and discharging cycles at 100 mV s^{-1}, which is more than 46 days of the continuous operation (Figure 7.5d). The excellent durability of these ASC devices was consistent with the results from the GCD tests under high and moderate current densities. The 3D printed structures and nanosheet morphology of both 3D GA/MnO_2 and SF-3D GA electrodes were well preserved after the long-term cycling. The chemical composition of both electrodes also remained unchanged, manifesting their excellent electrochemical stability.

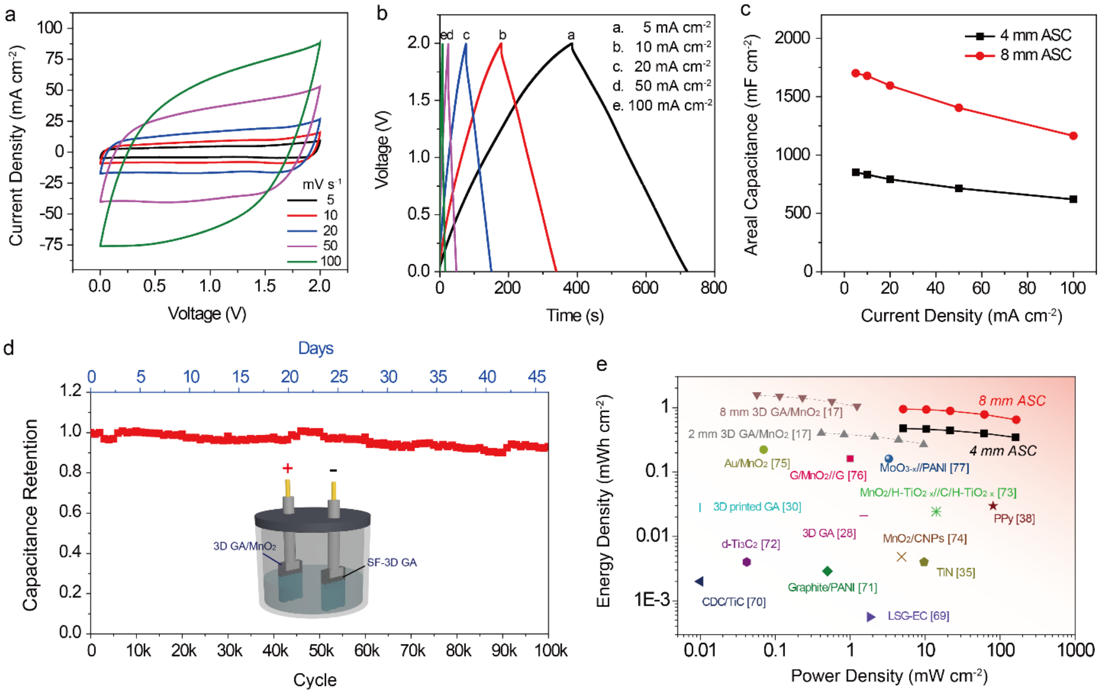

Figure 7.5 (a) Cyclic voltammograms of the 3D GA/MnO$_2$//SF-3D GA device collected at different scan rates. (b) Galvanostatic charging/discharging curves collected for the 3D GA/MnO$_2$//SF-3D GA device at different current densities. (c) Areal capacitances of the 4 mm-thick and 8 mm-thick 3D GA/MnO$_2$//SF-3D GA devices obtained at different current densities. (d) Long-term stability of the 3D GA/MnO$_2$//SF-3D GA device. Inset shows the schematic illustration of the 3D GA/MnO$_2$//SF-3D GA device. (e) Ragone plot of the 3D GA/MnO$_2$//SF-3D GA device. The values reported for other supercapacitor devices (3D GA/MnO$_2$ SSC,[17] LSG-EG SSC,[74] CDC/TiC MSC,[75] Graphite/PANI SSC,[76] d-Ti$_3$C$_2$ SSC,[77] TiN SSC,[37] MnO$_2$/CNPs SSC,[78] 3D GA SSC,[30] 3D-printed GA SSC,[28] PPy SSC,[40] MnO$_2$/H-TiO$_{2-x}$//C/H-TiO$_{2-x}$ ASC,[79] Au/MnO$_2$ MSC,[80] G/MnO$_2$//G ASC,[81] MoO$_{3-x}$/PANI ASC,[82]) are added for comparison. SSC: symmetric supercapacitor; MSC: microsupercapacitor. These values are the highest energy densities reported in each reference.

Notably, the 3D GA/MnO_2//SF-3D GA device achieved an excellent energy density of 0.94 mWh cm^{-2} at the power density of 5.1 mW cm^{-2} and retained an energy density of 0.65 mWh cm^{-2} at a high power density of 164.5 W cm^{-2} (Figure 7.5e). These values are considerably higher than the state-of-the-art supercapacitor devices reported previously.[28, 37, 40, 56, 74-82] In addition, the 3D GA/MnO_2//SF-3D GA device achieved a high specific energy density of 37.0 Wh kg^{-1} (1.19 mWh cm^{-3}) at a specific power density of 397.8 W kg^{-1} (12.7 mW cm^{-3}). It also retained a high specific energy density of 26.9 Wh kg^{-1} (0.86 mWh cm^{-3}) at an ultrahigh specific power density of 12631.4 W kg^{-1} (404.2 mW cm^{-3}), which outperform other carbon-based supercapacitor devices with mass loadings higher than 10 mg cm^{-2}.

7.4 Conclusions

In summary, we have successfully developed a surface functionalized 3D printed graphene aerogel that achieves a record-high areal capacitance for free-standing carbon-based materials. The surface functional groups contribute more than 99 % of the total capacitance. Importantly, a kinetic analysis performed at 10 mV s^{-1} showed that capacitance contribution from fast kinetic process is dominant at all potentials we studied, with a total contribution of 93.3%. This value is much higher than the values reported for other pseudocapacitive materials at the same scan rate. The excellent ion accessibility of the SF-3D GA electrode also leads to an extremely high intrinsic capacitance of 309.1 μF cm^{-2}, which is significantly higher than other carbon-based materials. The ASC device assembled with SF-3D GA as anode and 3D GA/MnO_2 as cathode achieves a remarkable energy density of 0.65 mWh cm^{-2} at an exceptionally high power density of 164.5 mW cm^{-2} in a voltage window of 2 V. This work demonstrates a new design principle to simultaneously achieve high total capacitance and intrinsic capacitance for carbon materials and hold great promise for a broad range of electrochemical applications including batteries, catalysts, fuel cells and desalination devices.

References

1. M. R. Hartings, Z. Ahmed, *Nat. Rev. Chem.* **2019**, *3*, 305-314.
2. H. Sun, J. Zhu, D. Baumann, L. Peng, Y. Xu, I. Shakir, Y. Huang, X. Duan, *Nat. Rev. Mater.* **2019**, *4*, 45-60.
3. C. Zhu, T. Y. Liu, F. Qian, W. Chen, S. Chandrasekaran, B. Yao, Y. Song, E. B. Duoss, J. D. Kuntz, C. M. Spadaccini, M. A. Worsley, Y. Li, *Nano Today* **2017**, *15*, 107-120.
4. K. Fu, Y. Yao, J. Dai, L. Hu, *Adv. Mater.* **2017**, *29,* 1603486-1603505.
5. X. C. Tian, J. Jin, S. Q. Yuan, C. K. Chua, S. B. Tor, K. Zhou, *Adv. Energy Mater.* **2017**, *7*, 1700127.
6. K. Sun, T.-S. Wei, B. Y. Ahn, J. Y. Seo, S. J. Dillon, J. A. Lewis, *Adv. Mater.* **2013**, *25*, 4539-4543.
7. F. Qian, C. Zhu, J. M. Knipe, S. Ruelas, J. K. Stolaroff, J. R. DeOtte, E. B. Duoss, C. M. Spadaccini, C. A. Henard, M. T. Guarnieri, S. E. Baker, *Nano Lett.* **2019**, *19*, 5829-5835.

8. X. Zhou, C.-j. Liu, *Adv Funct Mater* **2017**, *27*, 1701134.

9. J. T. Muth, D. M. Vogt, R. L. Truby, Y. Mengüç, D. B. Kolesky, R. J. Wood, J. A. Lewis, *Adv. Mater.* **2014**, *26*, 6307-6312.

10. Y. L. Kong, I. A. Tamargo, H. Kim, B. N. Johnson, M. K. Gupta, T.-W. Koh, H.-A. Chin, D. A. Steingart, B. P. Rand, M. C. McAlpine, *Nano Lett.* **2014**, *14*, 7017-7023.

11. P. J. Kitson, M. H. Rosnes, V. Sans, V. Dragone, L. Cronin, *Lab Chip* **2012**, *12*, 3267-3271.

12. J. L. Erkal, A. Selimovic, B. C. Gross, S. Y. Lockwood, E. L. Walton, S. McNamara, R. S. Martin, D. M. Spence, *Lab Chip* **2014**, *14*, 2023-2032.

13. S. Waheed, J. M. Cabot, N. P. Macdonald, T. Lewis, R. M. Guijt, B. Paull, M. C. Breadmore, *Lab Chip* **2016**, *16*, 1993-2013.

14. A. Lee, A. R. Hudson, D. J. Shiwarski, J. W. Tashman, T. J. Hinton, S. Yerneni, J. M. Bliley, P. G. Campbell, A. W. Feinberg, *Science* **2019**, *365*, 482-487.

15. B. Derby, *Science* **2012**, *338*, 921-926.

16. B. C. Gross, J. L. Erkal, S. Y. Lockwood, C. Chen, D. M. Spence, *Anal. Chem.* **2014**, *86*, 3240-3253.

17. B. Yao, S. Chandrasekaran, J. Zhang, W. Xiao, F. Qian, C. Zhu, E. B. Duoss, C. M. Spadaccini, M. A. Worsley, Y. Li, *Joule* **2019**, *3*, 459-470.

18. D. Cao, Y. Xing, K. Tantratian, X. Wang, Y. Ma, A. Mukhopadhyay, Z. Cheng, Q. Zhang, Y. Jiao, L. Chen, H. Zhu, *Adv. Mater.* **2019**, *31*, 1807313.

19. P. Chang, H. Mei, S. Zhou, K. G. Dassios, L. Cheng, *J. Mater. Chem. A* **2019**, *7*, 4230-4258.

20. K. Fu, Y. Wang, C. Yan, Y. Yao, Y. Chen, J. Dai, S. Lacey, Y. Wang, J. Wan, T. Li, Z. Wang, Y. Xu, L. Hu, *Adv. Mater.* **2016**, *28*, 2587-2594.

21. R. R. Kohlmeyer, A. J. Blake, J. O. Hardin, E. A. Carmona, J. Carpena-Nunez, B. Maruyama, J. Daniel Berrigan, H. Huang, M. F. Durstock, *J. Mater. Chem. A* **2016**, *4*, 16856-16864.

22. Y. Wang, C. Chen, H. Xie, T. Gao, Y. Yao, G. Pastel, X. Han, Y. Li, J. Zhao, K. Fu, L. Hu, *Adv Funct Mater* **2017**, *27*, 1703140.

23. J. Ding, K. Shen, Z. Du, B. Li, S. Yang, *ACS Appl. Mater. Interfaces* **2017**, *9*, 41871-41877.

24. K. Shen, H. Mei, B. Li, J. Ding, S. Yang, *Adv. Energy Mater.* **2018**, *8*, 1701527.

25. K. Shen, J. Ding, S. Yang, *Adv. Energy Mater.* **2018**, *8*, 1800408.

26. J. Zhao, Y. Zhang, X. Zhao, R. Wang, J. Xie, C. Yang, J. Wang, Q. Zhang, L. Li, C. Lu, Y. Yao, *Adv Funct Mater* **2019**, *29*, 1900809.

27. W. Yang, J. Yang, J. J. Byun, F. P. Moissinac, J. Xu, S. J. Haigh, M. Domingos, M. A. Bissett, R. A. W. Dryfe, S. Barg, *Adv. Mater.* **2019**, *31*, e1902725.

28. C. Zhu, T. Liu, F. Qian, T. Han, E. Duoss, J. Kuntz, C. Spadaccini, M. Worsley, Y. Li, *Nano Lett.* **2016**, *16*, 3448-3456.

29. L. H. Yu, Z. D. Fan, Y. L. Shao, Z. N. Tian, J. Y. Sun, Z. F. Liu, *Adv. Energy Mater.* **2019**, *9*, 1901839.

30. X. Tang, H. Zhou, Z. Cai, D. Cheng, P. He, P. Xie, D. Zhang, T. Fan, *ACS Nano* **2018**, *12*, 3502-3511.

31. P. Simon, Y. Gogotsi, *Nat. Mater.* **2008**, *7*, 845-854.

32. L. L. Zhang, X. S. Zhao, *Chem. Soc. Rev.* **2009**, *38*, 2520-2531.

33. J.-G. Wang, H. Liu, X. Zhang, X. Li, X. Liu, F. Kang, *Small* **2018**, *14*, 1703950.

34. J.-G. Wang, H. Liu, X. Zhang, M. Shao, B. Wei, *J. Mater. Chem. A* **2018**, *6*, 17653-17661.

35. V. Augustyn, P. Simon, B. Dunn, *Energy Environ. Sci.* **2014**, *7*, 1597-1614.

36. B. Yao, L. Huang, J. Zhang, X. Gao, J. Wu, Y. Cheng, X. Xiao, B. Wang, Y. Li, J. Zhou, *Adv. Mater.* **2016**, *28*, 6353-6358.

37. X. Lu, G. Wang, T. Zhai, M. Yu, S. Xie, Y. Ling, C. Liang, Y. Tong, Y. Li, *Nano Lett.* **2012**, *12*, 5376-5381.

38. P. Yang, D. Chao, C. Zhu, X. Xia, Y. Zhang, X. Wang, P. Sun, B. K. Tay, Z. X. Shen, W. Mai, H. J. Fan, *Adv. Sci.* **2016**, *3*, 1500299.

39. X. Xiao, X. Peng, H. Jin, T. Li, C. Zhang, B. Gao, B. Hu, K. Huo, J. Zhou, *Adv. Mater.* **2013**, *25*, 5091-5097.

40. L. Yuan, B. Yao, B. Hu, K. Huo, W. Chen, J. Zhou, *Energy Environ. Sci.* **2013**, *6*, 470-476.

41. J. Wang, J.-G. Wang, H. Liu, C. Wei, F. Kang, *J. Mater. Chem. A* **2019**, *7*, 13727-13735.

42. P. Yang, Y. Ding, Z. Lin, Z. Chen, Y. Li, P. Qiang, M. Ebrahimi, W. Mai, C. Wong, Z. Wang, *Nano Lett.* **2014**, *14*, 731-736.

43. Y. Song, T. Y. Liu, B. Yao, T. Y. Kou, D. Y. Feng, X. X. Liu, Y. Li, *Small* **2017**, *13*, 1700067-1700073.

44. Y. Song, T. Y. Liu, G. L. Xu, D. Y. Feng, B. Yao, T. Y. Kou, X. X. Liu, Y. Li, *J. Mater. Chem. A* **2016**, *4*, 7683-7688.

45. Y. Fang, B. Luo, Y. Jia, X. Li, B. Wang, Q. Song, F. Kang, L. Zhi, *Adv. Mater.* **2012**, *24*, 6348-6355.

46. M. Starsinic, R. L. Taylor, P. L. Walker, P. C. Painter, *Carbon* **1983**, *21*, 69-74.

47. J. Shen, A. Liu, Y. Tu, G. Foo, C. Yeo, M. B. Chan-Park, R. Jiang, Y. Chen, *Energy Environ. Sci.* **2011**, *4*, 4220-4229.

48. Y. Zhu, S. Murali, M. D. Stoller, K. J. Ganesh, W. Cai, P. J. Ferreira, A. Pirkle, R. M. Wallace, K. A. Cychosz, M. Thommes, D. Su, E. A. Stach, R. S. Ruoff, *Science* **2011**, *332*, 1537-1541.

49. W. Wang, W. Liu, Y. Zeng, Y. Han, M. Yu, X. Lu, Y. Tong, *Adv. Mater.* **2015**, *27*, 3572-3578.

50. G. Wang, H. Wang, X. Lu, Y. Ling, M. Yu, T. Zhai, Y. Tong, Y. Li, *Adv. Mater.* **2014**, *26*, 2676-2682.

51. C. Liu, C. Li, K. Ahmed, Z. Mutlu, I. Lee, F. Zaera, C. S. Ozkan, M. Ozkan, *Small* **2018**, *14*, 1702444.

52. S. W. Lee, N. Yabuuchi, B. M. Gallant, S. Chen, B.-S. Kim, P. T. Hammond, Y. Shao-Horn, *Nat. Nanotech.* **2010**, *5*, 531.

53. H. Zhang, W. Qiu, Y. Zhang, Y. Han, M. Yu, Z. Wang, X. Lu, Y. Tong, *J. Mater. Chem. A* **2016**, *4*, 18639-18645.

54. A. Sumboja, C. Y. Foo, X. Wang, P. S. Lee, *Adv. Mater.* **2013**, *25*, 2809-2815.

55. H. Xu, X. Hu, H. Yang, Y. Sun, C. Hu, Y. Huang, *Adv. Energy Mater.* **2015**, *5*, 1401882.

56. S. Chandrasekaran, B. Yao, T. Liu, W. Xiao, Y. Song, F. Qian, C. Zhu, E. B. Duoss, C. M. Spadaccini, Y. Li, M. A. Worsley, *Mater. Horiz.* **2018**, *5*, 1166-1175.

57. Y. Zheng, W. Zhao, D. Jia, L. Cui, J. Liu, *Chem. Eng. J.* **2019**, *364*, 70-78.

58. A. J. Bard, L. R. Faulkner, J. Leddy, C. G. Zoski, *Electrochemical methods: fundamentals and applications, Vol. 2,* Wiley New York, **1980**.

59. B. E. Conway, *Electrochemical supercapacitors: scientific, fundamentals and technological Applications*, Plenum, New York, **1999**.

60. Q. Wang, J. Yan, Z. J. Fan, *Energy Environ. Sci.* **2016**, *9*, 729-762.

61. T. Kim, G. Jung, S. Yoo, K. S. Suh, R. S. Ruoff, *ACS Nano* **2013**, *7*, 6899-6905.

62. H. R. Peng, B. Yao, X. J. Wei, T. Y. Liu, T. Y. Kou, P. Xiao, Y. H. Zhang, Y. Li, *Adv. Energy Mater.* **2019**, *9*, 1803665.

63. Y. Cheng, L. Huang, X. Xiao, B. Yao, L. Yuan, T. Li, Z. Hu, B. Wang, J. Wan, J. Zhou, *Nano Energy* **2015**, *15*, 66-74.

64. T. Liu, Z. Zhou, Y. Guo, D. Guo, G. Liu, *Nat. Commun.* **2019**, *10*, 675.

65. H. S. Kim, J. B. Cook, H. Lin, J. S. Ko, S. H. Tolbert, V. Ozolins, B. Dunn, *Nat. Mater.* **2017**, *16*, 454-460.

66. J. Wang, J. Polleux, J. Lim, B. Dunn, *J. Phys. Chem. C* **2007**, *111*, 14925-14931.

67. H. Lindström, S. Södergren, A. Solbrand, H. Rensmo, J. Hjelm, A. Hagfeldt, S.-E. Lindquist, *J. Phys. Chem. B* **1997**, *101*, 7717-7722.

68. V. Augustyn, J. Come, M. Lowe, J. Kim, P. Taberna, S. Tolbert, H. Abruna, P. Simon, B. Dunn, *Nat. Mater.* **2013**, *12*, 518-522.

69. Y. Song, P. Deng, Z. Qin, D. Feng, D. Guo, X. Sun, X.-X. Liu, *Nano Energy* **2019**, *65*, 104010.

70. D. Yang, Y. Song, Y.-J. Ye, M. Zhang, X. Sun, X.-X. Liu, *J. Mater. Chem. A* **2019**, *7*, 12086-12094.

71. Y. Lu, J. Liang, S. Deng, Q. He, S. Deng, Y. Hu, D. Wang, *Nano Energy* **2019**, *65*, 103993.

72. Y. Song, T. Y. Liu, M. Y. Li, B. Yao, T. Y. Kou, D. Y. Feng, F. X. Wang, Y. X. Tong, X. X. Liu, Y. Li, *Adv. Energy Mater.* **2018**, *8*, 1801784.

73. Z. Zhou, T. Liu, A. U. Khan, G. Liu, *Sci. Adv.* **2019**, *5*, eaau6852.

74. M. El-Kady, V. Strong, S. Dubin, R. Kaner, *Science* **2012**, *335*, 1326-1330.

75. P. Huang, C. Lethien, S. Pinaud, K. Brousse, R. Laloo, V. Turq, M. Respaud, A. Demortière, B. Daffos, P. L. Taberna, B. Chaudret, Y. Gogotsi, P. Simon, *Science* **2016**, *351*, 691-695.

76. B. Yao, L. Yuan, X. Xiao, J. Zhang, Y. Qi, J. Zhou, J. Zhou, B. Hu, W. Chen, *Nano Energy* **2013**, *2*, 1071-1078.

77. M. Ghidiu, M. Lukatskaya, M. Zhao, Y. Gogotsi, M. Barsoum, *Nature* **2014**, *516*, 78-81.

78. L. Yuan, X. H. Lu, X. Xiao, T. Zhai, J. Dai, F. Zhang, B. Hu, X. Wang, L. Gong, J. Chen, C. Hu, Y. Tong, J. Zhou, Z. L. Wang, *ACS Nano* **2012**, *6*, 656-661.

79. X. Lu, M. Yu, G. Wang, T. Zhai, S. Xie, Y. Ling, Y. Tong, Y. Li, *Adv. Mater.* **2012**, *25*, 267-272.

80. M. F. El-Kady, M. Ihns, M. Li, J. Y. Hwang, M. F. Mousavi, L. Chaney, A. T. Lech, R. B. Kaner, *Proc. Natl. Acad. Sci. U.S.A.* **2015**, *112*, 4233-4238.

81. T. S. Tran, K. M. Tripathi, B. N. Kim, I.-K. You, B. J. Park, Y. H. Han, T. Kim, *Mater. Res. Bull.* **2017**, *96*, 395-404.

82. X. Xiao, T. Ding, L. Yuan, Y. Shen, Q. Zhong, X. Zhang, Y. Cao, B. Hu, T. Zhai, L. Gong, J. Chen, Y. Tong, J. Zhou, Z. L. Wang, *Adv. Energy Mater.* **2012**, *2*, 1328-1332.

Chapter 8

Outlook

From 2D thin film electrodes to 3D printed electrodes, different materials have been discussed in this dissertation. 2D thin films represent the state-of-the-art form of electrodes in the practical supercapacitor fabrication. They are very promising for the future flexible energy storage systems that can integrate with other flexible electronics. Yet, to meet the increasing demand of energy density and fast charging capability, some challenges in these 2D film electrodes, such as low mass loading, deteriorated ion and electron transport in thick films, are becoming more troublesome. To address these problems and satisfy the high energy requirement for the future energy storage, 3D printing offers an alternative way to fabricate high-performance electrodes towards the advanced supercapacitors.

Since the 3D printing of functional electrodes are still at its early stage, there are still a lot of challenges in this area. The first and foremost issue is how to prepare suitable inks for the printing. An appropriate ink with the right rheology is the key for a successful 3D printing. A good printable ink should meet the following criteria. It should be sheer thinning.[1-2] With the increase of shear rates, its viscosity should decrease. It should also have quick switch of viscosity under different shear rates, which is resembled of the extrusion through narrow nozzles and the recovery of the ink's rheological property after printing. Viscoelastic fingerprints show the status of the ink under different shear stresses. A good ink should have predominantly solid-like behavior with a high storage modulus. When the stress is increased and reached to a critical point, the viscoelastic network in the inks breaks and flow like a liquid which enables its continuous extrusion through the micro-meter-sized nozzles.

Secondly, a well-structured electrode with optimized porosity should be designed. We already know that the ion transport in the 3D printed electrode is much easier than that in a bulk film electrode. However, the large voids in these 3D electrodes make them less competitive than the 2D thin films in volumetric capability of charge storage.[3-4] How to rationalize the distribution of pore size and electrode materials to achieve higher energy densities is still a challenge for the 3D printed electrodes. Simulation may provide a quick way to find out a suitable electrode structure with enough electrolyte infiltration and mobility and may shed some light for the experimental fabrication of the high-performance 3D electrodes.

Thirdly, chemical compositions in the 3D printed electrodes should be carefully tuned. Carbon materials are suitable choice for 3D printed materials due to their high surface area, good conductivity and easy tuned morphology.[5] The 3D printed carbon materials could uptake and deliver charges efficiently to satisfy the fast-charging requirement. Yet, the charges can be stored via their physical adsorption/desorption processes are limited. To further increase the charge density in the 3D printed electrodes, incorporation of carbon materials with pseudocapacitive materials such as metal oxides, conducting polymers, metal sulfides, and metal nitrides will be a promising research direction.

Finally, it is important to notice that the metrics of areal capacitance, volumetric capacitance and gravimetric capacitance are all important for a future supercapacitor electrode. For most of the conventional bulk electrodes, high capacitance normalized to area, gravimetry and volume are impossible.[6] For example, extraordinary gravimetric capacitances can be obtained at tiny amount of active material loadings. However, their areal capacitance would be significantly advantageous compared to other high mass-loading electrodes. 3D printed electrodes have shown their promise in breaking this long-term trade-off. They have displayed outstanding areal capacitance because of their high mass loadings and decent gravimetric and volumetric capacitance. How to further improve their gravimetric and volumetric performance under these high loadings will be the research focus of our next steps.

References

1. W. Yang, J. Yang, J. J. Byun, F. P. Moissinac, J. Xu, S. J. Haigh, M. Domingos, M. A. Bissett, R. A. W. Dryfe, S. Barg, *Adv. Mater.* **2019**, *31*, e1902725.
2. C. Zhu, T. Y. Han, E. B. Duoss, A. M. Golobic, J. D. Kuntz, C. M. Spadaccini, M. A. Worsley, *Nat. Commun.* **2015**, *6*, 6962.
3. B. Yao, S. Chandrasekaran, H. Zhang, A. Ma, J. Kang, L. Zhang, X. Lu, F. Qian, C. Zhu, E. B. Duoss, C. M. Spadaccini, M. A. Worsley, Y. Li, *Adv. Mater.* **2020**, *32*, 1906652.
4. X. Tang, H. Zhou, Z. Cai, D. Cheng, P. He, P. Xie, D. Zhang, T. Fan, *ACS Nano* **2018**, *12*, 3502-3511.

5. T. Y. Liu, F. Zhang, Y. Song, Y. Li, *J. Mater. Chem. A* **2017**, *5*, 17705-17733.

6. B. Yao, S. Chandrasekaran, J. Zhang, W. Xiao, F. Qian, C. Zhu, E. B. Duoss, C. M. Spadaccini, M. A. Worsley, Y. Li, *Joule* **2019**, *3*, 459-470.